**Astronomy
&
Astrophysics**

ATOMIUM: ALMA tracing the origins of molecules in dust forming oxygen rich M-type stars

Motivation, sample, calibration, and initial results

C. A. Gottlieb[1], L. Decin[2,3], A. M. S. Richards[4], F. De Ceuster[2,5], W. Homan[2], S. H. J. Wallström[2],
T. Danilovich[2], T. J. Millar[6], M. Montargès[2,7], K. T. Wong[8], I. McDonald[4,9], A. Baudry[10], J. Bolte[2],
E. Cannon[2], E. De Beck[11], A. de Koter[2,12], S. Etoka[4], D. Gobrecht[2], M. Gray[4,14],
F. Herpin[10], M. Jeste[15], P. Kervella[16], T. Khouri[11], E. Lagadec[17], S. Maes[2], J. Malfait[2], K. M. Menten[15],
H. S. P. Müller[18], B. Pimpanuwat[4,14], J. M. C. Plane[3], R. Sahai[19], M. Van de Sande[20,2], L. B. F. M. Waters[21,22],
J. Yates[5], and A. Zijlstra[4,23]

(Affiliations can be found after the references)

ABSTRACT

This overview paper presents ATOMIUM, a Large Programme in Cycle 6 with the Atacama Large Millimeter/submillimeter Array (ALMA). The goal of ATOMIUM is to understand the dynamics and the gas phase and dust formation chemistry in the winds of evolved asymptotic giant branch (AGB) and red supergiant (RSG) stars. A more general aim is to identify chemical processes applicable to other astrophysical environments. Seventeen oxygen-rich AGB and RSG stars spanning a range in (circum)stellar parameters and evolutionary phases were observed in a homogeneous observing strategy allowing for an unambiguous comparison. Data were obtained between 213.83 and 269.71 GHz at high ($\sim0\farcs025$–$0\farcs050$), medium ($\sim0\farcs13$–$0\farcs24$), and low ($\sim1''$) angular resolution. The sensitivity per ~1.3 km s^{-1} channel was 1.5–5 mJy beam^{-1}, and the line-free channels were used to image the millimetre wave continuum. Our primary molecules for studying the gas dynamics and dust formation are CO, SiO, AlO, AlOH, TiO, TiO$_2$, and HCN; secondary molecules include SO, SO$_2$, SiS, CS, H$_2$O, and NaCl. The scientific motivation, survey design, sample properties, data reduction, and an overview of the data products are described. In addition, we highlight one scientific result – the wind kinematics of the ATOMIUM sources. Our analysis suggests that the ATOMIUM sources often have a slow wind acceleration, and a fraction of the gas reaches a velocity which can be up to a factor of two times larger than previously reported terminal velocities assuming isotropic expansion. Moreover, the wind kinematic profiles establish that the radial velocity described by the momentum equation for a spherical wind structure cannot capture the complexity of the velocity field. In fifteen sources, some molecular transitions other than ^{12}CO $v = 0$ $J = 2 - 1$ reach a higher outflow velocity, with a spatial emission zone that is often greater than 30 stellar radii, but much less than the extent of CO. We propose that a binary interaction with a (sub)stellar companion may (partly) explain the non-monotonic behaviour of the projected velocity field. The ATOMIUM data hence provide a crucial benchmark for the wind dynamics of evolved stars in single and binary star models.

Key words. stars: AGB and post-AGB – stars: mass-loss – circumstellar matter – binaries: general – instrumentation: interferometers – astrochemistry

1. Introduction

A long-standing question in astrophysics is the physicochemical mechanism describing the complex phase transition from small molecules – containing typically only two or three atoms – to larger gas phase clusters, and eventually tiny dust grains, with the first thermochemical computations probably presented in the first half of the 1930s (Wildt 1933; Russell 1934). We are still struggling to predict how the composition of the gas with specific initial conditions for the thermodynamical and other physical properties (such as temperature, density, and velocity) will evolve in time. Aiming to unravel this question, astronomers have focussed their attention on low- and intermediate-mass asymptotic giant branch (AGB) stars and their more massive counterparts, the red supergiants (RSGs). The winds of AGB and RSG stars have long been recognised as key chemical laboratories in which more than 90 molecules and 15 dust species have been detected thus far (Habing 1996; Habing & Olofsson 2004; Heras & Hony 2005; Verhoelst et al. 2009; Waters 2011; Gail & Sedlmayr 2013; Höfner & Olofsson 2018). Convection-induced dredge-ups in the atmosphere, shocks, nucleation, and

stellar and interstellar UV photons in the circumstellar envelope are just a few of the physicochemical processes that determine the chemical fingerprints of AGB and RSG stellar winds (see Sect. 2.1.2). A large variety of chemical reactions occur in the wind, including unimolecular, two- and three-body reactions, cluster growth, and grain formation. Through their winds, AGB and RSG stars contribute $\sim85\%$ of the gas and $\sim35\%$ of the dust from stellar sources to the Galactic ISM (Tielens 2005), and are the dominant source of pristine building blocks of interstellar material.

Hoyle & Wickramasinghe (1962) were the first to propose that the wind acceleration in AGB stars is caused by radiation pressure on newly formed dust grains. Molecules might carry the analogous potential to launch a RSG wind, with grains taking over farther out in the wind (Gustafsson et al. 1992). It is generally accepted that pulsations are a key ingredient of AGB mass-loss with pulsation-induced shock waves levitating the gas to larger distances where the temperature is low enough for dust to condense (Hinkle et al. 1982, 1997; Bowen 1988; McDonald & Zijlstra 2016; Höfner & Olofsson 2018, and references therein). Convection-induced pulsation amplitudes are,

however, much lower for RSG stars and the role of pulsations in triggering the RSG wind is thought to be negligible. The prevailing streamlines in the AGB and RSG winds outside $\sim 5R_\star$ are radial (Höfner & Olofsson 2018, and references therein), although recent observations with ALMA have added structural complexities to this picture (see Sect. 2.1.1). Even so, the dynamical behaviour in the winds is much simpler than in other chemically rich environments, such as high-mass star-forming regions, young stellar objects and protoplanetary disks. If we can disentangle the (thermo)dynamical and chemical processes in the winds, we might be able to lay the foundation for a better understanding of the gas-to-dust phase transition as well as some of the physiochemical processes that occur in (pre-biotic) chemistry in these more complex environments.

The ALMA ATOMIUM[1] Large Programme has been constructed with the specific aim of understanding the chemistry of dust precursors and dust formation, as well as the more general aim of identifying chemical processes applicable to other astrophysical environments (including novae, supernovae, protoplanetary nebulae, and interstellar shocks). The obvious choice of targets for the ATOMIUM project are oxygen-rich AGB and RSG stellar winds (O-rich, C/O < 1; see Sect. 2.2), because ALMA provides the unique ability to study the many oxide and hydroxide precursors of dust in O-rich winds – something we cannot do for carbonaceous grains in carbon-rich (C/O > 1) winds, where the likely precursors such as aromatic molecules and polycyclic aromatic hydrocarbons (PAHs) are not observable with ALMA.

In this paper we discuss the scientific motivations for ATOMIUM, introduce the survey strategy as well as the source and spectral line sample (Sect. 2), and describe the calibration process (Sect. 3). All the data are available in the ALMA Science Archive, but in addition enhanced data products have been prepared. These are described in Sect. 4, and they will serve as a legacy for the astronomical community and will seed new insights in the dynamical and chemical process in evolved stars and other astronomical media. The quality and the properties of the data products are illustrated in the example of the OH/IR star IRC−10529 in Sect. 4.2 and the accompanying figures. In Sect. 5 we focus on one scientific result – the wind kinematics in the circumstellar envelopes of evolved stars. We discuss the efficiency of the wind initiation and show how the presence of a binary companion can be revealed via a study of the wind velocity profile, thereby demonstrating how the ATOMIUM data provides a crucial benchmark for single and binary star models of the wind dynamics of evolved stars.

Other results will be presented in separate papers including: detailed discussions of the individual sources; a chemical inventory of the molecular species in all 17 stars, observed in the three array configurations with an angular resolution that spans 50 mas−10″; and studies of the dust precursors, masers, and the wind morphology (Decin et al. 2020; Homan et al. 2020, 2021). In addition, various hydrodynamical, chemical, and radiative transfer models that simulate the wind properties of AGB and RSG stars and support the analysis of the ATOMIUM data, have already been published or are underway (see, for example, Decin 2021; De Ceuster et al. 2020a).

2. The ALMA ATOMIUM Large Programme

2.1. Scientific goals

The goal of the ALMA ATOMIUM Programme is: (1) to derive the morpho-kinematical and chemical properties of the winds; (2) to unravel the phase change from gaseous to solid-state species; (3) to identify the dominant chemical pathways; (4) to study the role of (un)correlated density structures[2] on the overall wind structure; and (5) to examine the reciprocal effect between various dynamical and chemical phenomena in 17 oxygen-rich AGB and RSG sources which cover a range of initial stellar masses, pulsations, mass-loss rates, and evolutionary phases (see Sect. 2.2).

Summarised in the following paragraphs are key science questions that are addressed in this large programme. For sake of clarity, we differentiate between physical and chemical phenomena, although both are coupled in an intimate way, as for example via the dust extinction efficiency Q_λ described in Sect. 5.

2.1.1. Dynamical behaviour of stellar winds

Wind initiation in the inner wind region ($1\,R_\star \lesssim r \lesssim 10 - 30\,R_\star$). The winds in O-rich AGB stars can only be predicted theoretically on the premise of pulsation-induced higher density regions close to the star where large transparent grains can form (Hinkle et al. 1982, 1997; Bertschinger & Chevalier 1985; Bowen 1988; Woitke 2006; Höfner 2008; Bladh et al. 2019). For RSGs the role of grains close to the star remains unresolved (Josselin & Plez 2007; Bennett 2010; Scicluna et al. 2015; Kervella et al. 2018; Montargès et al. 2019).

Fonfría et al. (2008) have used mid-infrared bands of molecules to study the dust formation zone. High-resolution ALMA data carry the same diagnostics, and trace the region closer to the star if high-excitation lines are studied. Recent observational studies have shown that the wind acceleration for O-rich AGB stars is often less efficient than previous predictions obtained by solving the momentum equation (Decin et al. 2010a, 2018; Khouri et al. 2014; Van de Sande et al. 2018a, see Eq. (2) in Sect. 5). This behaviour couples directly to the unknown grain composition (see also Sect. 2.1.2). Moreover, it is not yet known if the wind acceleration profile is different for regular versus irregular pulsators.

As a first step in determining where the wind is initiated, the wind kinematics of 17 oxygen-rich AGB and RSG stars in the ATOMIUM sample have been derived (see Sect. 5), which in turn allows us to correlate the wind acceleration profile to the specific stellar (and hence pulsation) characteristics and chemical properties; and will contribute to recent studies that investigate the role of pulsations as triggers for the onset of the mass loss and in controlling the rate of the mass loss (McDonald & Zijlstra 2016; McDonald & Trabucchi 2019).

Enforced dynamics in the intermediate wind region ($r \sim 30 - 400\,R_\star$). Accurate measurements of the wind velocities are a major factor in determining the AGB (RSG) mass-loss rate, and thus the lifetime and impact on Galactic enrichment. Recent ALMA data revealed a thought-provoking picture of the wind kinematics in the intermediate wind region (Decin et al. 2018): (i) the wind acceleration appears to continue beyond $\sim 30\,R_\star$,

---

[2] The term 'correlated density structures' refer to arcs, spirals, disks, bipolar structures, shells, etc. 'Uncorrelated density structures' refer to clump-like morphologies which do not appear to be correlated with any other morphology.

in contradiction to the solution of the momentum equation (see also Sect. 5); and (ii) the line profiles indicate that the maximum wind velocity – as derived from the primary tracer CO and other molecules – is much higher than the previously determined terminal wind velocity, with differences of up to a factor >4 in the case of R Dor (Decin et al. 2018). This surprising behaviour is seen for all AGB and RSG stars for which the ALMA line sensitivity is greater than a few mJy/beam. The reason for these enforced wind dynamics is still unclear, since further grain growth seems implausible owing to the low densities in regions far from the star (but see Sect. 5.4). Because the wings of the (low-excitation) lines carry the diagnostic information needed to unravel this science question, a sample of evolved stars was observed at very high sensitivity in ATOMIUM (complemented with other data, part of which has already been obtained with ALMA). Prior to this, only a handful of evolved stars underwent such observations with ALMA.

Wind morphology. The first step for identifying the wind-shaping mechanism(s) and retrieving the wind kinematics in AGB and RSG stars, was to map the 3D wind morphology. The ^{12}CO $v = 0$ $J = 1 - 0$ and $J = 2 - 1$ channel maps observed with single antennas at an angular resolution of $21''$ and $13''$, respectively, indicated that about 80% of the AGB and RSG winds show a large scale spherical symmetry. Observations of 24 oxygen rich AGB stars with a synthesised beam of about $4''$ (Neri et al. 1998), found that most have an outer circumstellar envelope that is mainly circular and an inner envelope whose shape was not easily discerned at the limited resolution. However, departures in the spherical symmetry of the CO $J = 1 - 0$ and $J = 2 - 1$ emission in the circumstellar envelopes of some oxygen rich AGB stars were identified when they were observed at a modest resolution of $1''$ or lower by Castro-Carrizo et al. (2010).

Data acquired subsequently with ALMA at higher angular resolution revealed that a significant fraction of the winds exhibit structural complexities embedded in the smooth radially outflowing wind which include arcs, shells, bipolar structures, clumps, spirals, tori, and rotating discs (Maercker et al. 2012; Ramstedt et al. 2014, 2017, 2018; Kim et al. 2015; Decin et al. 2015, 2019, 2020; Cernicharo et al. 2015; Wong et al. 2016; Kervella et al. 2016; Agúndez et al. 2017; Doan et al. 2017, 2020; Homan et al. 2018; Bujarrabal et al. 2018; Guélin et al. 2018; Randall et al. 2020; Hoai et al. 2020). For most of these morphologies, the formation mechanism is unknown, although binarity is suspected to play an important role. In two particular cases, the ALMA data suggest there is a planetary companion at a disc's inner rim (Kervella et al. 2016; Homan et al. 2018). In addition, hydrodynamical instabilities occurring in a multi-fluid environment and convection-induced activity can lead to the formation of overdense clumps (see for example, Montargès et al. 2019).

To analyse the correlated density structures, high spatial resolution data which sample a range in molecular excitation regime (and hence sample the extended wind region) was acquired. The key molecule is CO owing to: its high fractional abundance (with respect to H$_2$); its high dissociation energy; its simple energy level structure; and its rotational levels are readily excited by collisions. Other complementary tracers include the rotational transitions of SiO, HCN, and NaCl (see, e.g., Kervella et al. 2016; Decin et al. 2016). The first observations acquired in the ATOMIUM project were with an angular resolution of $0\rlap{.}''13$–$0\rlap{.}''24$ in the mid array configuration (see Sect. 3). The analysis of the ^{12}CO $v = 0$ $J = 2 - 1$ and ^{28}SiO $v = 0$

$J = 5 - 4$ and $J = 6 - 5$ rotational lines[3] has provided a unique view of the prevailing wind morphology in the ATOMIUM sources (Decin et al. 2020). This is illustrated by the channel maps of ^{12}CO (Fig. 3), SO$_2$ (Fig. 4), and SiO (Fig. 5) in the OH/IR star IRC -10529 (see also Sect. 4.2). None of the ATOMIUM sources display a spherical wind geometry. The derived morphologies: (1) correlate with the mass-loss rate; (2) yield important insights into the mechanism(s) determining the appearance of AGB descendants, post-AGB stars, and planetary nebulae in which cylindrically symmetric and multi-polar morphologies are often observed (Guerrero et al. 2003; Ercolano et al. 2003; Ueta et al. 2007); and (3) can be explained by binary interaction (Decin et al. 2020).

2.1.2. Chemical processes in stellar winds

Significant advances have been made in the past few years in characterising the physical and chemical properties of the dust in the inner wind owing to: (1) the polarimetric direct imaging of the dust in the visible at high angular resolution with VLT/SPHERE by Khouri et al. (2016a, 2018, 2020), Ohnaka et al. (2016, 2017), and Adam & Ohnaka (2019); and (2) parallel observations of the rotational spectra of potential Ti and Al bearing precursors of the dust (Kamiński et al. 2016, 2017; Decin et al. 2017; Takigawa et al. 2017; Danilovich et al. 2020a). However, very little is known about the physicochemical processes in the intermediate wind where dust-gas interactions occur, and tiny dust grains formed in the inner wind, grow in size by accretion of small abundant gaseous molecules onto the grains (for a comprehensive overview see the review by Decin 2021, and references therein). As noted in the discussion of the enforced dynamics in Sect. 2.1.1, it was unclear why the wind velocity has not yet reached its terminal velocity in the intermediate wind region. One of the main emphases of ATOMIUM is to better understand the chemistry in the intermediate wind.

To date most chemical models of oxygen-rich AGB stars have been devoted to the study of either the initial stage of dust formation in the inner wind at $\lesssim 10-30\,R_\star$ (Cherchneff 2006; Gobrecht et al. 2016; Boulangier et al. 2019), or to the photon dominated chemistry in the outer wind (Willacy & Millar 1997; Li et al. 2016). Of the 11 parent molecules considered by Van de Sande et al. (2019) in their chemical kinetics model of the intermediate wind region, all but two were observed in ATOMIUM (N$_2$ and NH$_3$), allowing us: (1) to derive the extent of the emission and potential depletion in the outflowing wind of nine of the 11 molecules in 17 sources from observations in the three array configurations; and (2) to compare the measured depletions with the predictions of the chemical kinetic models that include dust-gas interactions in the AGB outflow.

Continuum radiation. At millimeter wavelengths, the bulk of the continuum emission comes from the extended stellar atmosphere (Reid & Menten 1997). For most of the stars, the ATOMIUM observations at the highest resolution allow us to either resolve or to fit a disc to the 1.2 mm stellar continuum which is known to be 15–50% greater than the optical size listed in Table 1 (Vlemmings et al. 2019). On the assumption the star emits as a blackbody, the stellar flux at millimeter wavelengths can be estimated from the stellar effective temperature and luminosity. The derived stellar flux has been found to agree with fitting a uniform disc to the millimeter-wave visibilities when the

---

[3] Hereafter, all rotational transitions are in the ground ($v = 0$) vibrational state unless otherwise specified.

Table 1. Summary of some (circum)stellar parameters of the ATOMIUM sample.

Star [a]	Variability type [e]	Mass-loss rate ($M_\odot$/yr)	Pulsation period P (days)	Distance D (pc)	Stellar diameter [b] θ_d (mas)	T_{eff} [b] (K)	L [c] ($L_\odot$)	$v_{\text{LSR}}^{\text{new}}$ [d] (km s^{-1})
S Pav	SRa	8×10^{-8} [aa]	381 [aa]	190 [jj]	12.	3100 [xx]	4900	−18.2
T Mic	SRb	8×10^{-8} [aa]	347 [aa]	210 [jj,ll]	9.3	3300 [xx]	4700	25.5
U Del	SRb	1.5×10^{-7} [aa]	119 [jj]	330 [jj,ll,yy]	7.9 [uu]	2800	4100	−6.8
RW Sco [f]	Mira	2.1×10^{-7} [bb]	389 [bb]	514 [jj]	4.9	3300 [xx]	7700	−69.7
V PsA	SRb	3×10^{-7} [aa]	148 [aa]	278 [jj]	13.	2400 [aa]	4100	−11.1
SV Aqr	LPV	3×10^{-7} [aa]	$\cdots$	389 [jj]	4.4	3400 [xx]	4000	6.7
R Hya [g]	Mira	4×10^{-7} [cc]	366 [ll]	165 [pp]	23. [uu]	2100 [cc]	7400	−10.1
U Her	Mira	5.9×10^{-7} [dd]	402 [ll]	266 [qq]	11. [uu]	3100	8000	−14.9
π^1 Gru [g],[h]	SRb	7.7×10^{-7} [ee]	150 [cc]	197 [jj,ll]	21. [vv]	2300 [cc]	4700	−11.7
AH Sco	SRc	1×10^{-6} [ff]	738 [mm]	2260 [rr]	5.8 [ss]	3700	330000	−2.3
R Aql [f]	Mira	1.1×10^{-6} [dd]	268 [ll]	230 [jj,ll]	12. [uu]	2800 [cc]	4900	47.2
W Aql [g],[h]	Mira.	3×10^{-6} [gg]	479 [ll]	375 [jj]	11. [uu]	2800	9700	−23.0
GY Aql	Mira	4.1×10^{-6} [hh]	468 [ll]	152 [jj]	21.	3100 [xx]	9600	34.0
KW Sgr	SRc	5.6×10^{-6} [ii]	647 [nn]	2400 [ss]	3.9 [ss]	3700	175700	−4.4
IRC−10529 [f]	Mira	4.5×10^{-6} [cc]	680 [cc]	760 [cc]	6.5	2700 [cc]	14400	−16.3
IRC+10011 [f]	Mira	1.9×10^{-5} [cc]	660 [cc]	740 [cc]	6.5	2700 [cc]	13900	10.1
VX Sgr	SRc	6.1×10^{-5} [jj]	732 [oo]	1560 [tt]	8.8 [ww]	3500	102300	5.7

Notes. [a]Stars are ordered by increasing mass-loss rate. [b]For all the stars, either the stellar diameter (θ_d) or T_{eff} (or both) are derived from direct measurement; there are no objects for which indirect calculations are used for both parameters. The references in the footnotes refer to the direct measurements. The other parameter is then derived from the relation $L(R_\star, T_{\text{eff}})$ with $R_\star$ determined from the stellar diameter and the distance. [c]Derived from the $M_{\text{bol}}(P, L)$ relation in De Beck et al. (2010) unless indicated otherwise. [d]Estimate of the local standard of rest velocity derived from a sample of rotational lines with well behaved line profile shapes and laboratory measured frequencies observed in the ALMA ATOMIUM survey. [e]Mira variables have regular, large amplitude variations in the visible with $\delta V > 2.5$ mag and are thought to be fundamental mode pulsators; semiregular variables (SR) are of smaller amplitude, $\delta V < 2.5$ mag, with pulsations in the fundamental, first, and even higher overtone modes (Wood 2015). Semiregular variables that have stable periodicity are classified as SRa, while variables with different duration of individual cycles are classified as SRb. SRc semiregulars are variable supergiants. A source is classified as a long-period variable (LPV) if no regular pulsation period P could be deduced from the observations, in which case P is indicated by '$\cdots$' in Col. 4. [f]OH/IR star – Mira variables that show strong OH maser emission in the hyperfine split ground state transitions at 18 cm. [g]Known binary system. [h]S-type AGB star with a carbon to oxygen ratio (C/O) slightly less than 1.
References. [aa]Olofsson et al. (2002); [bb]Groenewegen et al. (1999); [cc]De Beck et al. (2010); [dd]Young (1995); [ee]Doan et al. (2017); [ff]Josselin et al. (1998); [gg]Ramstedt et al. (2017); [hh]Loup et al. (1993); [ii]Vogt et al. (2016); [jj]Gaia Collaboration (2018); [kk]Andronov & Chinarova (2012); [ll]Perryman et al. (1997); [mm]Kiss et al. (2006); [nn]Wittkowski et al. (2017); [oo]Samus et al. (2017); [pp]Zijlstra et al. (2002); [qq]Vlemmings & van Langevelde (2007); [rr]Shen & Zhou (2008); [ss]Arroyo-Torres et al. (2013); [tt]Chen et al. (2007); [uu]Richichi et al. (2005); [vv]Paladini et al. (2018); [ww]Chiavassa et al. (2010); [xx]Marigo et al. (2008).; [yy]Bailer-Jones et al. (2021).

S/N is sufficiently high (Homan et al. 2021). For at least some of the sample, an excess of the more extended emission that is typically up to a few tens of a percent of the stellar emission is detected with ALMA (Decin et al. 2018; Dehaes et al. 2007), which will allow us to subtract the stellar contribution and to measure the dust emission. Supplemented by data of the spectral energy distribution (SED) at other wavelengths, the dust mass and the (recent) dust mass-loss rate can be derived (Decin et al. 2018, Khouri et al., in prep.). Combined with the gas mass-loss rate derived from lines of CO acquired previously with single antennas, the gas-to-dust ratio as a function of stellar type can be determined Danilovich et al. (2015a). In addition, the determination of the positions of SiO masers close to the stellar surface with even finer precision in ATOMIUM, allow us to investigate the possible connection between dust clumps, particular molecular emission patterns, and stellar characteristics (Homan et al. 2020).

Dust nucleation. A major unknown in current wind models concerns the initial dust nucleation process (Gail & Sedlmayr 2013). When the ATOMIUM project was undertaken, it was not known which molecules form the large gas phase clus-

ters that transition into the first solid-state species in oxygen rich winds (Paquette et al. 2011; Plane 2013; Bromley et al. 2016). Thermodynamic condensation sequences favour alumina (Al_2O_3) or Fe-free silicates (such as Mg_2SiO_4), where the Al_2O_3 is formed at slightly higher temperatures (Tielens et al. 1998; Bladh & Höfner 2012). Grains of this type, however, need to be large enough (~ 200 nm–1 μm) and close to the star ($r \lesssim 10 R_\star$) for photon scattering to compensate for their low near-infrared absorption cross sections, and to trigger the onset of a stellar wind (Höfner 2008).

Recent NACO and SPHERE data support the presence of large transparent grains (~ 0.3 μm) at $\sim 1.5 R_\star$ in some AGB and RSG stars (Norris et al. 2012; Khouri et al. 2016a; Haubois et al. 2019), but this data cannot pinpoint the chemical build-up of the grains. As shown in recent publications (Kamiński et al. 2017; Decin et al. 2017; Takigawa et al. 2017), ALMA has paved the way for unraveling the composition of the tiny dust seeds via the study of specific small gaseous precursors. The synergy between ALMA and (near-)infrared data is allowing us in turn to establish which gas phase clusters [such as $(Al_2O_3)_n$ with $n > 1$] might be the intermediate steps in this dust nucleation history (Decin et al. 2017).

The metal oxides and hydroxides AlO, AlOH, TiO, OH – and most prominently SiO – are the key molecules we are using to study the impact of higher density clumps and correlated density structures on the time scales for dust growth in the inner region, and the efficiency of ice deposition in the intermediate region of the 17 stars in the ATOMIUM survey. The abundance structures are being examined with the recent radiative transfer analysis of vibrationally excited AlO and TiO in R Dor which has provided a new view of the formation of Al_2O_3 dust (Danilovich et al. 2020a) – and the same approach is also being applied to CO, HCN, SO, SO_2, SiS, AlCl, NaCl, and PO which are observed in non-maser emission in the ground and the excited vibrational levels within a couple of $R_\star$ of a number of the stars in the ATOMIUM sample.

Non-equilibrium gas-phase chemistry. For a long time, the gas-phase composition of stellar winds was believed to be determined solely by the C/O ratio of the stellar photosphere, hence no carbon-bearing molecules except for CO were expected to form in oxygen rich winds. The detection of CO_2, CS, and HCN in oxygen rich winds, and H_2O, OH, H_2CO, and SiO in carbon rich winds has caused this picture to be amended (Deguchi & Goldsmith 1985; Lindqvist et al. 1988; Bujarrabal et al. 1994; Justtanont et al. 1998; Ryde et al. 1998; Melnick et al. 2001; Ford et al. 2003, 2004; Schöier et al. 2006, 2013; Decin et al. 2008; Velilla Prieto et al. 2015). Pulsation-induced shock chemistry, and/or enhanced photochemical activity in a non-homogeneous outflow in which the harsh interstellar UV photon can deeply penetrate, have been proposed as potential explanations (Agúndez et al. 2010, 2017, 2020; Cherchneff 2011; Gobrecht et al. 2016; Van de Sande et al. 2018b). Such chemical modelling codes are based on a range of parameters including: velocity shock strength, specific clumpiness, and rates in the chemical network.

The observation of 24 different molecules and the measurement of approximately 290 rotational lines in ATOMIUM (supplemented with ALMA archival data) is described in a comprehensive Molecular Inventory paper (Wallström et al., in prep.), which includes the complete tabulation of the measured parameters (peak flux, width, and integrated area) of each rotational line observed in the 17 stars in the three array configurations. This homogenous set of measurements provides the fundamental benchmarks for establishing the essential parameters for the development of predictive chemical kinetic codes which includes: the angular size of the emission region in each molecule; the column densities and abundance distributions with radial extent; and the comparison of the spatial distributions of the different molecules in each star. Also being examined in the Molecular Inventory paper is evidence for trends in the distributions of the molecules according to pulsation type, pulsation period, pulsation phase, C/O ratio, mass-loss rate, and morphology.

The ATOMIUM observations also serve as a guide for new laboratory kinetic measurements, and quantum chemical calculations of accurate theoretical structures and kinetic reaction rates needed to assess the relevant gas phase reaction rates in prior and newly developed chemical kinetic codes (e.g., Gobrecht et al. 2018; West et al. 2019; McCarthy et al. 2019; Boulangier et al. 2019; Escatllar & Bromley 2020). The first paper resulting from these observations entails a detailed analysis of the rotational spectra of the aluminium halides in W Aql, augmented with supplementary observations from *Herschel* (Danilovich et al. 2021). We found that the abundance profiles calculated with an existing chemical kinetic model (Van de Sande et al. 2018b) better reproduces the observations when six new reactions of Al, AlO, and AlOH with HF and HCl were added to the gas phase rates provided in the UMIST database by McElroy et al. (2013), where the newly incorporated reaction rates in Danilovich et al. were obtained from detailed theoretical quantum chemical calculations in support of this project. The revised chemical kinetic code derived by Danilovich et al. should yield more accurate predictions of the abundances of these species in other S-type stars.

New identifications. About 60 unidentified (U) lines have been observed in the ATOMIUM survey. Potential carriers of interest include the gaseous oxides, hydroxides, and sulfides of Ca, Fe, Mg, and Zr; HSiO and H_2SiO; and more complex oxides of Al (e.g., AlOAlO, AlO_3, and Al_2O_3), and of Si (e.g., SiO_3, Si_2O, and Si_3O). Relating strengths of rotational lines of unidentified species observed at high sensitivity with ALMA across frequency bands and (circum)stellar properties is a crucial step in assigning the molecular carrier, and will empower us to build a detailed molecular census which will serve as a legacy for the entire astronomical community.

2.2. ATOMIUM sample

The ATOMIUM sample consists of 17 O-rich sources which span a range in (circum)stellar properties of evolved AGB and RSG stars. Our sample was selected so that the stars are observable with ALMA, but had not been previously observed at high angular resolution at millimeter wavelengths. The sources have been selected to cover some of the most important parameters for determing the wind characteristics of evolved giant stars such as: mass-loss rate, pulsation behaviour, and red supergiant versus AGB stars. As commented on above, ensemble studies are not yet possible with ALMA in its high resolution mode. Therefore a well-selected, yet small sample is the best way forward for enhancing our knowledge of these systems. The sample covers a range in mass-loss rates of $\sim 10^{-7}$ to $\sim 10^{-5}$ $M_\odot$ yr^{-1}, as inferred from s ingle antenna observations, and consists of stars that are as close to Earth as possible. The selection criteria did not take into account prior evidence for possible binary companions.

Table 1 gives an overview of some of the important (circum)stellar parameters. More details on how these parameters have been selected and the references to relevant papers, can be found in Sect. S1 in the Supplementary Materials in Decin et al. (2020). The only changes with respect to the values of the 14 stars cited in Decin et al. (2020) are the newly adopted: (i) mass-loss rate of IRC −10529 from the more recent results of Danilovich et al. (2015a); and (ii) the distance towards U Her from the improved maser parallax determination of 266 pc (Vlemmings & van Langevelde 2007), which also impacts the estimate of the effective temperature. Also included in the ATOMIUM survey are the three red supergiants AH Sco, KW Sgr, and VX Sgr[4].

---

[4] While this paper was in the final stage of preparation, the *Gaia* Early Data Release 3 (*Gaia* EDR3) became available. In 12 out of 15 ATOMIUM stars the distances in *Gaia* EDR3 are within ∼20% of the distances we have used here (see Table 1); two objects have no *Gaia* measurements (IRC−10529 and IRC+10011); and two of the remaining three stars have maser parallax distances that should be more accurate. We have adopted the distance for W Aql from *Gaia* EDR3 which is consistent with that in Danilovich et al. (2021); and the maser parallax distance for AH Sco of 2260 pc (Chen & Shen 2008), which is closer (by 21%) than the *Gaia* DR2 distance. Although the maser parallax distance for VX Sgr that we have adopted is at odds with *Gaia* EDR3, it is consistent with all previous measurements including *Gaia* DR2 (Richichi et al. 2005; Paladini et al. 2018).

3. Observations

3.1. ATOMIUM observing strategy

A primary requirement for the ATOMIUM project was homogeneous observations across the sample that would allow unambiguous comparison among sources. The most efficient way for ALMA to achieve the science goals described in Sect. 2.1 was to target specific spectral frequency regions, and to observe all 17 ATOMIUM sources in the same spectral regions. We know exactly which molecules to monitor in Band 6 to determine the dynamical behaviour of the winds (Sect. 2.1.1), and to answer the questions of gas-phase chemistry and dust nucleation (Sect. 2.1.2). The spectral range was chosen so we automatically had the same appropriate molecules to trace the gas phase chemistry in all 17 stars in the ATOMIUM survey, while serendipitous detections came for free.

To spatially resolve the dust condensation region ($r \lesssim 10$–$30\,R_\star$), an angular resolution (AR) of $\sim$25–50 mas was needed for our targets, which all have large stellar angular diameters of between 3.9 and 20.5 mas (see Table 1). The finest AR requested was 25 mas for each target, while we allowed for an upper limit of 35 mas for stars with stellar angular diameter <9 mas and of 50 mas for the larger stars. This was offered in C43-8/C43-9 with maximum recoverable scale (MRS) $\sim$0$\farcs$38–0$\farcs$62 (henceforth referred to as either 'extended' or 'high resolution'). To attain the full line strength of the transitions, we needed to complement these observations with data from a more compact configuration, C43-5/C43-6, at an AR of 0$\farcs$24/0$\farcs$13 with maximum MRS of 1$\farcs$5 (henceforth 'mid' or 'medium resolution'). Extended emission of the CO and SiO transitions in the ground-vibrational state might still be resolved out even with the mid configuration. Hence, observations with an even more compact configuration were needed to recover the total fluxes of these transitions. For all targets, various single antenna CO line measurements are available to derive the global thermal structure of the wind. Hence, the request for the low-resolution observations was primarily based on the estimated extents of the SiO emitting regions of the targets. We have estimated the angular size of the SiO photodissociation region for each target using the results of González Delgado et al. (2003). The photodissociation radius of most targets varies between 2$\farcs$5 and 10$''$, except that of AH Sco and KW Sgr, which is less than 1$''$. Hence, we requested C43-2 observations at an AR of $\sim$1$''$ (MRS ranging between 8$''$–10$''$; henceforth 'compact' or 'low resolution') for 15 out of 17 targets and in the two spectral setups that cover the SiO $J = 5 - 4$ and $J = 6 - 5$ lines. The CO $J = 2 - 1$ line is also covered in the same setup as SiO $J = 5 - 4$.

The 24 molecules identified in ATOMIUM can be separated into groups according to their chemical properties, or to their utility as probes of the wind kinematics and wind shaping mechanisms. Five molecules were observed in stars of all six pulsation types (CO, SiO, HCN, SO, and SO$_2$), and three of these (CO, SiO, and HCN) are universal tracers of the gas dynamics. Four other molecules (AlO, AlOH, TiO, and TiO$_2$) are suspected precursors in the initial dust formation process that occurs in the inner wind within a few $R_\star$ of the central star. Three molecules (SiS, H$_2$O, and CS) were observed in all but one of the pulsation types. Four (SO, SO$_2$, SiS, and CS) inform us about the sulphur budget (Danilovich et al. 2017), and one (NaCl) is a probe of the coupling of the chemistry and dynamics (Decin et al. 2016). Because of the central role of these 13 molecules in characterizing the physicochemical properties of the inner and intermediate winds, we found it useful to designate the 13 molecules as the 'primary' molecules. Hereafter CO, SiO, HCN, AlO, AlOH, TiO, and TiO$_2$, SO, SO$_2$, SiS, H$_2$O, CS, and NaCl are referred to as the 'primary molecules' in the ATOMIUM survey.

The primary molecules all have principal rotational transitions in spectral Band 6. Figure 1 shows the frequency coverage between 213.83 and 269.71 GHz, the frequency tunings (a–f; see also Table 2), and the atmospheric transmission for the range of precipitable water vapour (PWV) recorded during the ATOMIUM observations. The actual bandwidth within the total span of $\sim$56 GHz is approximately 27 GHz for the mid and extended configurations (after trimming the edges), and 13 GHz for the compact configuration. To ensure that all the principal transitions of the primary molecules were covered in the ATOMIUM survey, it was necessary to constrain the bandwidths of three of the spectral windows (spw 07, 08, and 13) to 1/2 the width of the 13 other spws because of: (1) the constraints of the ALMA Local Oscillator system on fitting the spws within the basebands; and (2) the need to minimise the total number of the local oscillator tunings for efficient use of observing time[5]. In all three array configurations, the line free channels (or about one half the total bandwidth) are available to image the millimeter-wave continuum.

A spectral resolution of $\sim$1.3 km s^{-1} provided sufficient resolution elements per line with typical full width at half maximum (FWHM) line widths ranging between 5–60 km s^{-1}, where the smaller line widths probe the wind acceleration region. The velocity widths of our spectral windows (spw) and channels are shown in Table 2.

To diagnose the (wide) velocity tails and hence extract the kinematical behaviour, a sensitivity of a few mJy/beam was needed (Decin et al. 2018). The most stringent constraint on the sensitivity was set by the metal oxides, most especially by AlO – the gaseous precursor of aluminum oxide (Al$_2$O$_3$) grains (Kamiński et al. 2016; Decin et al. 2017; Takigawa et al. 2017). We calculated the expected AlO line strength for each target, and aimed for a signal-to-noise ratio of >3. The sensitivity ranged from 1.5 mJy beam^{-1} to 5 mJy beam^{-1} for C43-8/C43-9 and C43-5/C43-6. For the SiO observations in C43-2, the sensitivity was 5 mJy beam^{-1}.

Standard ALMA observing procedures were followed, including system temperature and PWV monitoring. Bright, compact quasi stellar objects (QSOs) were used for calibration of the bandpass and flux scale; the latter was determined with respect to approximately fortnightly monitoring of Neptune or Uranus. Phase referencing was used with a nearby, compact quasar. A check source – that is to say, a known, compact source at a similar angular separation from the phase reference as the target – was also observed in the extended configuration. Table E.1 summarises the observations, including the phase reference sources used; see the ALMA Science Archive[6] for more details.

3.2. ATOMIUM data reduction

The ATOMIUM project is among the first to collect a large volume of ALMA data for a set of three different baseline configurations, including long baselines. A substantial effort was made to explore various calibration strategies to enhance the data quality.

---

[5] See the ALMA Cycle 6 Technical Handbook at `https://almascience.nrao.edu/documents-and-tools/cycle6/alma-technical-handbook`.
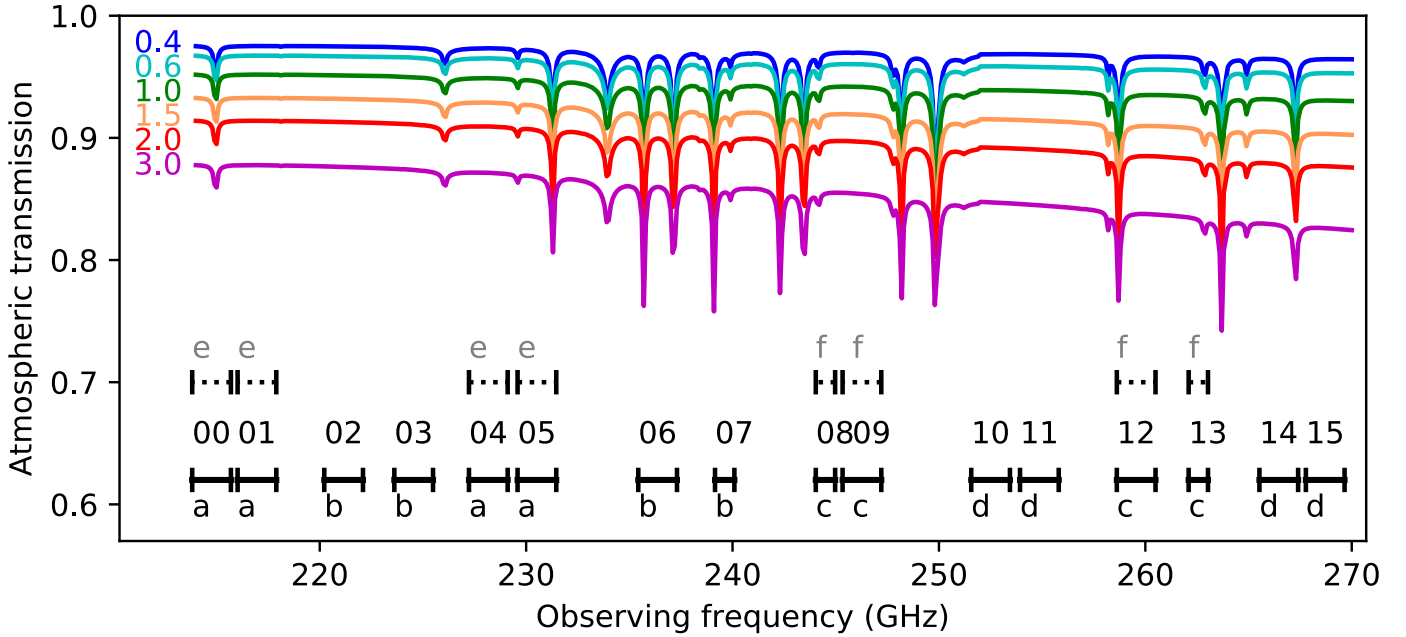
[6] `http://almascience.eso.org/aq/`

Fig. 1. Frequency coverage of the ATOMIUM project in each array configuration (see Sect. 3.1 and Table 2). Each black bar represents the frequency coverage of a spectral window (spw), labelled with the same index number as in our final released data products. The solid lines and letters a–d represent the frequency tunings for the medium and extended configurations; the dotted lines and grey letters e, f represent the frequency tunings for the compact configuration. The exact spectral coverage for each target depends on the adjustment to the assumed v_{LSR} on the dates of observation (see Table 1). Each frequency tuning covered 4 spws grouped as follows: [00,01,04,05], [02,03,06,07], [08,09,12,13], and [10,11,14,15]. The first (second) pair of spw in each frequency tuning corresponds to the lower (upper) sideband in which the channel numbering is in descending (ascending) frequency order. The coloured lines represent the atmospheric percentage transmission labelled by the precipitable water vapour (PWV), in mm.

In this section, we describe the standard data reduction methodology. The details on the calibration of the specific datasets for individual stars will be available in the ATOMIUM data release (see Sect. 4) and where needed, additional information will be provided in separate papers.

3.2.1. Processing each configuration

Each fully observed Scheduling Block (SB) was processed using the ALMA calibration and imaging Pipelines[7] (Humphreys et al. 2016) implemented in CASA[8] (the Common Astronomy Software Applications package), or in a few cases with manually steered scripts, where the end result was equivalent in the two procedures. The calibration pipeline applies all instrumentally derived calibration (e.g., from PWV measurements) as well as corrections derived from observations of calibration and phase-reference sources. The line free channels were initially identified from the visibility data and a linear fit to these was subtracted from the data. Data cubes were then made for each subtracted spw, and the line-free continuum was also imaged.

We inspected the web logs; occasionally a few instances of over- or under-flagging[9] were identified, but the former were too trivial to affect sensitivity significantly and the latter were remedied during our processing.

For each star, each full set of tunings in each configuration was processed by the following steps:

1. Two copies of the pipeline calibrated target data were split out: one at a 'continuum' spectral resolution of 15.625 MHz, and the other at a 'line' spectral resolution of 0.9765625 MHz which ranges from 1.09 to 1.37 km s^{-1} in velocity units. These were then concatenated to make continuum and line datasets containing the full spectral coverage for each star and array configuration. The concatenation task aligns the phase centre of each input visibility dataset with that of the one measured at the earliest date. The extended configuration data were all taken within 5 weeks, so any errors in the predicted proper motions would cause <1 mas discrepancy (see Sect. 3.2.3) and the self-calibration (see Step 5) takes care of relative alignment.

2. The Lumberjack[10] package was used to identify line free channels from the pipeline image cubes. The selection was adjusted to correspond to the channelisation of the continuum and line datasets, and checked interactively using the visibility data.

3. The continuum-only channels of the dataset were imaged. In most cases the continuum emission distribution was dominated by a compact peak, but at the highest resolution some stars were slightly resolved. Nonetheless the peak signal-to-noise ratio (S/N) was ≳100 for all the stars except SV Aqr where it was ~50.

4. The stellar peaks were offset by up to a few hundred mas from the predicted continuum positions (see Sect. 3.2.3). The measured position was used as the imaging field centre for further extended configuration images as the displacement could

Table 2. Velocity widths Δv and resolutions δv of the ATOMIUM observations.

spw	v_{central} (GHz)	Δv (km s^{-1})	δv (km s^{-1})	Frequency tuning
00	214.8	2598	1.36	a/e
01	217.0	2572	1.35	a/e
02	221.2	2523	1.32	b
03	224.6	2485	1.30	b
04	228.2	2445	1.28	a/e
05	230.5	2420	1.27	a/e
06	236.4	2360	1.24	b
07	239.7	1164	1.22*	b
08	244.5	1141	1.20*	c/f
09	246.3	2266	1.19	c/f
10	252.6	2209	1.16	d
11	254.9	2189	1.15	d
12	259.6	2149	1.13	c/f
13	262.6	1062	1.12*	c/f
14	266.5	2093	1.10	d
15	268.7	2076	1.09	d

Notes. The exact central frequency v_{central} depends on the adjustment to the assumed v_{LSR} on the dates of observation. Velocity widths are given using v_{central}. Due to Hanning smoothing in the correlator, the velocity resolution is 15% broader except for spectral windows (spw) marked *. These were observed in half the maximum bandwidth in order to fit within the frequency sidebands; the original velocity channel width was half that shown, and the additional averaging gives a final velocity resolution which is only 1% broader than the channel spacing. The letters a, b, c, d represent the frequency tunings for the medium and extended configurations; e, f represent the frequency tunings for the compact configuration.

be a significant fraction of the chosen image size. Mid and compact configuration images were made using the observing phase centres.

5. The clean components from the first continuum image were used as a starting model for self-calibration. This removes any small offsets between SBs due to differences in calibration or proper motion uncertainty, and improves the image quality. If the signal-to-noise ratio was sufficient, an image using a first-order spectral index provided a model for more cycles of self-calibration, including amplitude self-calibration. Fortunately, amplitude offsets are only significant above the noise in sources bright enough for self-calibration. In the case of continuum sources with complex structure, we checked that the apparent complex structure was not due to an incorrect model or inappropriate imaging parameters – for example, if a secondary, compact component was present, we investigated whether it remained after using a single point model. Once the optimum level of calibration was achieved, images with and without the primary beam correction were made.

6. The corrections described earlier in this section were also applied to the line data set, and we then checked the selection of line-free channels and subtracted the continuum using a first-order fit.

7. A spectral image cube for each spw and configuration was made large enough to encompass all detectable circumstellar emission at that resolution. Weighting for the optimum balance between sensitivity and the required resolution resulted in a synthesized beam θ_{B} that varied slightly depending on target elevation and exact antenna positions. Cubes were made with and without the primary beam correction. Automasking was used for

the mid and compact configurations, and the masks derived for mid were also used for the extended configuration.

8. Spectra were extracted for a range of circular apertures (as appropriate for the configuration resolution and image size), centred on the stellar peak.

The properties of each continuum and cube image are listed in Tables E.2 and E.3, respectively. The values for the maximum recoverable scale (MRS) apply to both line and continuum for a given configuration and target, although the imaging fidelity for cubes is slightly worse due to the narrower coverage of the visibility plane per channel as compared to the broadband continuum.

3.2.2. Accuracy

In this section, we cover the overall accuracy of the ATOMIUM observations. Astrometric position uncertainties in the ATOMIUM data arise from several factors:

– Transferring phase corrections from the reference source to the target is affected by the difference in the angular separation and in the time between the observations of the phase reference and the target. Following expressions from Taylor et al. (1999), it can be estimated from the magnitude of the initial target self-calibration phase corrections and for the 43 antennas in use, that the position error is roughly equal to: (synthesised beam) $\times$ (phase error in degrees/1450). The phase corrections are typically $\sim$40°, and the uncertainty is $\sim\theta_{\text{B}}/40$ which corresponds to $\sim$0.7, $\sim$6, and $\sim$25 mas for the extended, mid, and compact configurations.

– The phase reference position is usually accurate to <1 mas as most phase reference source positions are taken from the Very Long Baseline Interferometer (VLBI) calibrator catalogues: see the ALMA Calibrator Source Catalogue[11].

– Position measurement accuracy for a compact source such as the star is given by $f \times \theta_{\text{B}}/(S/N)$ where $f = 0.5$ is appropriate for a well-filled array, tending to $f = 1$ for the extended configuration. S/N is the signal-to-noise ratio, typically $\gtrsim 100$, leading to stochastic position errors of no more than $\sim$0.25, $\sim$2, and $\sim$5 mas for the extended, mid, and compact configurations.

– Antenna rms position errors now contribute $\sim$1 mas astrometric errors (for typical target-calibrator separations of around 6 degrees). The measurement technique involving QSO observations described in Alma et al. (2015) has since been improved by the addition of more weather stations across the ALMA tracks which refine the measurements of the atmospheric delay.

Thus, the total astrometric uncertainty has typical values of 2, 7, and 26 mas for the extended, mid, and compact configurations. This is consistent with the typical extended-configuration check-source position errors of 1–5 mas. The stellar positions used for astrometry were measured before any self-calibration as this cannot improve the astrometry.

The faintest stars are the most difficult case for self-calibration, and self-calibration was only performed for the phase with a solution interval of a single scan. This removes errors due to the phase-reference-target angular separation and inconsistencies between antennas – at least halving the phase errors. A residual 20° phase error would give a 4% amplitude error. The direct causes of amplitude errors fluctuate more slowly than for phase errors, so the solution transfer has a smaller uncertainty.

The ALMA flux density scale has an uncertainty of up to 5% in Band 6 due to the variability of QSOs in between monitoring

---

[11] https://almascience.eso.org/sc/

intervals. After the data reduction was completed, a problem was identified with the T_{sys} normalisation that might affect the flux scales in a channel dependent way[12]. Using scripts provided by ESO, we confirmed that – in the example of the CO $J = 2-1$ line observed in KW Sgr in the mid configuration – the magnitude of the effect is only ∼2%.

Each of our targets was observed several times separated by months, with uncertainties at each epoch, so the total amplitude scale error is at least 10% (to be analysed in more detail in future papers).

Each channel is labelled with its central frequency and the only significant uncertainties in v_{LSR} arise from poorly known rest frequencies for a few little-studied species.

3.2.3. Combining configurations

In order to combine the mid, extended and (if used) compact configurations, the data sets have to be aligned in position and flux density scale. The observing schedules were prepared using HIPPARCOS-based positions and proper motions. The highest proper motions are ∼70 mas yr^{-1}, referenced to epoch 2000, and by the time of the observations, the offsets from the predicted positions were up to a few hundred mas, suggesting errors of up to 10 mas yr^{-1}. The mid and extended configurations completed so far were taken up to 9 months apart, so the alignment error could be a significant fraction of the extended configuration resolution, requiring position corrections before combination. Future comparisons between positions derived from ATOMIUM and *Gaia* might lead to improved accuracy.

After applying all self-calibration to the data taken in each configuration, the continuum visibility data were split out and the line channels flagged (to allow later averaging). We used task FIXVIS to rotate the phase centre of each visibility data set to the position of its continuum image peak. We took the peak position measured from the extended configuration image (with the highest astrometric accuracy), as the reference position and used task FIXPLANETS to re-label the centre of the mid and compact configuration data sets to this position. All positions are given in ICRS.

We then plotted amplitude against *uv* distance (i.e., projected baseline lengths) for each configuration, using the data sets with the peak at the phase centre, averaging all continuum channels, to investigate whether the amplitude scaling was consistent on baseline lengths common to all configurations. The situation is complicated because, as well as possible flux scale errors of order 10%, the photospheric pulsation or the formation of dust could cause a flux variation of a few percent, and the extended line emission is likely to be much less affected on the same time scale. In three cases the emission in the extended configuration was >10% brighter, probably due to a known bias in the flux scale calibration of long baselines with phase noise, and we rescaled these data to be consistent with the flux densities in the other configurations. The position-corrected continuum data were then concatenated giving each data set equal weight. We imaged the combined data applying a *uv* taper, equivalent to a Gaussian beam of 20 mas at the FWHM, in order to avoid artefacts owing to the relatively sparse coverage on the longest baselines, giving θ_B ∼ 50 mas.

The calibrated line data were then similarly split out, the position corrections applied, and the data concatenated and image cubes made. All spw were imaged using an image size

of 4″ and multi-scale clean, and giving higher weight to the largest scales. This maintained high resolution whilst ensuring that all scales in the data were imaged smoothly, avoiding over-emphasied, spotty small scales owing to the higher sensitivity of the extended observations. The emission of a few lines in the ground vibrational state was extended over more than 4″. In the example of the ^{12}CO $J = 2 - 1$ line we made a 40″ image to the 0.2 primary beam sensitivity level. The size (8192×8192 pixels^2) and time taken to clean made it impractical to make such images for more than a few hundred channels for each target.

4. ATOMIUM data release

An important motivation for the ATOMIUM survey was to provide the community with a set of accurately calibrated ALMA data of evolved stars, which – on the grounds of its homogeneous setup – can advance our insights into dynamical and astrochemical processes in various astrophysical media, and spark related research. To that end, we will release a suite of data products which go beyond the normal standard contents in the ALMA Archive where all the ATOMIUM data are now available.

4.1. Data products

The enhanced data products for each star will include: (1) the visibility data self-calibrated as described in Sect. 3, with all tunings aligned per configuration, and the data sets from the three configurations combined; (2) consistent image data cubes of manageable size, covering the full spectral range; (3) continuum images; and (4) spectra extracted at a range of apertures. Documentation describing the data products will be provided, and all the principal data products will be available in the ALMA Archive standard format via the ALMA Large Programme web pages in 2022. In addition, we will provide the parameters of all the spectral lines observed in the three array configurations, and a Table with the parameters of all the unidentified lines. The spectral and imaging templates that will be created will allow the astronomical community to explore the entire dataset, and to exploit these libraries in other research domains which will in turn serve as a legacy for the community[13].

4.2. Example of the OH/IR star IRC−10529

In the following discussion we refer to the example of the OH/IR star IRC−10529 for each of the data products included in the ATOMIUM data release. This target was chosen because the morphology is not too complex (Decin et al. 2020), it is rich in molecular spectral lines, and the data can be used for a straightforward demonstration of the ATOMIUM data products and their role for scientific inference[14].

– Continuum image: The low, medium, and high spatial resolution continuum maps of IRC−10529 are displayed in Fig. 2. For each resolution, the emission is spatially resolved with deconvolved sizes of 0.″348 × 0.″310, 0.″085 × 0.″046 and 0.″015 × 0.″011 for the compact, mid, and extended

---

[12] https://almascience.eso.org/news/amplitude-calibration-issue-affecting-some-alma-data

[13] For announcements and links to products see: https://fys.kuleuven.be/ster/research-projects/aerosol/atomium/atomium

[14] Many OH/IR stars were first observed in the two micron Caltech (IRC) sky survey (Neugebauer & Leighton 1969), and were subsequently shown by radio astronomers to have intense lines from OH and H$_2$O masers. Most of the stars in the IRC catalog are M-type stars which have high mass-loss rates.

C.A. Gottlieb et al.: ALMA ATOMIUM Survey

Fig. 2. Continuum-maps of IRC −10529. Low (*left panel*), medium (*middle panel*), and high (*right panel*) spatial resolution continuum map. Contours (in orange) are indicated in steps of (3, 6, 10, 100)×σ_{rms}^{cont} (see Table E.2). The ALMA synthesized beam is shown as a white ellipse in the lower right corner of each panel (see Table E.2).
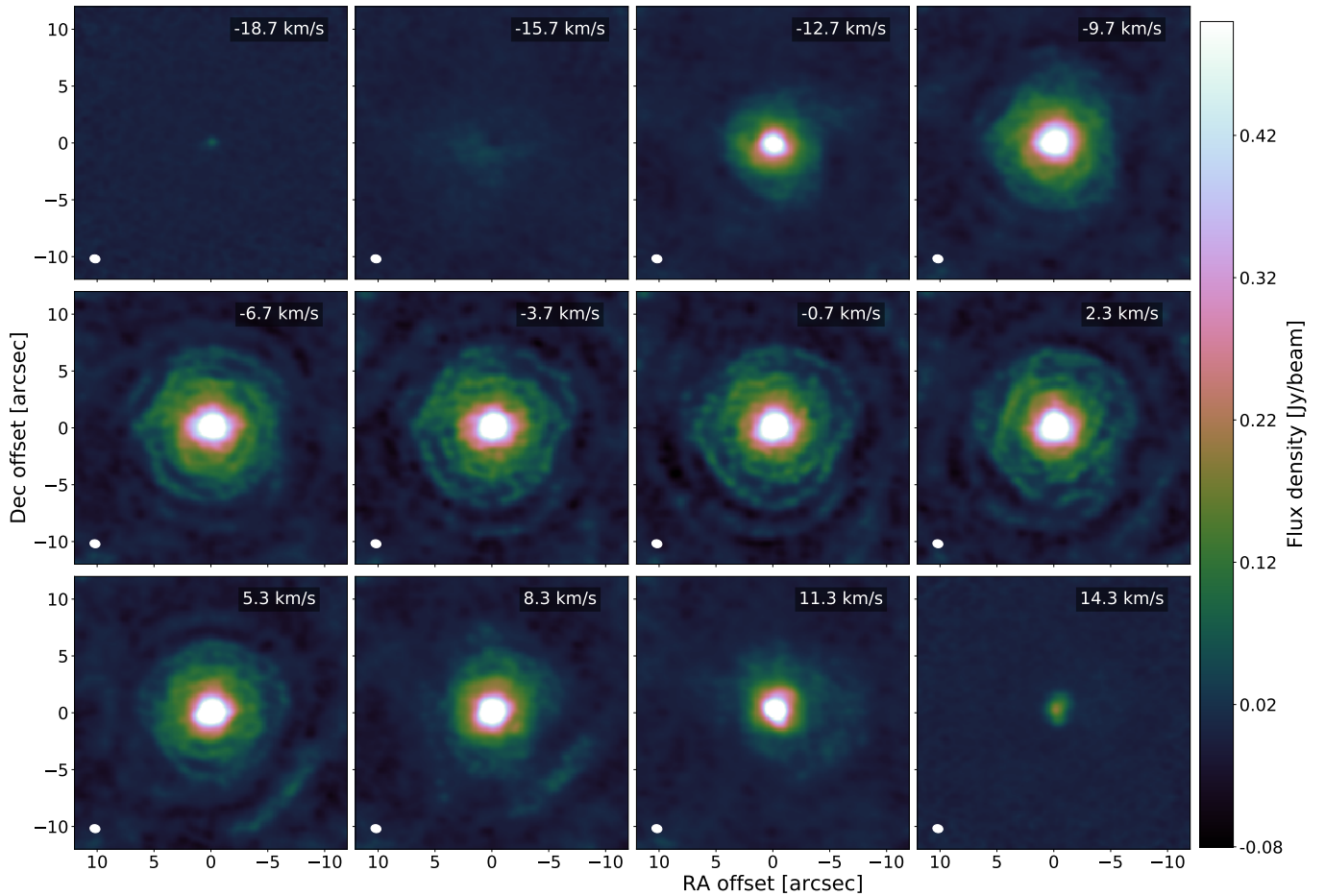
Fig. 3. Low resolution channel map of ^{12}CO $v = 0$ $J = 2 − 1$ in IRC −10529. The peak of the continuum emission is at (0,0). The velocity (in km s^{-1}) is with respect to the stellar velocity of −16.3 km s^{-1} (see the last column in Table 1), and is indicated in the upper right corner of each panel. The ALMA synthesized beam is shown as a white ellipse in the lower left corner of each panel (see Table E.2). The offsets in right ascension and declination are with respect to the peak of the continuum emission.

configuration respectively. The peak continuum flux densities are 6–7 mJy beam^{-1} in all configurations. For a star with effective temperature of 2700 K and angular diameter of 6.47 mas at a distance of 760 pc, the stellar blackbody contribution in the selected spectral windows is ∼3.7 mJy. Hence roughly 50–60% of the continuum flux can be attributed to dust emission and the radio photosphere.

– Channel maps: Figure 3 shows the low resolution channel map of ^{12}CO $J = 2 − 1$ at 230.538 GHz and a lower state energy (E_{low}) of 5.53 K. We could not find any measurements with single antennas of the ^{12}CO $J = 2 − 1$ $v = 0$ line in IRC-10529 in the literature, although there are such measurements for other sources in the ATOMIUM sample. Therefore to estimate the total amount of the CO flux recovered for this source, we
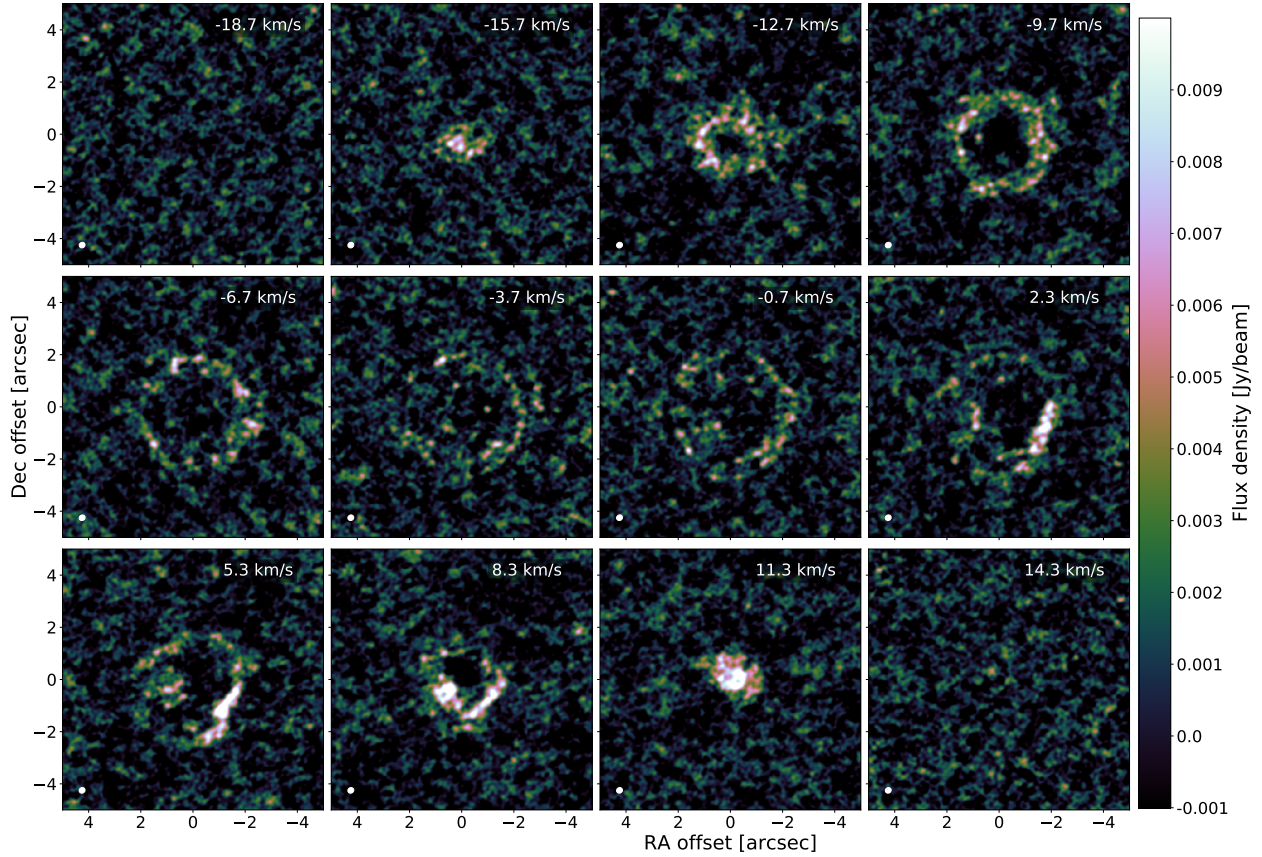
Fig. 4. Medium resolution channel map of SO$_2$ $v = 0$ 11(1,11)−10(0,10) in IRC −10529. See Fig. 3 caption. The emission shows a hollow shell structure located at a radius of ~2″.5.

referred to the observations of the $J = 1 − 0$ line with SEST (Nyman et al. 1992) and the $J = 3 − 2$ line observed with APEX-2a (De Beck et al. 2010), and to the Jy/K factors from the APEX/SEST web site[15] and R. Laing (personal communication). We estimate an average flux density of ~44 Jy for the $J = 2 − 1$ transition on the basis of a peak flux density of 16.2 Jy for the $J = 1 − 0$ line and 71 Jy for the $J = 3 − 2$ line, on the assumption that a flat-topped approximation to the profiles is adequate owing to the other uncertainties. ALMA recovered a peak flux density of 25 Jy for the $J = 2 − 1$ line, implying that we recovered >55% of the most extended emission (and probably all the emission of the compact front and back caps).

As discussed by Decin et al. (2020), the data show the prevalence of a broken spiral-like structure which can be explained by binary interaction caused by an as yet undetected (sub-)stellar companion. As an example of a medium-resolution channel map, we show the emission of the $11_{1,11} − 10_{0,10}$ transition of SO$_2$ (at 221.965 GHz and $E_{low} = 49.71$ K), where the brightness distribution is composed of a hollow shell structure located at a radius of ~2″.5 (Fig. 4). A similar shell-like structure was previously seen for SO in oxygen-rich AGB stars with a high mass-loss rate by Danilovich et al. (2016), but the limitations of their data did not allow these authors to study the spatial distribution of SO$_2$. The current ALMA data now confirm the emission of both SO and SO$_2$ can have a shell-like structure, in accord with recent chemical model predictions (Van de Sande et al. 2018b;

---

[15] https://www.apex-telescope.org/telescope/
efficiency/index.php.old
https://www.apex-telescope.org/sest/html/
telescope-instruments/telescope/index.html

Danilovich et al. 2020b). The high-resolution channel map of the SiO $J = 5 − 4$ emission (at 217.105 GHz) is displayed in Fig. 5. Although the channel map is challenging to interpret at face value, the moment1-map has proven to be very valuable for understanding the velocity vector field in the inner wind region of various ATOMIUM sources (Decin et al. 2020), which (as shown in the next item) is illustrated very nicely in IRC−10529.

– Moment1-map: First moment (or moment1) maps are utilised as a tool for visualising structures in the velocity fields. The maps are obtained by

$$M_1 = \frac{\sum_{v_{blue}}^{v_{red}} I_v \, v_v \, dv}{\sum_{v_{blue}}^{v_{red}} I_v \, dv},$$ (1)

with the velocity channels centred around v_{LSR}. We illustrate the strength of this visualisation for the low, medium, and high spatial resolution data of the SiO $J = 5 − 4$ emission of IRC −10529 (see Fig. 6). The line velocity map exhibits distinct red-shifted and blue-shifted components, which is the classical signature of rotation or a bipolar outflow (Kervella et al. 2016; Decin et al. 2020).

– Spectra and line identifications: Shown in Figs. 7 and B.1–B.3 are the 16 spectral windows (spw) of IRC−10529 observed with medium resolution (mid configuration). The spectra were extracted with an aperture radius of 1″.8 in the upper part of the panels and 0″.2 in the lower part, and are plotted on a common frequency scale. The line identifications shown in the upper panel were made using the spectral line catalogues of the Cologne Database for Molecular Spectroscopy (CDMS, Müller et al. 2001, 2005; Endres et al. 2016) and the Jet
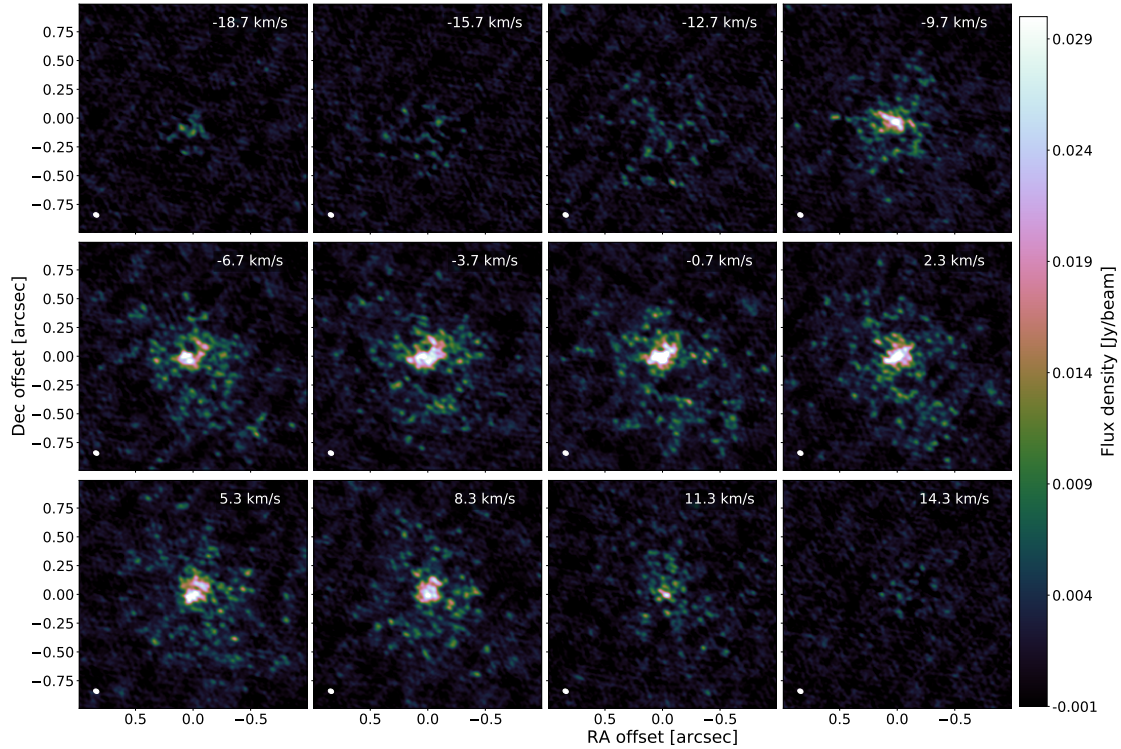
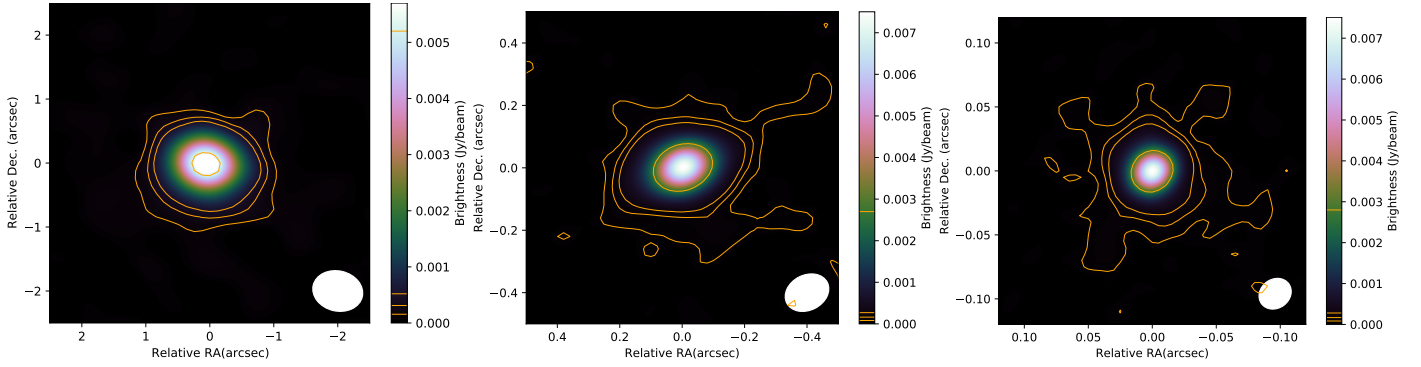**Fig. 5.** High resolution channel map of SiO $v = 0$ $J = 5 - 4$ in IRC -10529. See Fig. 3 caption.
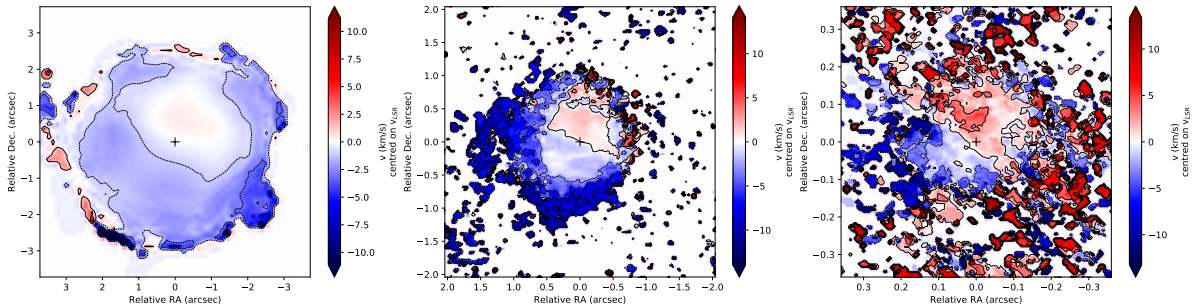
Fig. 6. SiO moment1-maps of IRC -10529. Low (*left panel*), medium (*middle panel*), and high (*right panel*) spatial resolution moment1-map of SiO $v = 0$ $J = 5 - 4$. The black cross indicates the position of the AGB star. The distinct spatial difference between red and blue-shifted velocity components indicates signs of rotation or bipolarity in the inner $\sim 0\!\!''5$ region of IRC -10529.

Propulsion Laboratory (JPL, Pickett et al. 1998), and by referring to prior spectral line surveys. In all, 60 lines from 12 molecules are observed in IRC-10529 in the mid configuration. These include CO, SiO, HCN, SO, SO_2, SiS, CS, H_2S, H_2O, NaCl, KCl, and PO. Some molecular features, such as those of AlOH and OH (although not shown here), are only visible in the extended configuration, because the longer on-source observing time provides higher sensitivity to compact emission. In addition, there are a couple of weak features whose carriers have not yet been identified. The parameters of the molecular lines in IRC-10529 will be presented in the Molecular Inventory paper (Wallström et al., in prep., see Sect. 2.1.2).

5. Result – Wind kinematics of the ATOMIUM AGB and RSG sources

5.1. Background

The ATOMIUM data introduced in Sect. 2.1 provides a unique opportunity for studying the wind kinematics in the circumstellar envelope of the 17 AGB and RSG sources. Here we use the data to understand where the wind is initiated, how fast it is accelerated, and if a terminal velocity is reached at some distance from the central star (Sect. 2.1.1). These questions can be answered by retrieving the wind velocity profile by analysing the extent of the emission from an ensemble of molecular transitions (for examples see Decin et al. 2015, 2018).

When the ALMA proposal was submitted, it was generally expected that most of the ATOMIUM sources, with the exception of W Aql, π^1 Gru, and R Hya (Danilovich et al. 2015b; Feast 1953; Mason et al. 2001), were single stars. However, even for these three AGB sources, the known companion resides at a separation >150 au so its gravitational field should not disturb the wind kinematics in the inner wind region ($r \lesssim 10-30\,R_\star$) where the wind is initiated. Hence, even for these three sources, the ATOMIUM data should allow us to study the efficiency of the wind initiation.

A first highlight of the ATOMIUM programme, however, was that no source displays a smooth spherical wind. Instead, the observed morphologies include bipolar geometries with
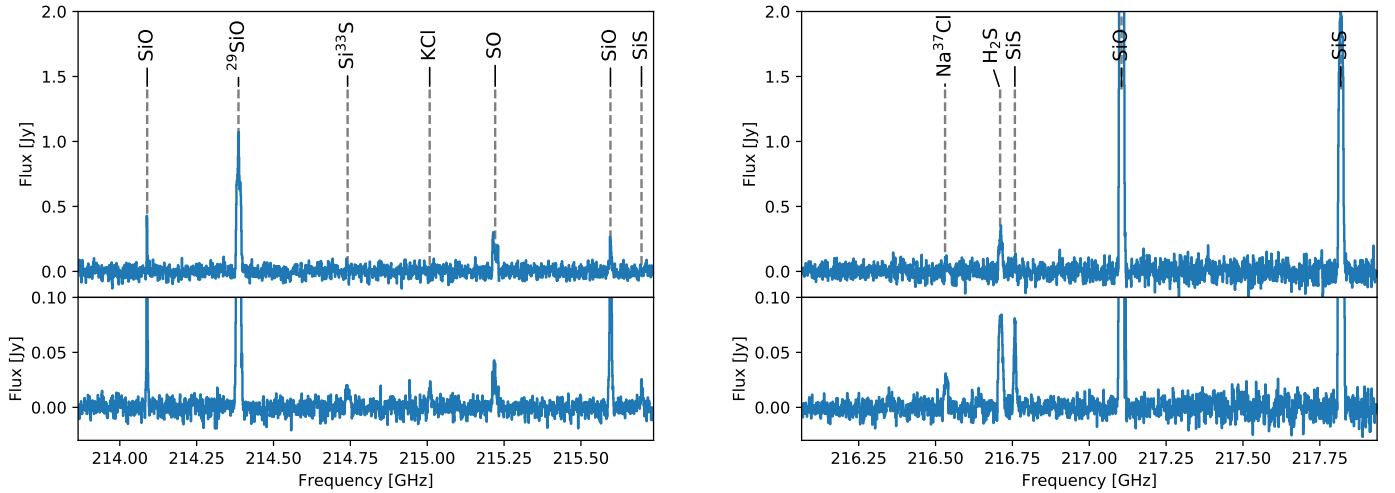
Fig. 7. Spectra of IRC−10529. Spectra of IRC−10529 for cubes 00 (*left panel*) and 01 (*right panel*) observed in the medium-resolution configuration with ALMA. The spectra were extracted with an aperture whose radius is 1″8 (upper part) and 0″2 (lower part). The frequency scale refers to the rest frequency adjusted to the v_{LSR} of the star indicated in Table 1. Plots for the remaining cubes 02–15 are shown in Figs. B.1–B.3.

a central waist, equatorial density enhancements (EDE) and disk-like geometries, spiral-like structures, arcs, and 'eye'-like shapes. These morphologies, supported by a population synthesis approach, led to the conclusion that most ATOMIUM sources are part of a binary system, although the stellar or planetary properties and the orbital parameters of the companion remain unknown (Decin et al. 2020). It is expected that very-low-mass objects, including brown dwarfs and large planets, play a larger role than previously assumed. Therefore the ATOMIUM data renders a crucial observational benchmark for both binary-star and single-star theoretical simulations of the wind dynamics of AGB and RSG sources. Even though (sub-)stellar companions might be omnipresent, if the mass of the companion is low or the separation is large, there will be little departure of the velocity streaming lines from radial motion and the observed wind kinematics can guide single-star models. Moreover, even if a companion disturbs the radial velocity pattern substantially, the effect is 'localised' and the velocity pattern retains its radial character farther out in the wind. As discussed by El Mellah et al. (2020), any density structure imprinted in the wind will then expand in a self-similar way.

For the single-star and binary-star models, the question about the impact of resolved-out flux on the observables needs to be assessed. This mainly affects the low-excitation CO emission, however measurements of the velocity measure are not affected. Our observations are sensitive to MRS ≳8″ (Sect. 3.2.3), therefore all but the smoothest emission is detected. The perturbations and anomalous velocities we examine occur within 4″ of the star (as do the extreme velocities from a spherical shell). so resolved-out flux does not affect an investigation of the cause of perturbations. A next step entails assessing the mass fraction of the wind that is diverted for the binary-star models. To answer that question, single antenna observations are currently being acquired and analysed (Jeste et al., in prep.).

Single star models. It is generally accepted that the winds of AGB stars are radiation driven. Pulsations lift material to greater heights where the temperature is ≲1800 K, allowing gas to condense into grains (Hoyle & Wickramasinghe 1962; Gail & Sedlmayr 2013). The absorption of stellar radiation by these newly formed dust grains creates a net force that can overcome gravity (Höfner & Olofsson 2018). The gas is then accel-

erated beyond the escape velocity. This is expressed in the radial momentum transfer equation (Goldreich & Scoville 1976)

$$v(r)\frac{dv(r)}{dr} = (\Gamma(r) - 1)\frac{GM_\star}{r^2}, \qquad (2)$$

where $v(r)$ refers to the gas velocity at a radial distance r from the star, $M_\star$ the stellar mass, G the gravitional constant, and $\Gamma(r)$ the ratio of the radiation pressure force on the dust to the gravitational force that can be written as (Decin et al. 2006)

$$\Gamma(r) = \frac{3v(r)}{16\pi\rho_s cGM_\star \dot{M}(r)} \iint \frac{Q_\lambda(a,r)L_\lambda \dot{M}_d(a,r)}{a[v(r) + v_{drift}(a,r)]} d\lambda \, da, \qquad (3)$$

with ρ_s the specific density of dust, c the speed of light, $\dot{M}$ the gas mass-loss rate, $\dot{M}_d$ the dust mass-loss rate, $v_{drift}(a,r)$ the drift velocity of a grain of size a, $Q_\lambda(a)$ the dust extinction efficiency, L_λ the monochromatic stellar luminosity at wavelength λ. A solution for the gas velocity as derived from solving the momentum equation (Eq. (2)) for IK Tau is shown as the full black line in Fig. 8. If the grain properties change with radial distance so that, for example, $Q_\lambda(a,r)$ increases, a gradual wind acceleration at larger distances can arise (Chapman & Cohen 1986). In general, the particular behaviour of $Q_\lambda(a,r)$ has a strong influence on the wind acceleration, as discussed in detail by Netzer & Elitzur (1993).

The wind initiation mechanism for RSG stars is less well understood. Mechanisms based on turbulent pressure in combination with radiation pressure on molecular lines or freshly synthesized dust grains and magneto-accoustic waves are invoked, or a combination of the above (Josselin & Plez 2007; Thirumalai & Heyl 2012). In general, these alternative processes might also support the AGB stellar wind, although their role in driving the wind is still very much debated (Wood 1990; Gustafsson & Höfner 2003). Solutions for the momentum equation (Eq. (2)) indicate that the velocity profile of AGB and RSG winds can be approximated by the so-called β-type velocity law (Lamers & Cassinelli 1999)

$$v(r) = v_0 + (v_\infty - v_0)\left(1 - \frac{R_{dust}}{r}\right)^\beta, \qquad (4)$$

with r the distance to the star, v_0 the velocity at the dust condensation radius R_{dust}, and v_∞ the terminal wind velocity (see red dashed line in Fig. 8).
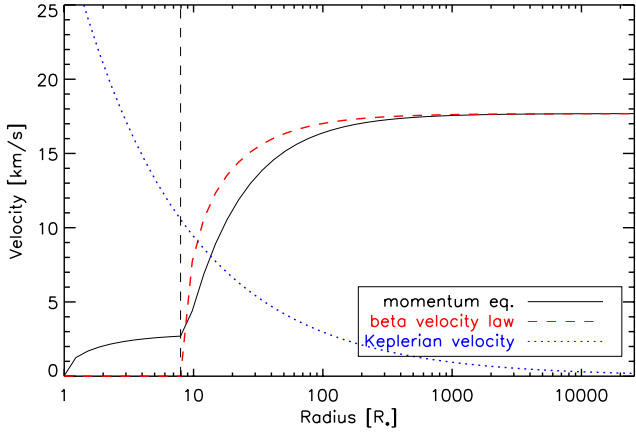
Fig. 8. Illustration of different velocity laws. The full black line at radii beyond $8\,R_\star$ represents the solution of the momentum equation (Eq. (2)) derived for the wind velocity profile of the oxygen-rich AGB star IK Tau (Decin et al. 2010b); for the region between $1–8\,R_\star$ a beta-velocity law with $\beta = 0.5$ is used (Decin et al. 2006). The red dashed line illustrates the β-velocity law (Eq. (4)) for $\beta = 0.5$, $v_0 = 2.7\,\mathrm{km\,s^{-1}}$, $v_\infty = 17.68\,\mathrm{km\,s^{-1}}$, and the vertical black dashed line indicates R_{dust} at $8.6\,R_\star$. An almost perfect fit to the velocity as derived from the momentum equation (Eq. (2)) would be obtained for $\beta = 1$. The dotted blue line represents the Keplerian velocity law for material bound to a star of mass $1\,M_\odot$.

Fig. 9. 3D hydrodynamical simulation for a binary system containing a mass-losing AGB star. Slices of density are shown, in units of the density at the sonic point, in the orbital plane (*left column*) and in the plane containing the orbital axis and the line joining the two bodies (*right column*). The dimensionless parameters for this simulation are the mass ratio, $q = M_1/M_2 = 1$; the ratio of the terminal to orbital speed $\eta = v_\infty/v_{\mathrm{orb}} = 2$, the dust condensation radius filling factor $f = R_d/R_{R,1} = 20\%$ (with $R_{R,1}$ the Roche lobe radius of the primary), and the β exponent setting the steepness of the velocity profile here being 5 (El Mellah et al. 2020). For a dust condensation radius set to $3\,R_\star$, the dimensionless parameters translate into an orbital separation of $\sim 35\,R_\star$. Due to binary interaction, a spiral shock is created in the circumstellar envelope. The spiral structure is readily recognised in the density slice in the orbital plane and the width of the successive spiral windings can be deduced from the density arcs in the edge-on view.

The beta velocity law assumes that the CSE is physically homogenous, apart from a decrease in number density and temperature as a function of distance from the star. Low values for β describe a situation with a high wind acceleration. For carbon-rich AGB stars, β is around 0.5 (Decin et al. 2015) owing to the very opaque carbon dust grains that facilitate photon momentum transfer. Recent observational studies indicate that the wind acceleration for oxygen-rich AGB stars might be much lower than for carbon-stars, and values of β between $1 - 5$ have been derived (Decin et al. 2010a, 2018; Khouri et al. 2014; Van de Sande et al. 2018a). The cause for this slow wind acceleration is not yet fully understood. The fact that oxygen-rich dust grains (such as aluminium oxides and silicates) are more transparent than carbon-rich grains offers part of the solution. Using colour-dependent absorption, it has been shown that silicates become progressively more iron-rich (hence opaque) as the material gets farther from the star (Woitke 2006; Bladh & Höfner 2012). However, even then we cannot explain why for some sources the observed wind acceleration continues beyond ~ 50 stellar radii where the densities are too low for efficient momentum exchange between the gas and dust particles (see, for example, IK Tau in Fig. 9 of Decin et al. 2018). Fractal grains within an inhomogeneous clumpy wind increase the radiation pressure efficiency and can potentially explain the more gradual but ultimately more forceful acceleration (Decin et al. 2018).

Binary star models. As discussed in Decin et al. (2020), we expect that most of the ATOMIUM sources are part of a binary system. Binary interaction with a (sub-)stellar companion results in distinct non-spherical wind geometries that are readily probed in CO and SiO channel maps. Observationally derived wind profiles can provide a means for constraining the presence and the properties of a companion. Compared with a single-star model, the companion will perturb the radial character of the velocity vector field as expressed, for example, in the momentum equation (Eq. (2)) or in the β-velocity law (Eq. (4)). For example,

in the case that the companion induces the formation of a Keplerian disk-like structure, the tangential velocity component is given by $\sqrt{G\,M_\star/r}$, with G the gravitational constant, $M_\star$ the mass of the AGB star to which the disk is gravitationally bound, and r the radial distance (Kervella et al. 2016, see blue dotted line in Fig. 8). In addition, the companion's gravity lowers the effective gravity felt by a particle driven from the primary AGB star, which can lead to a local enhancement of the velocity amplitude. Based on a 3D hydrodynamical simulation for a binary system containing a mass-losing AGB star (Fig. 9; El Mellah et al. 2020), we illustrate this effect in Fig. 10. In this simulation, the wind is initially accelerated from the primary star following a β-velocity profile with $\beta = 5$ (see black dashed curve in Fig. 10, illustrating the single-star model). The presence of the secondary object impacts the velocity profile; see dotted lines in Fig. 10. The first up/down peak in the radial velocity profile in the direction of the secondary (blue dotted line in Fig. 10) is due to the wind being first accelerated, but then dissipating most of its radial kinetic energy in the spiral shock, and having to be re-accelerated from scratch. To a lesser extent the same phenomena are apparent each time the radial ray crosses the spiral shock, hence the oscillating motion around the mean isotropic profile. Notice also that, as expected, the blue and red profiles oscillate with almost opposite phases. The isotropic velocity profile (black dotted line in Fig. 10) is then the average over all azimuthal and longitudinal angles of the velocity profile. In the example shown here, the isotropic velocity profile has a wave-like character, in which the first peak indicates the orbital separation and the higher harmonics are linked to the spiral-arm crossing. As we discuss below, the velocity profile of W Aql might be an example of the binary-induced effect described here.

5.2. Methodology

To constrain the wind kinematics of the ATOMIUM sources, we followed the same methodology described in Decin et al. (2015) and Decin et al. (2018), which was augmented with several
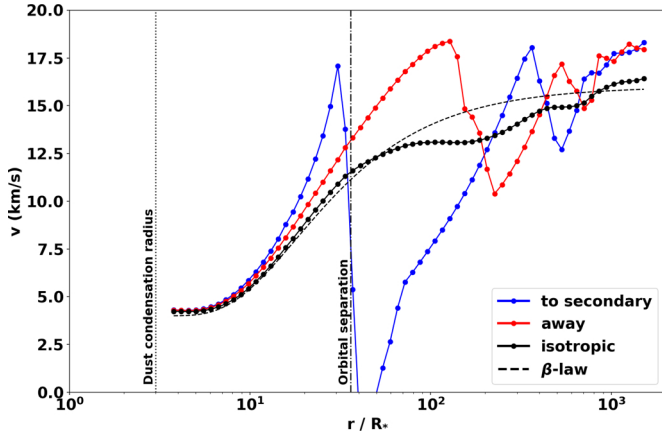
Fig. 10. Illustration of the impact of a binary companion on the velocity field. Given the simulations shown in Fig. 9 (El Mellah et al. 2020), the dotted black line represents the 1D isotropic radial velocity profile (w.r.t. the star). The dotted blue line is the radial velocity profile in the direction of the secondary, and the dotted red line is the radial velocity profile in the direction opposite to the secondary. For comparison, the dashed black curve illustrates the β-velocity law (Eq. (4)) for $\beta = 5$ representing the single-star situation. For better comparison with the observed velocity profiles (Sect. 5.2), the same figure but with a linear x-axis is shown in Fig. A.1. See text for more details.

additional steps. Figures A.2–A.3 illustrate the methodology for the SiO $J = 6 - 5$ and NaCl $J = 20 - 19$ transition observed in the medium-resolution configuration of IRC -10529.

1. In the first step, the spectrum of each molecular transition was extracted for a range of circular apertures. The minimum diameter of the extraction aperture was the major axis of the synthesized beam ('b_{maj}', see Table E.3), the maximum diameter was the MRS (see Table E.3), where the step size was $2 \times b_{maj}$.

2. The velocity of the blue and red wings[16] was determined for all extraction apertures. Accounting for the noise around the line spectrum (σ_{line}), the blue and red wing velocity were taken as the closest points to the line centre for which the flux was less than $3 \times \sigma_{line}$. These sensitivity-limited velocity widths are likely the lower bounds. The maximum of these numbers in absolute values was retained as the wind 'velocity measure' for the transition. The uncertainty in the velocity measure was taken from the spectral resolution of the data.

3. We then computed the zeroth moment map (integrated intensity or moment 0 map) of each line (between the measured red and blue wing velocities) and measured the angular FWHM by fitting a 2D Gaussian profile to the moment 0 map using the Levenberg–Marquardt algorithm. If the least-squares minimisation was unsuccessful, the molecular transition was not retained for further analysis. This led to a significant reduction in the number of transitions retained for the analysis of the kinematical behaviour. This particularly affects transitions with low signal to noise ratios and/or high upper energy levels which are associated with having a small angular extent. Transitions whose moment 0 maps differ significantly from a 2D Gaussian profile – such as the SO_2 distribution shown in Fig. 4 – were not retained after this step.

3. If the FWHM of the fitted 2D Gaussian was comparable to the axes of the synthesised beam (b_{min}, b_{maj}; see Table E.3), the

---

[16] Negative velocities (i.e., blue shifted) with respect to the v_{LSR} represent material coming towards the observer, and positive velocities (i.e., red shifted) with respect to the v_{LSR} represent material receding from the observer.

non-deconvolved extent was taken as an upper limit to the distribution of the species. For transitions for which the FWHM of the fitted 2D Gaussian was larger than the synthesised beam, we deconvolved the beam. As in Decin et al. (2018), we assumed that the spatial FWHM of the molecular emission zone represents the dominant line formation region.

4. In the case of successful least-square minimization, the covariance matrix was used to estimate the variance of the FWHM (σ_{FWHM}). Accounting for the interferometric capabilities of ALMA, the total accuracy of the measured size of the emission is then given by

$$\sigma_{ext} = \sqrt{\sigma_{FWHM}^2 + \left(\sqrt{2} * K * \theta_B / S/N \right)^2}, \quad (5)$$

where the S/N is the signal-to-noise ratio of the moment 0-map, θ_B the beamsize as given by (b_{min}, b_{maj}), and K is 0.5, 1, or 1.5 for the low, medium, and high spatial resolution data (Condon 1997; Taylor et al. 1999).

5. In the final step, the outcomes of the analysis of the velocity versus aperture information extracted from the low, medium, and high spatial resolution data were merged to produce a single output: for transitions in which the emission zone could be deconvolved in observations at various spatial resolution, the largest velocity measure and largest extent (often measured by the observation at the lowest spatial resolution) were retained. This should ensure that the impact of resolving out flux was kept to a minimum. In addition, blended lines were removed from the sample.

Our analysis provides a unique view of the wind kinematics of 17 oxygen-rich AGB and RSG sources. The outcome of this analysis for IRC -10529 is shown in Fig. 11, and that of the prototypical source W Aql is shown in Fig. 12. The wind dynamics for the 15 other sources are in Appendix C (see Figs. C.1–C.15). Until now similar velocity profiles were only obtained for the carbon-rich AGB star CW Leo ($\dot{M} = 1.5 \times 10^{-5}\ M_\odot\ yr^{-1}$), and the two oxygen-rich AGB stars R Dor ($\dot{M} = 1 \times 10^{-7}\ M_\odot\ yr^{-1}$) and IK Tau ($\dot{M} = 5 \times 10^{-6}\ M_\odot\ yr^{-1}$) (Decin et al. 2015, 2018).

One of the obvious limitations of the method is that we use Gaussian fits to the zeroth moment maps to determine the size of the emission zone. Inspection of individual channel maps and zeroth moment maps shows a variety of intensity distributions, depending on excitation effects, formation and depletion mechanisms, and the potential influence of a companion (see Sect. 5.4.2). In future work we will investigate different techniques such as fitting a modified power law (as in Sahai & Bieging 1993), an azimuthal average, or a cutoff such as $3 \times \sigma_{rms}$. These methods for determining the angular size are likely to strengthen the inference drawn from this analysis (see Sect. 5.4), because fewer transitions would be rejected owing to the lack of convergence of the Gaussian fitting method. We also will need to consider whether we are detecting essentially all the emission of each transition; or whether we are bounded by missing extended flux and/or sensitivity which varies between species. In general, the estimates of the maximum extent of any one transition might be biased if the CSE is not truly spherical, and depends on the orientation to the line of sight of any elongation.

Arguably, this is a simplified view of the wind kinematics since: (i) we only obtain a projected 1D view of the velocity vector field; and (ii) the spatial extents plotted in these figures might not always reflect the region where some of the extreme velocities arise from, for example in the situation where the extreme velocities are only reached at close distances from the AGB
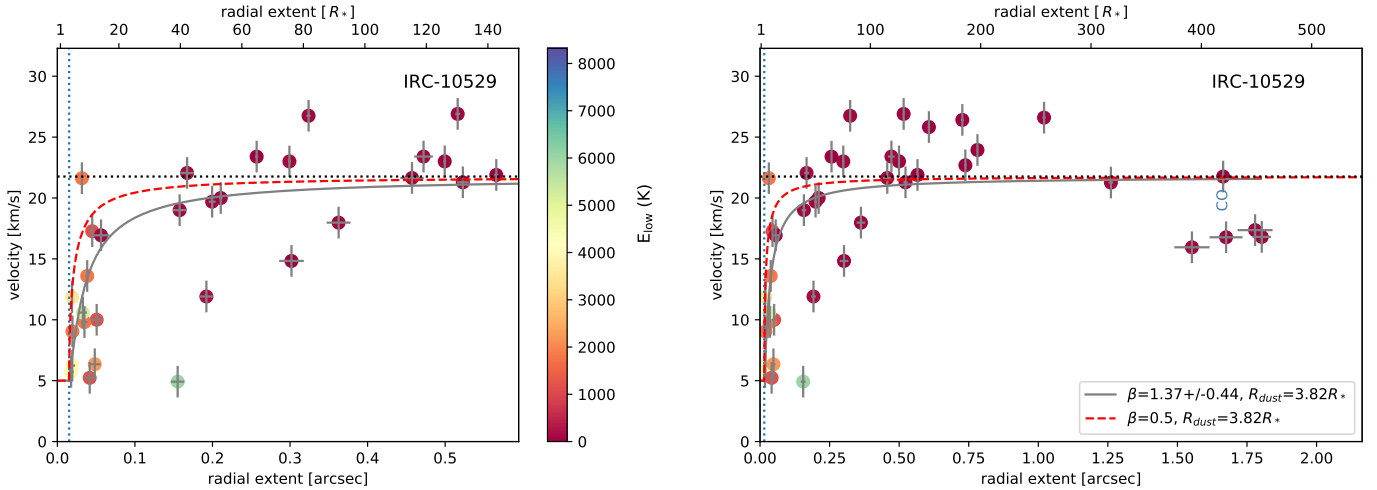
Fig. 11. Wind kinematics for IRC−10529. The wind velocities for all the molecular transitions observed in the low, medium, and high spatial resolution observations of IRC−10529 derived by the methodology described in Sect. 5.2. The velocities are plotted versus half of the spatial full-width-half-maximum (FWHM) of the molecular emission zone, and represent the dominant line formation region (Decin et al. 2018). The dotted blue vertical line indicates the radius at which the winds begin being accelerated (R_{dust} in Eq. (4); see Sect. 5.4), and the dotted black horizontal line is the velocity measure of the ^{12}CO $v = 0$ $J = 2 − 1$ line. Only emission zones which could be spatially deconvolved are plotted (as dots) – the colour of the symbols are related to the energy of the lower state as indicated by the colour code bar. The grey cross on top of each coloured dot indicates the error bar in the derived velocity and in the FWHM, and is often smaller than the size of the dots. The error bars represent the fitting margin. Not accounted for here are the uncertainties due to the Gaussian approximation which might result in a systematic underestimate of the angular extent (see Sect. 5.2). The bottom axis is in units of arcseconds and the top axis is in units of the stellar radius. *Left hand panel*: zooms into the 150 stellar radii of the circumstellar envelope, and *right hand panel*: full extent of the detected wind emission. The ^{12}CO $v = 0$ $J = 2 − 1$ transition (indicated in blue) only appears in the *right hand panel* owing to its large angular extent. The deconvolved data with a velocity less than that of the ^{12}CO $J = 2 − 1$ transition, were fitted with a β-velocity law (Eq. (4)). Indicated in the legend in the *right hand panel* is β. The fit is represented by the full grey line which can be compared with a β-velocity law for $\beta = 0.5$ indicated by the red dashed line.
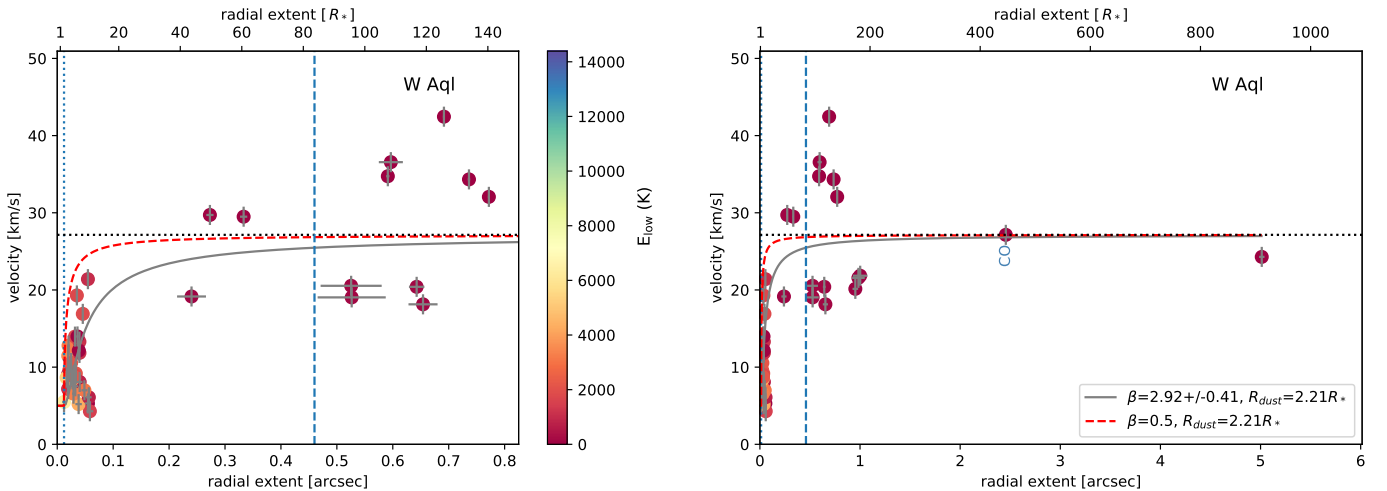
Fig. 12. Wind kinematics for W Aql. See Fig. 11 caption. The vertical blue dashed line at 0.″46 indicates the projected separation of the binary companion as deduced by Ramstedt et al. (2011).

star while the bulk of the emission further out has lower velocities. Nevertheless, interesting conclusions can already be derived from these results (see Sect. 5.4).

5.3. Combining different angular resolution data and the issue of resolved-out flux

To date, there are two stars for which the three individual spatial resolution data and the combined dataset have been analysed in detail – π^1 Gru (Homan et al. 2020) and R Hya (Homan et al. 2021) – thereby offering an opportunity to study the effect of resolved-out flux at a maximum recoverable scale for the lowest

resolution ALMA ATOMIUM observations of ∼10″. Resolving out flux might be an issue for the measurement of the angular extent of the molecular emission, but this does not hinder the determination of the velocity measure, because resolving out flux mainly reduces the measured line flux of extended emission around the central velocities and not that of the line wings which represent the more compact front and back caps of the circumstellar envelope.

The combined data are significantly more sensitive to emission which has structure on sub-arcsec scales, than the individual configurations. For an angular resolution of between ∼0.1 and ∼8 arcsec, the combined data sets contain at least twice as

much data as an individual configuration. The combined visibility data can be weighted as a function of baseline length to provide greater sensitivity for any desired resolution in this range, and this will be done in the detailed studies of each star. On smaller scales of tens of mas, the combined data set may also give a better image in the presence of extended structure although 'clean' stability can then be an issue. The combined data therefore allows for a more accurate measure of the total extent of emission from some lines at intermediate distances from the star.

The three observing dates of the low, medium, and high spatial resolution data differ by up to ∼9 months, while AGB stars have typical pulsation periods of ∼0.5–2 yr (see Table 1; Cernicharo et al. 2014; Fonfría et al. 2018). Therefore, the higher-excitation molecular transitions which are excited close to the stellar surface, can vary between epochs, and while this may lead to a more complete picture in the combined data, extreme variability (e.g., SiO masers) causes artefacts that result in combined images which might not be reliable. For these lines, the velocity measurement is more accurate for the merged dataset (see Step 6 in Sect. 5.2) than for the combined dataset.

For some molecular transitions the Levenberg–Marquardt minimization used for fitting the 2D Gaussian profiles failed for the combined dataset, but was successful for (one of) the individual observations. An example is the ^{12}CO $J = 2 - 1$ line where the emission zone in low spatial resolution data often better resembles a 2D Gaussian profile, but in the combined dataset the individual substructures are more prominent and a 2D Gaussian profile does not reproduce the observed emission. In general, an excellent correspondence is found for those molecular transitions that could be deconvolved in both the merged outcomes (of the low, medium, and high spatial resolution data; see Step 6 in Sect. 5.2) and the combined dataset. The differences between extents measured in the two ways have a dispersion of 0″.06.

Given these outcomes for π^1 Gru, we have used the merged results from the datasets of individual spatial resolution for the study of the kinematics in all the ATOMIUM AGB and RSG envelopes.

The only question still remaining is whether some flux is resolved out beyond the ∼10″ scale. The two molecules most affected by resolved-out flux are CO and SiO, owing to their high abundance in these oxygen-rich sources, and hence potentially extended molecular envelopes. For each target, we have estimated the CO and SiO photodissocation region using the formula given by Mamon et al. (1988) and González Delgado et al. (2003), respectively (see Sect. 3.1). For all the ATOMIUM sources, the SiO emission zone – as estimated from the photodissociation radius following González Delgado et al. (2003) – is less than ∼3″.5, with the exception of GY Aql where owing to its proximity to Earth the estimated SiO emission zone is ∼9″. Hence, resolving out flux should not be an issue for the SiO measurements. However, the CO emission zone for the ATOMIUM sources ranges between ∼20–300″, although the CO $J = 2 - 1$ transition is not excited up to the very outer boundary. This implies that the measured sizes of the ^{12}CO and ^{13}CO $J = 2 - 1$ transitions will be lower limits. This, however, does not hinder our present study on the wind kinematics, since we focus here on the wind initiation efficiency in the inner wind region, the maximum and minimum velocities deduced from the ATOMIUM data, and the imprint of a binary companion on the observationally derived wind velocity profiles. For all sources, additional observations of the ^{12}CO $J = 2 - 1$ and ^{13}CO $J = 2 - 1$ transitions have been or will be acquired with the APEX 12 m single

antenna, allowing us to constrain the CO emission region with higher precision.

5.4. Interpretation

In this section, we aim for an interpretation of the observationally derived wind kinematic profiles displayed in Figs. 11, 12, and C.1–C.15. We first examine the wind acceleration in the ATOMIUM sources. As will be discussed, the majority of the ATOMIUM sources display a slow wind acceleration characterised by quite high values of β. However, the wind kinematic profiles also make it readily clear that the radial velocity description as provided by the momentum equation (Eq. (2)) or the β-velocity law (Eq. (4)) for single-star models cannot capture the complexity of the velocity field in the ATOMIUM sources. We therefore extend this discussion with a more detailed examination of some of the observationally derived velocity profiles in the context of binary-star models.

5.4.1. Single-star models: wind initiation and terminal wind velocities

The first theoretical studies discussing analytical approximations (Gehrz & Woolf 1971; Gilman 1972) and numerical solutions of the equation of motion (Kwok 1975; Goldreich & Scoville 1976), resulted in gas velocity profiles having a characteristic sharp rise and reaching a constant 'terminal' wind velocity, v_∞, within the first few stellar radii (see also Fig. 8). Values for v_∞ have been observationally derived from the half-line width of low-excitation rotational CO lines (see, for example, Loup et al. 1993). The predicted fast acceleration of the wind velocity also motivated various modellers to assume a constant wind velocity (for example, Ramstedt et al. 2009; Sargent et al. 2011; Groenewegen 2014). However, the ATOMIUM data show that the notion of a constant wind velocity being reached within ∼$10 R_\star$ is not consistent with the observations. For all ATOMIUM sources, large variations in the derived velocity measures are seen, even at radial distances greater than $50 R_\star$, where (1D) spherical symmetric wind models with a steadily increasing velocity profile predict the velocity measure to have asymptotically reached the terminal wind velocity (see Fig. D.1).

In the approach adopted here we apply the same classical methodology in which a low excitation line of CO is used to determine the terminal wind velocity. However our approach differs from most earlier studies because: (1) it relies on a quantifiable metric linked to the 3σ rms noise in spectra that were observed at very high angular resolution and sensitivity; and (2) it does not rely on subjective judgement derived from visual inspection of less sensitive observations, or by referring to a model.

Various sources such as S Pav show some substantial changes in the velocity amplitude in the innermost few stellar radii. This behaviour might be reminiscent of pulsation-induced shocks for which hydrodynamical simulations show that they can lead to time-variable velocity characteristics within the first ∼4 stellar radii and with amplitudes of around 5–10 km s^{-1} (Bladh et al. 2019; Hoai et al. 2020, see Fig. D.3). The strongest effect is within the first $2 R_\star$, but rapidly fades out at greater distances (Liljegren et al. 2018; Bladh et al. 2019). While the shock in the 3D hydrodynamical models is global in scale, the maximum velocity reached by the gas in the shock front is not uniform but rather clumpy. The medium and low-resolution data are less sensitive to compact emission, and hence the high-resolution and combined datasets should be used to diagnose this

Table 3. Velocity parameters of the ATOMIUM sample.

(1) Target	(2) v_∞^{old}(CO) (km s^{-1})	(3) v_∞^{com}(CO) (km s^{-1})	(4) v(CO) (km s^{-1})	(5) v_{max} [a] (km s^{-1})	(6) Transition [b] (v_{max})	(7) v_{min} [a] (km s^{-1})	(8) Transition [b] (v_{min})	(9) R_{dust} ($R_\star$)	(10) β
S Pav	9.0 (1)	13.0	15.5	21.2	SiO $J = 5 - 4$	3.9	SO$_2$ $20_{2,18}-19_{3,17}$	2.0	0.7 ± 0.2
T Mic	6.1 (2)	12.7	16.0	21.8	SiO $J = 5 - 4$	4.0	CS $J = 5 - 4$	2.0	0.6 ± 0.3
U Del [c]	7.5 (1)	14.6	18.4	19.4	SiO $J = 6 - 5$	9.5	SiO $v = 1$ $J = 5 - 4$	5.1	–
RW Sco	11.0 (3)	18.5	18.5	18.8	SO$_2$ $11_{1,11}-10_{0,10}$	4.8	CS $J = 5 - 4$	6.7	9.1 ± 2.3
V PsA [c]	14.4 (1)	18.8	23.1	28.4	SiO $J = 6 - 5$	5.9	SiO $v = 4$ $J = 6 - 5$	3.5	–
SV Aqr [c]	7.9 (4)	15.9	17.0	23.8	SiO $J = 6 - 5$	4.9	Si^{34}S $J = 14 - 13$	5.2	–
R Hya	12.5 (5)	22.2	22.2	24.8	SiO $J = 6 - 5$	3.9	SO$_2$ $44_{6,38}-43_{7,37}$	2.0	0.6 ± 0.1
U Her	11.5 (6)	19.7	19.7	23.0	SiO $v = 1$ $J = 5 - 4$	4.4	SO$_2$ $4_{3,1} - 4_{2,2}$	2.6	2.0 ± 0.5
π^1 Gru	30.0 (7)	64.5	64.5	64.5	CO $J = 2 - 1$	3.9	SiO $v = 3$ $J = 6 - 5$	2.0	2.6 ± 0.6
AH Sco [d]	23.0 (8)	–	35.4	52.0	HCN $J = 3 - 2$	5.8	TiO $v = 1$ $\Omega = 1$ $J = 7 - 6$	3.8	5.0 ± 0.9
R Aql	9.5 (6)	12.8	15.8	21.4	SiO $J = 5 - 4$	4.3	SO$_2$ $v_2 = 1$ $30_{4,26}-30_{3,27}$	2.3	1.0 ± 0.3
W Aql	20.0 (5)	24.6	27.1	42.5	SiO $J = 6 - 5$	4.0	Si^{34}S $v = 1$ $J = 14 - 13$	2.2	2.9 ± 0.4
GY Aql	16.2 (9)	15.0	18.1	22.9	SiO $J = 5 - 4$	4.6	^{13}CS $J = 5 - 4$	3.1	3.2 ± 1.1
IRC -10529	16.5 (5)	21.8	21.8	26.9	SiS $J = 12 - 11$	4.3	CO $v = 1$ $J = 2 - 1$	3.8	1.4 ± 0.4
KW Sgr [c],[d]	27.0 (10)	–	27.7	34.0	SiO $J = 5 - 4$	3.9	^{29}Si^{34}S $J = 13 - 12$	7.9	–
IRC $+10011$	19.8 (5)	23.1	23.1	34.9	Si^{34}S $J = 14 - 13$	4.1	PO $^2\Pi_{1/2}$ $J, F{=}5.5, 6{-}4.5, 5$	6.5	2.8 ± 0.6
VX Sgr	24.3 (5)	32.9	34.4	66.5	HCN $J = 3 - 2$	4.0	^{34}SO$_2$ $24_{2,22}-24_{1,23}$	3.9	2.2 ± 0.5

Notes. The target name is in Col. (1); the terminal wind velocity v_∞^{old}(CO) in Col. (2) was obtained from observations of CO listed in the references indicated in parentheses; the wind velocity v_∞^{com}(CO) determined from the compact ATOMIUM ^{12}CO $v = 0$ $J = 2 - 1$ observation is in Col. (3); the velocity v(CO) determined from all ATOMIUM configurations of the ^{12}CO $v = 0$ $J = 2 - 1$ transition is in Col. (4), following Step 2 in Sect. 5.2; the maximum velocity v_{max} derived from the ATOMIUM observations is in Col. (5) with the corresponding molecular transition in Col. (6); the minimum velocity v_{min} derived from the ATOMIUM observations is in Col. (7) with the corresponding molecular transition in Col. (8); the two parameters derived from fitting the β-velocity law (Eq. (4)) are in Cols. (9) and (10) (see text for more details). [a]Includes both deconvolved and non-deconvolved data obtained after Step 3 as described in Sect. 5.2. [b]All rotational transitions are in the ground ($v = 0$) vibrational state unless otherwise noted. [c]Not enough data are available to determine β. [d]Targets only observed at medium and high spatial resolution.
References. (1) Olofsson et al. (2002); (2) Kerschbaum & Olofsson (1999); (3) Groenewegen et al. (1999); (4) Kerschbaum & Olofsson (1998); (5) De Beck et al. (2010); (6) Young (1995); (7) Doan et al. (2017); (8) Josselin et al. (1998); (9) Loup et al. (1993); (10) Mauron & Josselin (2011).

region that is disturbed by the shocks. Analogous to Khouri et al. (2016b, 2019), we derive a first estimate of the velocity amplitude in this complex region from the high-resolution observations of the highly excited OH and CO $v = 1$ transitions. These data indicate velocities of around $6 - 10$ km s^{-1}. For three source (R Aql, R Hya, and S Pav) the OH and CO $v = 1$ transition both have an inverse P-Cygni profile which – in the framework of a 1D single-star model – can be interpreted as a sign of infall of material with velocities of around 10–15 km s^{-1}. As discussed in Appendix D for the case of the 'normal shock' model, these shock characteristics cannot be traced in the medium and low-resolution data in the theoretical simulations of the ^{12}CO $v = 0$ $J = 2 - 1$ and ^{28}SiO $v = 0$ $J = 5 - 4$ line, and this is a conclusion which we extrapolate to the other molecular lines.

To compare our results here with the prior literature, we use the velocity retrieved from the ALMA CO $v = 0$ $J = 2 - 1$ line v(CO) to define the terminal wind velocity (v_∞), and thereby assume CO traces the velocity of the bulk material at large distances from the star. To avoid potential impact from pulsation-induced shocks (see above and Appendix D), we opt to use the (low-resolution) data from the compact configuration (v_∞^{com}(CO), see Col. 3 in Table 3).

As discussed in the Appendix D: (1) the effects of thermal and turbulent broadening in the wings of the line profile can be distinguished when CO is observed at high sensitivity; and (2) the low resolution CO data is indeed a good diagnostic for the terminal wind velocity. At a temperature of 2500 K, thermal broadening amounts to $\sim$1.2 km s^{-1}. The turbulent broadening is difficult to estimate, but the example of De Beck et al. (2012) indicates a value of around 1.5 km s^{-1}, so the combined effect

yields a Gaussian broadening of the line wings with HWHM of around 2.2 km s^{-1}. Excluding the fast, bipolar outflow traced in the ^{12}CO $J = 2$-1 data of π^1 Gru (see Sect. 5.4.2; Doan et al. 2017), the three red supergiants in the sample (AH Sco, KW Sgr, and VX Sgr) have the largest CO velocities. Even when we account for this broadening effect and for the spectral resolution of our ALMA data of $\sim$1.3 km s^{-1}, the results in Table 3 still indicate higher terminal velocities than were derived previously for most ATOMIUM sources. With the exception of GY Aql, the compact configuration ATOMIUM data of CO yield a larger terminal wind velocity than previous values (see cols. 2 and 3 in Table 3), where the maximum difference is a factor of 2.1. The reason for this difference is the higher sensitivity of the ATOMIUM data which allows us to trace the broad CO wings whose intensity is low.

In their survey of 42 mostly southern AGB stars that includes 21 M-type stars, Ramstedt et al. (2020) observed the $J = 2$-1 line of ^{12}CO in five of the ATOMIUM sources (T Mic, IRC–10529, IRC+10011, SV Aqr, and R Hya), but their observations were done with the ALMA 7 m Compact Array (ACA) – rather than with the ALMA 12 m Array which we used here. The synthesized beam of the ACA is about 5 arcsec and the 1σ rms of the data is about 40–110 mJy beam^{-1} in Band 6 (see Table B.1 in Ramstedt et al. 2020). When the ATOMIUM observations were made at low angular resolution in the compact configuration, the synthesized beam was about 7 times smaller (750 mas) and the 1σ rms (5 mJy beam^{-1}) was about 15 times smaller than in Ramstedt et al. The method for determining the CO velocity measure in Ramstedt et al. and ATOMIUM are similar: (1) the CO line profile is extracted for a circular aperture, which in

Ramstedt et al. consists of a fixed circular aperture of 18″ that is close to the maximum recoverable scale for these observations; and (2) the total velocity width (divided by a factor 2) is used to determine the CO velocity measure. Dividing the full width of the CO $J = 2$–1 line in Table B.1 of Ramstedt et al. by a factor of 2, the $v_{max}(CO)$ is 6.25 km s^{-1} for T Mic, 15.25 km s^{-1} for IRC-10529, 19.5 km s^{-1} for IRC+10011, 9.4 km s^{-1} for SV Aqr, and 10.5 km s^{-1} for R Hya. Comparing these with $v_\infty^{com}(CO)$ in Table 3, we find that $v_\infty^{com}(CO)$ determined in ATOMIUM is $1.5-2$ times higher in four stars and 1.2 times higher in IRC+10011 than in Ramstedt et al. (2020) As illustrated in Fig. A.4, the 15 times higher sensitivity in the ATOMIUM observation of T Mic yields a much more sensitive diagnostic of the low level emission from the wings of the CO line profile and an estimation of $v_{max}(CO)$.

Owing to resolved-out flux (see Sect. 5.3), in five out of the 17 sources a transition other than the ^{12}CO $J = 2 - 1$ line has the largest apparent emission zone. In W Aql and GY Aql, the ^{13}CO $J = 2 - 1$ line has a larger extent, while in IRC-10529 and IRC$+10011$ some transitions of SO$_2$ probe larger regions. KW Sgr is in various ways an exception, because we have not acquired the low-resolution data and the ^{12}CO $J = 2 - 1$ line remains undetected in the medium-resolution data – i.e., the data are sensitivity limited, owing to its large distance of 2 400 pc. Hence the CO extent plotted in Fig. C.12 is deduced from the high resolution data and some rotational transitions of SiO in the vibrational ground state which trace larger emission zones.

For all sources, except for π^1 Gru, the value of $v(CO)$ is, however, lower than the velocity measure from other transitions with spatial emission zones lower than the extent of CO (see Cols. 4–6 in Table 3), implying the wind profile will never be captured by the solution of the momentum equation (Eq. (2)) and cannot be adequately reproduced using a β-velocity law. Nevertheless, we have tried to quantify approximately the region of the wind initiation and the wind acceleration efficiency by fitting the β-velocity law (Eq. (4)) to the data in which the velocity measure is lower than the velocity determined from the ^{12}CO $J = 2 - 1$ line. The fits account for the variance on the measure of the velocity, and the emission extent. Equation (4) has three free parameters (v_0, R_{dust}, and β). The parameters v_0 and R_{dust} are not straightforward to quantify, because of the pulsation-induced shocks (see above). We therefore empirically estimate these two parameters[17].

To be a reliable measure of the velocity, the line profile should encompass at least three spectral resolution elements. Given the spectral resolution of ~1.3 km s^{-1}, this results in the minimum measurable velocity of around 4 km s^{-1} (as can be seen in Col. 7 of Table 3). Often the corresponding transitions are high-excitation transitions (see Col. 8 in Table 3), although in some cases the lowest velocity measure is derived for weak, low-excitation transitions with restricted signal-to-noise ratios. The parameter v_0 is determined as the minimum of the derived velocity measures (for both non-deconvolved and deconvolved emission; see Step 4 in Sect. 5.2), but should be larger than the local sound speed of $\sim 4-5$ km s^{-1}.

The parameter R_{dust} is then quantified as the radius at which v_0 is reached, but should be larger than $2 R_\star$. The derived values of R_{dust} vary between $2-6.7 R_\star$ (see Table 3). We caution against

over interpreting R_{dust} as the radius where the dust formation is starting, owing to the unknown effects of pulsation-induced shocks.

Using a Levenberg–Marquardt minimization routine, β is derived with its variance as given by the covariance matrix (see last two columns in Table 3) and – as can be seen in Table 3 – β varies between 0.6–9.1. In four sources (U Del, V PsA, SV Aqr, and KW Sgr) not enough data points with $v < v(CO)$ are available to determine β (see Figs. C.3–C.5, and C.12). For sources with $\dot{M} \gtrsim 5 \times 10^{-7} M_\odot$ yr^{-1} in which the spatial emission zone of a significant fraction of the molecular transitions could be deconvolved, we often see that the wind acceleration continues up to $\sim 100 R_\star$ and is represented by high values of β. Some examples include RW Sco, AH Sco and GY Aql.

The ATOMIUM data provides some insight into the wind initiation efficiency, particularly on the frequently observed low wind acceleration. But Figs. 11, 12, and C.1–C.15 confirm that the velocity vector field for all the ATOMIUM sources is more complex than is captured by current 1D hydrodynamical models. Pulsation-induced shocks can explain some of the velocity variation in the innermost few stellar radii, but as discussed in the next section this scenario cannot explain the complex kinematic behaviour seen in most ATOMIUM sources.

5.4.2. ATOMIUM wind profiles interpreted within the context of binary-star models

Two conclusions can be drawn from the plots of the wind kinematics: (1) the velocity measures in Table 4 which were derived from different rotational transitions and from different molecules at the same distance from the star (see Cols. 6 and 8 in Table 3), differ by more than the 3σ of the velocity resolution; and (2) the differences in the velocity measures correspond to real anomalies in the behaviour of the species. The wind kinematic plots also show that the SiO velocities are greater than than those of CO in 15 of the 17 ATOMIUM sources (i.e., all sources except π^1 Gru and RW Sco) by up to a factor ~1.6, and in six sources the velocity measure derived from other molecular lines are also greater than that of CO (see Tables 3–4). However, CO has a larger extent than SiO for all sources except KW Sgr (see Fig. D.2, and Sect. 5.4.1). In general, the CO emission is expected to extend roughly an order of magnitude farther than the SiO emission (see Sect. 5.3). The low-excitation CO line is predominantly collisionally excited, and is a reliable tracer of the density in the outer wind region. The Einstein A coefficients of the rotational lines of SiO in the ground-vibrational state are three orders of magnitude higher than those of CO, and as a result the rotational lines of SiO are sensitive to radiative (de-)excitation effects implying that these lines are key diagnostics for tracing the complex kinematics in the inner wind regions.

Given our current physical understanding, pulsation-induced shocks are not a viable mechanism to explain the wind kinematic profiles of most of the ATOMIUM sources, in particular for the case where larger SiO velocities are traced in the compact and medium configuration data (see the Appendix D). Hence other mechanisms should be considered. An obvious candidate is binary interaction – see our results published in Decin et al. (2020). Simulations for binary systems with a mass-losing AGB star as primary indicate that circumbinary disks are dynamically formed for systems with orbital separation $\lesssim 6$ au and mass-ratios in the order of 0.5–1 (Chen et al. 2017). A Keplerian (or in general rotational) velocity field (see dotted blue line in Fig. 8) can lead to velocities projected along the line-of-sight in excess of the terminal velocity in the innermost few stellar radii; see for

---

[17] The acceleration of the gas and dust begins at R_0, however – consistent with the prior work by Maercker et al.; Decin et al. (2016; 2018, and references therein) – we do not distinguish between R_{dust} and R_0 here, because the difference between R_{dust} and R_0 of $\lesssim 10 R_\star$ is small compared with the large scale description of the wind velocities that extend up to about $100 - 200 R_\star$ in many of the ATOMIUM stars.

Table 4. Velocity measures of SiO versus CO.

(1) $v(SiO) < v(CO)$	(2) $v(SiO) > v(CO)$ No other molecules with large v		(3) $v(SiO) > v(CO)$ Other molecules with large v	
Target	Target	Radial extent of SiO	Target	Radial extent of SiO
RW Sco	S Pav	$0\rlap{.}''20 - 21\,R_\star$	AH Sco	$0\rlap{.}''40 - 136\,R_\star$
π^1 Gru	T Mic	$0\rlap{.}''40 - 42\,R_\star$	W Aql	$0\rlap{.}''74 - 133\,R_\star$
	U Del	$0\rlap{.}''34 - 85\,R_\star$	GY Aql	$0\rlap{.}''82 - 149\,R_\star$
	V PsA	$0\rlap{.}''05 - 9\,R_\star$	IRC -10529	$0\rlap{.}''78 - 197\,R_\star$
	SV Aqr	$0\rlap{.}''52 - 263\,R_\star$	IRC $+10011$	$0\rlap{.}''67 - 336\,R_\star$
	R Hya	$0\rlap{.}''97 - 85\,R_\star$	VX Sgr	$0\rlap{.}''67 - 153\,R_\star$
	U Her	$0\rlap{.}''54 - 98\,R_\star$		
	R Aql	$1\rlap{.}''48 - 248\,R_\star$		
	KW Sgr	$0\rlap{.}''06 - 29\,R_\star$		

Notes. Listed in the first column are the ATOMIUM sources in which the velocity of all transitions of SiO is lower than that of CO $v = 0$ $J = 2 - 1$, $v(SiO) < v(CO)$). The second and third column list the ATOMIUM sources in which at least one SiO transition has a larger line width than the CO $v = 0$ $J = 2 - 1$ line, $v(SiO) > v(CO)$. In the case where only SiO lines trace velocities larger than the CO $v = 0$ $J = 2 - 1$ line, the source is listed in the second column; if other molecules also trace a larger velocity, the source name is indicated in the last column. The largest radial extent probed by the high velocity lines of SiO in the 15 sources with $v(SiO) > v(CO)$ is listed in Cols. (2) and (3). The maximum extent can be probed by SiO lines other than the one listed in Table 3.

example the case of L_2 Pup (Kervella et al. 2016). However, such a disk cannot explain the high velocity indicated for most sources in the centre and right hand columns of Table 4, which show high velocity SiO emission extends by more than $\sim$30 $R_\star$ (in diameter). We propose here that the gravitational influence of the binary companion (residing at a wide separation) is the cause for the latter behaviour, in particular for those sources in the last column of Table 4 for which various molecules trace large velocities. For example, if there is a (binary-induced) density contrast between an equatorial density enhancement and a biconical outflow or lobes, the velocities in these directions might differ, and they might not always favour the lobes if a denser equatorial region is more efficiently dust driven. As the result, the density differential will favour different species in the kinematical plots which are at the same distance from the star, but which have different velocities.

Checking the low-, medium-, and high-resolution data of the high-velocity lines, it becomes clear that in most cases the highest velocity value is observed in the high resolution data. This points towards excess high velocity emission arising from the shocked inner wind region, often within $\sim$2–10 $R_\star$ (Cernicharo et al. 1997; Herpin et al. 1998; Vlemmings et al. 2017, see the Appendix D). For the binary hypothesis to hold in the situation of a separation above $\sim$10 stellar radii, we need to know if there is high velocity emission at other locations in the wind farther away from the central star, which we refer to here as the persistence test. We therefore check if high velocity emission (from molecules other than CO) can be detected in the low and medium resolution data. Because the lower resolution data were observed for a shorter time, they are less sensitive to compact emission. If the emission only arises from the innermost few stellar radii, no maximum radius or Gaussian fit can be determined from the lower resolution data following the procedure outlined in Sect. 5.2, and we then categorise the emission as non-persistent. The persistence test reaches two levels: level 1 applies to the sources in the second column of Table 4, in which only SiO transitions reach velocities above the one deduced from the CO $v = 0$ $J = 2 - 1$ line; level 2 applies to sources in the last column of Table 4, in which molecules other than SiO also reach velocities above CO. The persistence test fails for five sources (U Del, V PsA, U Her, R Aql, and

KW Sgr), but is successful for four sources at level 1 (S Pav, T Mic, SV Aqr, and R Hya), and six sources at level 2 (AH Sco, W Aql, GY Aql, IRC -10529, IRC $+10011$, and VX Sgr). Obviously, all targets in the last column of Table 4 pass, which is not unexpected given the argument that molecules other than SiO are also diagnostics for the binary hypothesis. Hence, for the ten sources that pass the persistence test at either level 1 or level 2, we investigated whether we could deduce an approximate orbital separation from the kinematic information in Figs. 11, 12, C.1, C.2, C.5, C.6, C.9, C.11, C.13 and C.14.

W Aql was first identified as a spectroscopic binary by Herbig (1965). Ramstedt et al. (2011) used *Hubble* Space Telescope (HST) data, with a spatial resolution of $0\rlap{.}''12$, to deduce the projected separation of $0\rlap{.}''46$ ($\sim$150 au or $\sim$85 $R_\star$). The inclination of the orbit is unknown, and therefore the orientation of both sources relative to each other could not be deduced from these data, although Danilovich et al. (2015b) finds that the F8-G0 companion, with mass around 1 $M_\odot$, cannot be in front of the AGB star.

We note that a close companion can increase the terminal wind velocity as compared to a single star model owing to the slingshot mechanism (Maes et al. 2021). Morever as illustrated in Fig. 10, the gravitational attraction by a binary companion can induce an increase in the velocity amplitude at radii smaller than the orbital separation, eventually leading to a wave-like velocity profile beyond the orbital separation. These predictions are roughly consistent with the velocity profile of W Aql derived from the ATOMIUM data in Fig. 12, in which around 80 $R_\star$ we see both an increase and a decrease of the velocity measures with respect to the beta law. However the observed pattern is not as sharp as in the theoretical simulation in Fig. 10 (see also Fig. A.1) because: (1) the observations correspond to projected velocities; and (2) the binary system in W Aql might be more complex than the simulations. Given this first-order agreement, we use the closest location beyond 10 $R_\star$ where the velocity gradient turns negative as a proxy for a tentative indication of the upper limit on the orbital separation for those sources that pass the persistence test. Admittedly, this is not deduced straightforwardly for all sources. For those cases in which there are only a few points to guide us in this exercise, we have opted to list the

extent of the molecule with the highest velocity measure (v_{max}) which for W Aql would yield $0\rlap{.}''69$ (or $125\,R_\star$). This difference between the first estimate of $\sim 80\,R_\star$ – as deduced from the negative gradient of the velocity pattern, and $\sim 125\,R_\star$ as retrieved from v_{max} – also marks the limitations of the method proposed here for estimating the orbital separation.

Two other ATOMIUM sources in addition to W Aql are confirmed binaries (R Hya and π^1Gru). The companion of R Hya is thought to have a very wide orbital separation of $21''$ (Mason et al. 2001) which is beyond the field of view of the ATOMIUM data. In R Hya there is also evidence of dramatic perturbations in the CSE within a few $100\,R_\star$ of the central star, possibly owing to a second companion (Homan et al. 2021). π^1Gru has a companion of spectral type G0V at a separation of $2\rlap{.}''7$ (~ 500 au, Feast 1953), but there is no signature of the known companion in the line or continuum data of ATOMIUM.

Following a similar approach as for W Aql in Fig. 12, we derived an orbital separation for IRC–10529 from the velocity profile in Fig. 11, and the orbital separations for the eight other stars that pass the persistence test from the velocity profiles in Appendix C of: $0.20''-0.30''$ for S Pav, T Mic, SV Aqr, GY Aql, and IRC+10011; and between $0.45''-1.00''$ for AH Sco, R Hya, and VX Sgr.

In π^1Gru, the width of the ^{12}CO $J = 2 - 1$ line is more than a factor of 2 larger than that of any other molecular transition. The large line width – which had also been seen in previous ALMA ^{12}CO $J = 3 - 2$ data – was interpreted as an indication that the envelope structure of π^1 Gru includes a radially expanding equatorial torus (with a velocity of 8–13 km s^{-1}); and a fast bipolar outflow (with a linear velocity increase from 14 km s^{-1} at the base up to 100 km s^{-1} at the tip), with an angle between the line of sight and the equatorial plane of $40°$ (Doan et al. 2017). However, a spiral pattern has emerged in more recent higher spatial resolution ALMA ^{12}CO $J = 3 - 2$ data, and the spiral-arm separation hints towards the presence of a companion with a separation of less than 70 AU (or $34\,R_\star$; Doan et al. 2020). The ATOMIUM data will now further refine this picture, since various other molecules have line wings up to ~ 40 km s^{-1} and exhibit clear signs of rotation or bipolarity in their moment 1 maps – see for example the SiO $J = 5 - 4$ and $J = 6 - 5$ lines in Homan et al. (2020). The separation between the arc-like structures observed in the ATOMIUM ^{12}CO $J = 2 - 1$ channel maps (Decin et al. 2020), indicates the presence of a second companion with an orbital separation of around $0\rlap{.}''04$; and the dynamics traced by the SiO masers, suggest a (tentative) upper limit of the companion mass of $\sim 1.1\,M_\odot$ (Homan et al. 2020, Montargès et al., in prep.).

5.5. Discussion and implications

Putting these results in the context of the overall goals of the ATOMIUM project, it is clear that important science questions posed in Sect. 2.1.1 can be addressed by the ATOMIUM data. The wind acceleration efficiency, as expressed by the quite large values of β, seems quite low in general. The slow wind acceleration in turn yields constraints on the composition, size, and formation radius of dust grains, expressed for a single-star model by the dust extinction efficiency $Q_\lambda(a, r)$ in Eqs. (2) and (3). In addition, the question of the enforced wind dynamics in the intermediate wind region needs to be reformulated and should incorporate a search for the impact of binary companions on the wind dynamics of AGB and RSG stars.

Within both a single-star and a binary-star context, the results derived here have an impact on our understanding of the mass-loss rate for the following two reasons:

(i) When comparing prior results to those obtained in the ATOMIUM project, the velocities v(CO) derived from the low excitation line of ^{12}CO $J = 2 - 1$ are systematically higher when derived from the ATOMIUM data. Since v(CO) is often used as a measure for the terminal wind velocity in single-star models, a direct implication is that the mass-loss rate for these sources will be underestimated. The high sensitivity of the current ALMA data was the key for deriving these higher wind velocities. As noted in Sect. 5.4.1, under the condition of single star models the larger CO velocities might imply larger terminal velocities and larger values of $\dot{M}$, because the random scatter from the thermal line broadening and turbulence cannot explain these large velocities. As a result, we surmise that the terminal wind velocities and hence gas mass-loss rates will be underestimated for other AGB and RSG sources as well.

It might also be the case that the higher CO velocities (and those of other molecules) indicate exceptional motions owing to binary interaction. Under the condition of binary companions, the larger CO velocities might not be an indication of larger terminal velocities of the bulk material, but we are currently unable to estimate the relative effect in the single versus binary model, because assessing the impact of the companion on the Lagrangian (see Gregory 2006) would require extensive hydrodynamical simulations.

(ii) The current results support the conclusion in Decin et al. (2020) that (sub-)stellar binary interaction is the prime wind shaping agent of the majority of AGB/RSG stars, including the ATOMIUM sources whose mass-loss rates exceed the nuclear burning rate of around $1 \times 10^{-7}\,M_\odot$ yr^{-1}. In the majority of the ATOMIUM sources, molecular transitions other than the ^{12}CO $v = 0$ $J = 2 - 1$ line trace a larger velocity amplitude than CO, and have a spatial emission zone that is often greater than 30 stellar radii, but is much less than the extent of CO. This result has a two-fold repercussion on our historical insight of mass-loss rates in AGB and RSG which were derived within the context of single-star models:

– For close binary systems, a massive planet or stellar companion can enhance the AGB/RSG mass-loss rate by depositing angular momentum into the envelope and by reducing the effective gravity of the mass-losing star. Single stars or binary stars isolated from angular momentum deposition hence might suffer from a lower mass-loss rate during the AGB/RSG phase than stars prone to angular momentum deposition (Sabach & Soker 2018). Hydro-chemical simulations stimulated by the results of the ATOMIUM survey, indicate this difference might be up to almost an order of magnitude (Bolte et al., in prep., Decin 2021).

– There are profound implications for the classical measures of the AGB/RSG mass-loss rate derived under the assumption of a single star with a spherical wind. For a mass-losing AGB/RSG star in a binary system, the material flow will have a directional preference towards the orbital plane; and spiral arcs, circumbinary and accretion disks, etc. can be created (see, for example Mastrodemos & Morris 1999; Mohamed & Podsiadlowski 2012; Kim & Taam 2012; Liu et al. 2017; Chen et al. 2017; Saladino et al. 2019; El Mellah et al. 2020). As such, previous mass-loss rate estimates based on the assumption of spherical symmetry should be interpreted with care since systematic errors might occur, as shown recently by Homan et al. (2015, 2016), and Decin et al. (2019). We conjecture that in general, mass-loss rates hitherto derived from dust spectral features will be systematically overestimated. This conjecture is based on the fact that the companion's gravitational attraction can

create an equatorial density enhancement (EDE) with a density contrast that can be up to an order of magnitude higher than the background wind density (El Mellah et al. 2020). The spectral energy distribution (SED) in the near- and mid-infrared mainly traces warm dust residing close to the star, hence in the EDE. Therefore, depending on the inclination of the EDE, the analysis of dust spectral features using a simplified 1D approach reflects the higher density in the EDE created by the binary interaction, but not the actual mass-loss rate which will be lower. This conjecture is in line with previous observations which indicated that mass-loss rates derived from dust features are about an order of magnitude larger than mass-loss rates from CO observations (e.g., Heske et al. 1990).

These implications have a profound impact on several aspects of stellar evolution. Because the mass is the prime parameter determining the evolution and lifetime of a star, any modification to the stellar mass-loss over time has large repercussions on its evolutionary path.

If we would only account for (i), then a higher mass-loss rate implies a shortening of the AGB (RSG) phase. However, recent studies indicate that most stars in the universe will have one or more stellar or gas-giant planetary mass companions (Moe & Di Stefano 2017; Nielsen et al. 2019; Fulton & Petigura 2018; Fulton et al. 2019). Hence, most empirically derived mass-loss rates are from samples containing a large fraction of stars that experience binary interaction with a (sub-)stellar companion. As such, our knowledge of the mass-loss rate will be biased by the impact that companions can have both on the magnitude of the mass-loss and on the observed diagnostics from which mass-loss rates are retrieved. Given (ii) implies that the mass-loss rate for these cool evolved stars can be seriously overestimated in current stellar evolution models for single stars. These models use mass-loss rate prescriptions to calculate the change of mass during the AGB and RSG phase, whose parametric relations for the mass-loss rate are often based on fitting infrared colours or the dusty SEDs (Reimers 1975; de Jager et al. 1988; van Loon et al. 1999, 2005). The impact of the effects discussed in (ii) are somewhat countered by the increase in mass-loss rate prescribed by (i), but the amplitude of the effect discussed in (i) is lower than those in (ii). The white-dwarf initial-final mass function (see for example Cummings et al. 2018) limits the total mass-loss occurring during the AGB phase. Hence, this result implies that the AGB phase will be longer for single stars. For single stars with initial mass greater than ∼8 $M_\odot$, the mass before exploding as supernovae will be higher implying a larger fraction of more massive neutron stars can form. In addition, this implies that the contribution of cool evolved stars to the (extra)galactic dust budget will be lower than currently stipulated (see for example Matsuura et al. 2009, 2013), and the issue of the 'missing dust-mass problem[18]' is far from solved (Matsuura et al. 2009)

Dust-to-gas mass ratios for M-type AGB stars retrieved empirically are on average 5.8×10^{-3}, while for carbon and S-type AGB stars they are around 2.5×10^{-3} and 2.8×10^{-3}, respectively (Groenewegen & de Jong 1998; Groenewegen et al. 1999; Ramstedt et al. 2008, 2009; Danilovich et al. 2015a). Combining (i) and (ii) implies the dust-to-gas mass ratio for these samples, with derived gas mass-loss rates $\lesssim 1 \times 10^{-5}$ $M_\odot$ yr^{-1} for the carbon and S-type AGB stars and $\lesssim 7 \times 10^{-5}$ $M_\odot$ yr^{-1} for the M-type AGB

stars, will be lower than current empirically derived values indicate. This conclusion impacts all studies that are (or have been) using a dust-to-gas mass ratio to compute total mass-loss rates from retrieved dust masses for which most often the canonical dust-to-gas ratio of 1/200 (as derived from galactic ISM studies) is used (see for example Matsuura et al. 2009, 2013).

References

Adam, C., & Ohnaka, K. 2019, A&A, 628, A132

Agúndez, M., Cernicharo, J., & Guélin, M. 2010, ApJ, 724, L133

Agúndez, M., Cernicharo, J., Quintana-Lacaci, G., et al. 2017, A&A, 601, A4

Agúndez, M., Martínez, J. I., de Andres, P. L., Cernicharo, J., & Martín-Gago, J. A. 2020, A&A, 637, A59

Alma, P., Fomalont, E. B., Vlahakis, C., et al. 2015, ApJ, 808, L1

Andronov, I. L., & Chinarova, L. L. 2012, Odessa Astron. Publ., 25, 148

Arroyo-Torres, B., Wittkowski, M., Marcaide, J. M., & Hauschildt, P. H. 2013, A&A, 554, A76

Bailer-Jones, C. A. L., Rybizki, J., Fouesneau, M., Demleitner, M., & Andrae, R. 2021, AJ, 161, 147

Bennett, P. D. 2010, ASP Conf. Ser., 425, 181

Bertschinger, E., & Chevalier, R. A. 1985, ApJ, 299, 167

Bladh, S., & Höfner, S. 2012, A&A, 546, A76

Bladh, S., Liljegren, S., Höfner, S., Aringer, B., & Marigo, P. 2019, A&A, 626, A100

---

[18] The missing dust-mass problem refers to the Large Magellanic Cloud and other high-z galaxies whose accumulated dust mass from AGB and RSG stars (and possibly supernovae) over the dust lifetime is significantly less than the dust mass in the ISM.

Boulangier, J., Gobrecht, D., Decin, L., de Koter, A., & Yates, J. 2019, MNRAS, 489, 4890

Bowen, G. H. 1988, ApJ, 329, 299

Bromley, S. T., Gómez Martín, J. C., & Plane, J. M. C. 2016, Phys. Chem. Chem. Phys. (Incorporating Faraday Trans.), 18, 26913

Bujarrabal, V., Fuente, A., & Omont, A. 1994, A&A, 285, 247

Bujarrabal, V., Alcolea, J., Mikołajewska, J., Castro-Carrizo, A., & Ramstedt, S. 2018, A&A, 616, L3

Castro-Carrizo, A., Quintana-Lacaci, G., Neri, R., et al. 2010, A&A, 523, A59

Cernicharo, J., Alcolea, J., Baudry, A., & Gonzalez-Alfonso, E. 1997, A&A, 319, 607

Cernicharo, J., Teyssier, D., Quintana-Lacaci, G., et al. 2014, ApJ, 796, L21

Cernicharo, J., Marcelino, N., Agúndez, M., & Guélin, M. 2015, A&A, 575, A91

Chapman, J. M., & Cohen, R. J. 1986, MNRAS, 220, 513

Chen, X., & Shen, Z. Q. 2008, in The Art of Modeling Stars in the 21st Century, eds. L. Deng, & K. L. Chan, 247

Chen, X., Shen, Z.-Q., & Xu, Y. 2007, Chin. J. Astron. Astrofis., 7, 531

Chen, Z., Frank, A., Blackman, E. G., Nordhaus, J., & Carroll-Nellenback, J. 2017, MNRAS, 468, 4465

Cherchneff, I. 2006, A&A, 456, 1001

Cherchneff, I. 2011, A&A, 526, L11

Chiavassa, A., Lacour, S., Millour, F., et al. 2010, A&A, 511, A51

Condon, J. J. 1997, PASP, 109, 166

Cummings, J. D., Kalirai, J. S., Tremblay, P. E., Ramirez-Ruiz, E., & Choi, J. 2018, ApJ, 866, 21

Danilovich, T., Bergman, P., Justtanont, K., et al. 2014, A&A, 569, A76

Danilovich, T., Teyssier, D., Justtanont, K., et al. 2015a, A&A, 581, A60

Danilovich, T., Olofsson, G., Black, J. H., Justtanont, K., & Olofsson, H. 2015b, A&A, 574, A23

Danilovich, T., De Beck, E., Black, J. H., Olofsson, H., & Justtanont, K. 2016, A&A, 588, A119

Danilovich, T., Van de Sande, M., De Beck, E., et al. 2017, A&A, 606, A124

Danilovich, T., Gottlieb, C. A., Decin, L., et al. 2020a, ApJ, 904, 110

Danilovich, T., Richards, A. M. S., Decin, L., Van de Sande, M., & Gottlieb, C. A. 2020b, MNRAS, 494, 1323

Danilovich, T., Van de Sande, M., Plane, J. M. C., et al. 2021, A&A, 655, A80

De Beck, E., Decin, L., de Koter, A., et al. 2010, A&A, 523, A18

De Beck, E., Lombaert, R., Agúndez, M., et al. 2012, A&A, 539, A108

De Ceuster, F., Homan, W., Yates, J., et al. 2020a, MNRAS, 492, 1812

De Ceuster, F., Bolte, J., Homan, W., et al. 2020b, MNRAS, 499, 5194

Decin, L. 2021, ARA&A, 59, 337

Decin, L., Hony, S., de Koter, A., et al. 2006, A&A, 456, 549

Decin, L., Cherchneff, I., Hony, S., et al. 2008, A&A, 480, 431

Decin, L., Justtanont, K., De Beck, E., et al. 2010a, A&A, 521, L4

Decin, L., De Beck, E., Brünken, S., et al. 2010b, A&A, 516, A69

Decin, L., Richards, A. M. S., Neufeld, D., et al. 2015, A&A, 574, A5

Decin, L., Richards, A. M. S., Millar, T. J., et al. 2016, A&A, 592, A76

Decin, L., Richards, A. M. S., Waters, L. B. F. M., et al. 2017, A&A, 608, A55

Decin, L., Richards, A. M. S., Danilovich, T., Homan, W., & Nuth, J. A. 2018, A&A, 615, A28

Decin, L., Homan, W., Danilovich, T., et al. 2019, Nat. Astron., 3, 408

Decin, L., Montargès, M., Richards, A. M. S., et al. 2020, Science, 369, 1497

Deguchi, S., & Goldsmith, P. F. 1985, Nature, 317, 336

Dehaes, S., Groenewegen, M. A. T., Decin, L., et al. 2007, MNRAS, 377, 931

de Jager, C., Nieuwenhuijzen, H., & van der Hucht, K. A. 1988, A&AS, 72, 259

Doan, L., Ramstedt, S., Vlemmings, W. H. T., et al. 2017, A&A, 605, A28

Doan, L., Ramstedt, S., Vlemmings, W. H. T., et al. 2020, A&A, 633, A13

El Mellah, I., Bolte, J., Decin, L., Homan, W., & Keppens, R. 2020, A&A, 637, A91

Endres, C. P., Schlemmer, S., Schilke, P., Stutzki, J., & Müller, H. S. P. 2016, J. Mol. Spectrosc., 327, 95

Ercolano, B., Morisset, C., Barlow, M. J., Storey, P. J., & Liu, X. W. 2003, MNRAS, 340, 1153

Escatllar, A. M., & Bromley, S. T. 2020, A&A, 634, A77

Feast, M. W. 1953, MNRAS, 113, 510

Fonfría, J. P., Cernicharo, J., Richter, M. J., & Lacy, J. H. 2008, ApJ, 673, 445

Fonfría, J. P., Fernández-López, M., Pardo, J. R., et al. 2018, ApJ, 860, 162

Ford, K. E. S., Neufeld, D. A., Goldsmith, P. F., & Melnick, G. J. 2003, ApJ, 589, 430

Ford, K. E. S., Neufeld, D. A., Schilke, P., & Melnick, G. J. 2004, ApJ, 614, 990

Fulton, B. J., & Petigura, E. A. 2018, AJ, 156, 264

Fulton, B., Rosenthal, L., Howard, A., Hirsch, L., & Isaacson, H. 2019, AAS/Division for Extreme Sol. Syst. Abstracts, 51, 401.01

Gaia Collaboration (Brown, A. G. A., et al.) 2018, A&A, 616, A1

Gail, H. P., & Sedlmayr, E. 2013, Physics and Chemistry of Circumstellar Dust Shells

Gehrz, R. D., & Woolf, N. J. 1971, ApJ, 165, 285

Gilman, R. C. 1972, ApJ, 178, 423

Gobrecht, D., Cherchneff, I., Sarangi, A., Plane, J. M. C., & Bromley, S. T. 2016, A&A, 585, A6

Gobrecht, D., Decin, L., Cristallo, S., & Bromley, S. T. 2018, Chem. Phys. Lett., 711, 138

Goldreich, P., & Scoville, N. 1976, ApJ, 205, 144

González Delgado, D., Olofsson, H., Kerschbaum, F., et al. 2003, A&A, 411, 123

Gregory, R. D. 2006, Classical Mechanics (Cambridge University Press)

Groenewegen, M. A. T. 2014, A&A, 561, L11

Groenewegen, M. A. T., & de Jong, T. 1998, A&A, 337, 797

Groenewegen, M. A. T., Baas, F., Blommaert, J. A. D. L., et al. 1999, A&AS, 140, 197

Guélin, M., Patel, N. A., Bremer, M., et al. 2018, A&A, 610, A4

Guerrero, M. A., Chu, Y.-H., Manchado, A., & Kwitter, K. B. 2003, AJ, 125, 3213

Gustafsson, B., & Höfner, S. 2003, Asymptotic Giant Branch Stars, 149

Gustafsson, B., & Plez, B. 1992, in Instabilities in Evolved Super- and Hypergiants, eds. C. de Jager, & H. Nieuwenhuijzen, 86

Habing, H. J. 1996, A&ARv, 7, 97

Habing, H. J., & Olofsson, H. 2004, Asymptotic Giant Branch Stars

Haubois, X., Norris, B., Tuthill, P. G., et al. 2019, A&A, 628, A101

Heras, A. M., & Hony, S. 2005, A&A, 439, 171

Herbig, G. H. 1965, Veroeffentlichungen der Remeis-Sternwarte zu Bamberg, 27, 164

Herpin, F., Baudry, A., Alcolea, J., & Cernicharo, J. 1998, A&A, 334, 1037

Heske, A., Forveille, T., Omont, A., van der Veen, W. E. C. J., & Habing, H. J. 1990, A&A, 239, 173

Hinkle, K. H., Hall, D. N. B., & Ridgway, S. T. 1982, ApJ, 252, 697

Hinkle, K. H., Lebzelter, T., & Scharlach, W. W. G. 1997, AJ, 114, 2686

Hoai, D. T., Tuan-Anh, P., Nhung, P. T., et al. 2020, MNRAS, 495, 943

Höfner, S. 2008, A&A, 491, L1

Höfner, S., & Olofsson, H. 2018, A&ARv, 26, 1

Homan, W., Decin, L., de Koter, A., et al. 2015, A&A, 579, A118

Homan, W., Boulangier, J., Decin, L., & de Koter, A. 2016, A&A, 596, A91

Homan, W., Richards, A., Decin, L., de Koter, A., & Kervella, P. 2018, A&A, 616, A34

Homan, W., Montargès, M., Pimpanuwat, B., et al. 2020, A&A, 644, A61

Homan, W., Pimpanuwat, B., Herpin, F., et al. 2021, A&A, 651, A82

Hoyle, F., & Wickramasinghe, N. C. 1962, MNRAS, 124, 417

Humphreys, E., Miura, R., Brogan, C. L., et al. 2016, Proceedings of the 2016 ALMA Conference, 1

Josselin, E., & Plez, B. 2007, A&A, 469, 671

Josselin, E., Loup, C., Omont, A., et al. 1998, A&AS, 129, 45

Justtanont, K., Feuchtgruber, H., de Jong, T., et al. 1998, A&A, 330, L17

Kamiński, T., Wong, K. T., Schmidt, M. R., et al. 2016, A&A, 592, A42

Kamiński, T., Müller, H. S. P., Schmidt, M. R., et al. 2017, A&A, 599, A59

Kerschbaum, F., & Olofsson, H. 1998, A&A, 336, 654

Kerschbaum, F., & Olofsson, H. 1999, A&AS, 138, 299

Kervella, P., Homan, W., Richards, A. M. S., et al. 2016, A&A, 596, A92

Kervella, P., Decin, L., Richards, A. M. S., et al. 2018, A&A, 609, A67

Khouri, T., de Koter, A., Decin, L., et al. 2014, A&A, 561, A5

Khouri, T., Maercker, M., Waters, L. B. F. M., et al. 2016a, A&A, 591, A70

Khouri, T., Vlemmings, W. H. T., Ramstedt, S., et al. 2016b, MNRAS, 463, L74

Khouri, T., Vlemmings, W. H. T., Olofsson, H., et al. 2018, A&A, 620, A75

Khouri, T., Velilla-Prieto, L., De Beck, E., et al. 2019, A&A, 623, L1

Khouri, T., Vlemmings, W. H. T., Paladini, C., et al. 2020, A&A, 635, A200

Kim, H., & Taam, R. E. 2012, ApJ, 759, 59

Kim, H., Liu, S.-Y., Hirano, N., et al. 2015, ApJ, 814, 61

Kiss, L. L., Szabó, G. M., & Bedding, T. R. 2006, MNRAS, 372, 1721

Kwok, S. 1975, ApJ, 198, 583

Lamers, H. J. G. L. M., & Cassinelli, J. P. 1999, Introduction to Stellar Winds

Li, X., Millar, T. J., Heays, A. N., et al. 2016, A&A, 588, A4

Liljegren, S., Höfner, S., Freytag, B., & Bladh, S. 2018, A&A, 619, A47

Lindqvist, M., Nyman, L. A., Olofsson, H., & Winnberg, A. 1988, A&A, 205, L15

Liu, Z.-W., Stancliffe, R. J., Abate, C., & Matrozis, E. 2017, ApJ, 846, 117

Loup, C., Forveille, T., Omont, A., & Paul, J. F. 1993, A&AS, 99, 291

Maercker, M., Mohamed, S., Vlemmings, W. H. T., et al. 2012, Nature, 490, 232

Maercker, M., Danilovich, T., Olofsson, H., et al. 2016, A&A, 591, A44

Maes, S. 2020, Master's Thesis, KU Leuven, Belgium

Maes, S., Homan, W., Malfait, J., et al. 2021, A&A, 653, A25

Mamon, G. A., Glassgold, A. E., & Huggins, P. J. 1988, ApJ, 328, 797

Marigo, P., Girardi, L., Bressan, A., et al. 2008, A&A, 482, 883

Mason, B. D., Wycoff, G. L., Hartkopf, W. I., Douglass, G. G., & Worley, C. E. 2001, AJ, 122, 3466

Mastrodemos, N., & Morris, M. 1999, ApJ, 523, 357

Matsuura, M., Barlow, M. J., Zijlstra, A. A., et al. 2009, MNRAS, 396, 918

Matsuura, M., Woods, P. M., & Owen, P. J. 2013, MNRAS, 429, 2527

Mauron, N., & Josselin, E. 2011, A&A, 526, A156
McCarthy, M. C., Gottlieb, C. A., & Cernicharo, J. 2019, J. Mol. Spectros., 356, 7
McDonald, I., & Trabucchi, M. 2019, MNRAS, 484, 4678
McDonald, I., & Zijlstra, A. A. 2016, ApJ, 823, L38
McElroy, D., Walsh, C., Markwick, A. J., et al. 2013, A&A, 550, A36
McMullin, J. P., Waters, B., Schiebel, D., Young, W., & Golap, K. 2007, ASP Conf. Ser., 376, 127
Melnick, G. J., Neufeld, D. A., Ford, K. E. S., Hollenbach, D. J., & Ashby, M. L. N. 2001, Nature, 412, 160
Moe, M., & Di Stefano, R. 2017, ApJS, 230, 15
Mohamed, S., & Podsiadlowski, P. 2012, Baltic Astron., 21, 88
Montargès, M., Homan, W., Keller, D., et al. 2019, MNRAS, 485, 2417
Morris, M., Lucas, R., & Omont, A. 1985, A&A, 142, 107
Müller, H. S. P., Thorwirth, S., Roth, D. A., & Winnewisser, G. 2001, A&A, 370, L49
Müller, H. S. P., Schlöder, F., Stutzki, J., & Winnewisser, G. 2005, J. Mol. Struct., 742, 215
Neri, R., Kahane, C., Lucas, R., Bujarrabal, V., & Loup, C. 1998, A&AS, 130, 1
Netzer, N., & Elitzur, M. 1993, ApJ, 410, 701
Neugebauer, G., & Leighton, R. B. 1969, Two-micron sky survey. A preliminary catalogue
Nielsen, E. L., De Rosa, R. J., Macintosh, B., et al. 2019, AJ, 158, 13
Norris, B. R., Tuthill, P. G., Ireland, M. J., et al. 2012, Nature, 484, 220
Nowotny, W., Höfner, S., & Aringer, B. 2010, A&A, 514, A35
Nyman, L. A., Booth, R. S., Carlstrom, U., et al. 1992, A&AS, 93, 121
Ohnaka, K., Weigelt, G., & Hofmann, K. H. 2016, A&A, 589, A91
Ohnaka, K., Weigelt, G., & Hofmann, K. H. 2017, A&A, 597, A20
Olofsson, H., González Delgado, D., Kerschbaum, F., & Schöier, F. L. 2002, A&A, 391, 1053
Paladini, C., Baron, F., Jorissen, A., et al. 2018, Nature, 553, 310
Paquette, J. A., Ferguson, F. T., & Nuth, J. A. 2011, ApJ, 732, 62
Perryman, M. A. C., Lindegren, L., Kovalevsky, J., et al. 1997, A&A, 500, 501
Pickett, H. M., Poynter, R. L., Cohen, E. A., et al. 1998, J. Quant. Spec. Radiat. Transf., 60, 883
Plane, J. M. C. 2013, Philos. Trans. R. Soc. London Ser. A, 371, 20120335
Ramstedt, S., Schöier, F. L., Olofsson, H., & Lundgren, A. A. 2008, A&A, 487, 645
Ramstedt, S., Schöier, F. L., & Olofsson, H. 2009, A&A, 499, 515
Ramstedt, S., Maercker, M., Olofsson, G., Olofsson, H., & Schöier, F. L. 2011, A&A, 531, A148
Ramstedt, S., Mohamed, S., Vlemmings, W. H. T., et al. 2014, A&A, 570, L14
Ramstedt, S., Mohamed, S., Vlemmings, W. H. T., et al. 2017, A&A, 605, A126
Ramstedt, S., Mohamed, S., Olander, T., et al. 2018, A&A, 616, A61
Ramstedt, S., Vlemmings, W. H. T., Doan, L., et al. 2020, A&A, 640, A133
Randall, S. K., Trejo, A., Humphreys, E. M. L., et al. 2020, A&A, 636, A123
Reid, M. J., & Menten, K. M. 1997, ApJ, 476, 327
Reimers, D. 1975, Memoires Soc. R. Sci. Liege, 8, 369
Richichi, A., Percheron, I., & Khristoforova, M. 2005, A&A, 431, 773
Russell, H. N. 1934, ApJ, 79, 317
Ryde, N., Eriksson, K., Gustafsson, B., Lindqvist, M., & Olofsson, H. 1998, Ap&SS, 255, 301
Sabach, E., & Soker, N. 2018, MNRAS, 479, 2249
Sahai, R., & Bieging, J. H. 1993, AJ, 105, 595
Saladino, M. I., Pols, O. R., & Abate, C. 2019, A&A, 626, A68
Samus, N. N., Kazarovets, E. V., Durlevich, O. V., Kireeva, N. N., & Pastukhova, E. N. 2017, Astron. Rep., 61, 80
Sargent, B. A., Srinivasan, S., & Meixner, M. 2011, ApJ, 728, 93
Schoenberg, K. 1988, A&A, 195, 198
Schöier, F. L., van der Tak, F. F. S., van Dishoeck, E. F., & Black, J. H. 2005, A&A, 432, 369
Schöier, F. L., Olofsson, H., & Lundgren, A. A. 2006, A&A, 454, 247
Schöier, F. L., Ramstedt, S., Olofsson, H., et al. 2013, A&A, 550, A78
Scicluna, P., Siebenmorgen, R., Wesson, R., et al. 2015, A&A, 584, L10
Shen, Z.-J., & Zhou, J.-F. 2008, Chin. J. Astron. Astrofis., 8, 343
Takigawa, A., Kamizuka, T., Tachibana, S., & Yamamura, I. 2017, Sci. Adv., 3, eaao2149
Taylor, G. B., Carilli, C. L., & Perley, R. A. 1999, Synthesis Imaging in Radio Astronomy II, 180
Thirumalai, A., & Heyl, J. S. 2012, MNRAS, 422, 1272
Tielens, A. G. G. M. 2005, The Physics and Chemistry of the Interstellar Medium
Tielens, A. G. G. M., Waters, L. B. F. M., Molster, F. J., & Justtanont, K. 1998, Ap&SS, 255, 415
Ueta, T., Murakawa, K., & Meixner, M. 2007, AJ, 133, 1345
Van de Sande, M., Decin, L., Lombaert, R., et al. 2018a, A&A, 609, A63
Van de Sande, M., Sundqvist, J. O., Millar, T. J., et al. 2018b, A&A, 616, A106
Van de Sande, M., Walsh, C., Mangan, T. P., & Decin, L. 2019, MNRAS, 490, 2023
van der Tak, F. F. S., Lique, F., Faure, A., Black, J. H., & van Dishoeck, E. F. 2020, Atoms, 8, 15
van Loon, J. T., Groenewegen, M. A. T., de Koter, A., et al. 1999, A&A, 351, 559
van Loon, J. T., Cioni, M.-R. L., Zijlstra, A. A., & Loup, C. 2005, A&A, 438, 273
Velilla Prieto, L., Cernicharo, J., Quintana-Lacaci, G., et al. 2015, ApJ, 805, L13
Verhoelst, T., van der Zypen, N., Hony, S., et al. 2009, A&A, 498, 127
Vlemmings, W. H. T., & van Langevelde, H. J. 2007, A&A, 472, 547
Vlemmings, W., Khouri, T., O'Gorman, E., et al. 2017, Nat. Astron., 1, 848
Vlemmings, W. H. T., Khouri, T., & Olofsson, H. 2019, A&A, 626, A81
Vogt, N., Contreras-Quijada, A., Fuentes-Morales, I., et al. 2016, ApJS, 227, 6
Waters, L. B. F. M. 2011, ASP Conf. Ser., 445, 227
West, N. A., Millar, T. J., Van de Sande, M., et al. 2019, ApJ, 885, 134
Wildt, R. 1933, Z. Astrophys., 6, 345
Willacy, K., & Millar, T. J. 1997, A&A, 324, 237
Wittkowski, M., Arroyo-Torres, B., Marcaide, J. M., et al. 2017, A&A, 597, A9
Woitke, P. 2006, A&A, 460, L9
Wong, K. T., Kamiński, T., Menten, K. M., & Wyrowski, F. 2016, A&A, 590, A127
Wood, P. R. 1990, ASP Conf. Ser., 11, 355
Wood, P. R. 2015, MNRAS, 448, 3829
Yang, B., Stancil, P. C., Balakrishnan, N., & Forrey, R. C. 2010, ApJ, 718, 1062
Young, K. 1995, ApJ, 445, 872
Zijlstra, A. A., Bedding, T. R., & Mattei, J. A. 2002, MNRAS, 334, 498

[1] Harvard-Smithsonian Center for Astrophysics, 60 Garden Street, Cambridge, MA 02138, USA
[2] Institute of Astronomy, KU Leuven, Celestijnenlaan 200D, 3001 Leuven, Belgium
e-mail: Leen.Decin@kuleuven.be
[3] University of Leeds, School of Chemistry, Leeds LS2 9JT, UK
[4] Jodrell Bank Centre for Astrophysics, Department of Physics and Astronomy, University of Manchester, Manchester M13 9PL, UK
[5] University College London, Department of Physics and Astronomy, London WC1E 6BT, UK
[6] Astrophysics Research Centre, School of Mathematics and Physics, Queen's University Belfast, University Road, Belfast BT7 1NN, UK
[7] LESIA, Observatoire de Paris, Université PSL, CNRS, Sorbonne Université, Université de Paris, 5 place Jules Janssen, 92195 Meudon, France
[8] Institut de Radioastronomie Millimétrique, 300 rue de la Piscine, 38406 Saint Martin d'Hères, France
[9] Open University, Walton Hall, Milton Keynes MK7 6AA, UK
[10] Université de Bordeaux, Laboratoire d'Astrophysique de Bordeaux, 33615 Pessac, France
[11] Chalmers University of Technology, Onsala Space Observatory, 43992 Onsala, Sweden
[12] University of Amsterdam, Anton Pannekoek Institute for Astronomy, 1090 GE Amsterdam, The Netherlands
[13] KU Leuven, Center for mathematical Plasma Astrophysics, 3001 Leuven, Belgium
[14] National Astronomical Research Institute of Thailand, Chiangmai 50180, Thailand
[15] Max-Planck-Institut für Radioastronomie, 53121 Bonn, Germany
[16] Laboratoire d'Etudes Spatiales et d'Instrumentation en Astrophysique, Observatoire de Paris, Université Paris Sciences et Lettres, Centre National de la Recherche Scientifique, Sorbonne Université, Université de Paris, 92195 Meudon, France
[17] Université Côte d'Azur, Laboratoire Lagrange, Observatoire de la Côte d'Azur, 06304 Nice Cedex 4, France
[18] Universität zu Köln, I. Physikalisches Institut, 50937 Köln, Germany
[19] California Institute of Technology, Jet Propulsion Laboratory, Pasadena, CA 91109, USA
[20] School of Physics and Astronomy, University of Leeds, Leeds LS2 9JT, UK
[21] SRON Netherlands Institute for Space Research, 3584 CA Utrecht, The Netherlands
[22] Radboud University, Institute for Mathematics, Astrophysics and Particle Physics (IMAPP), Nijmegen, The Netherlands
[23] University of Hong Kong, Laboratory for Space Research, Pokfulam, Hong Kong

Appendix A: Additional figures
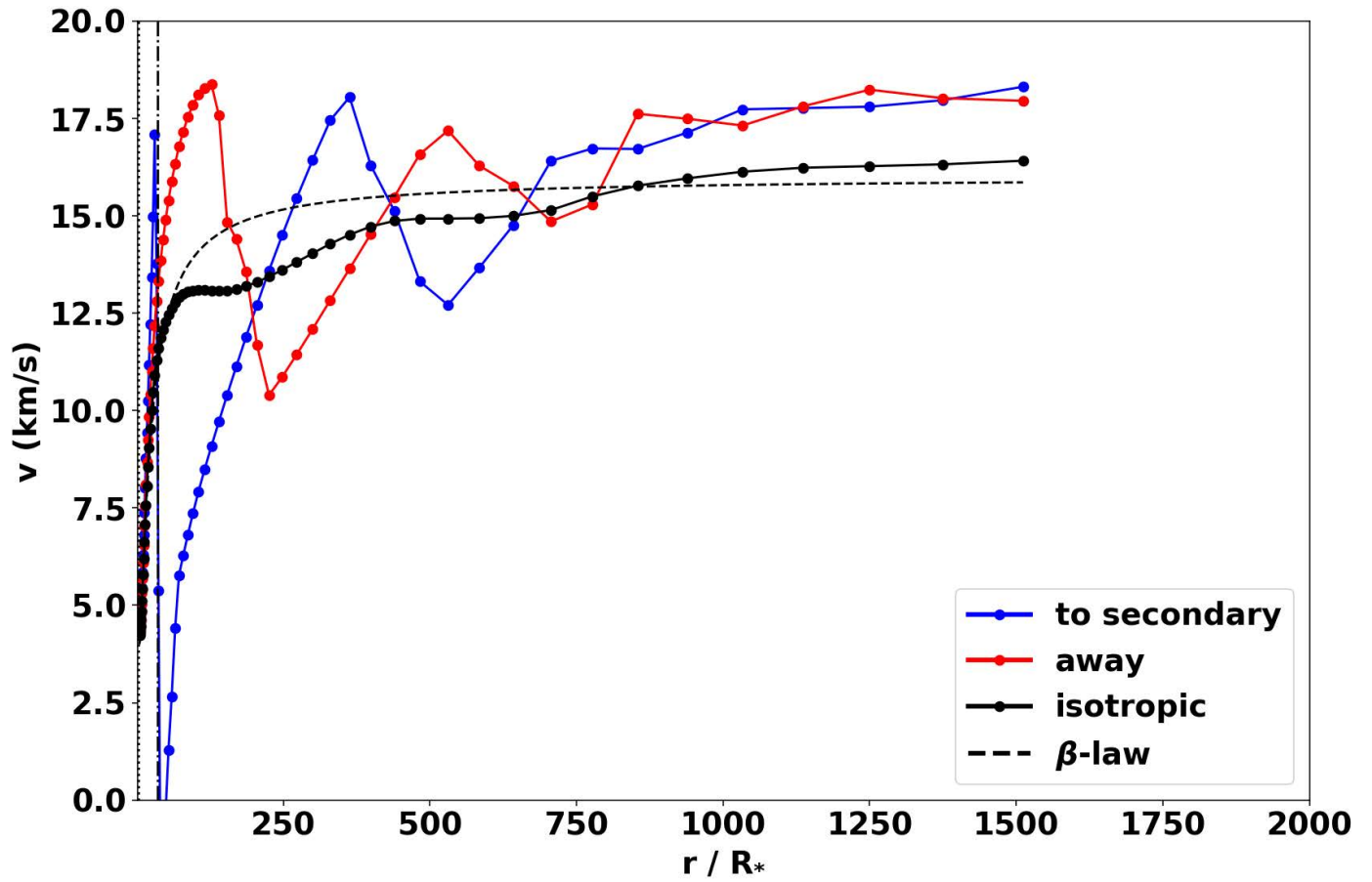
Fig. A.1. Illustration of the impact of a binary companion on the velocity field. This is the same as Fig. 10, except it has been replotted with a linear x-axis.
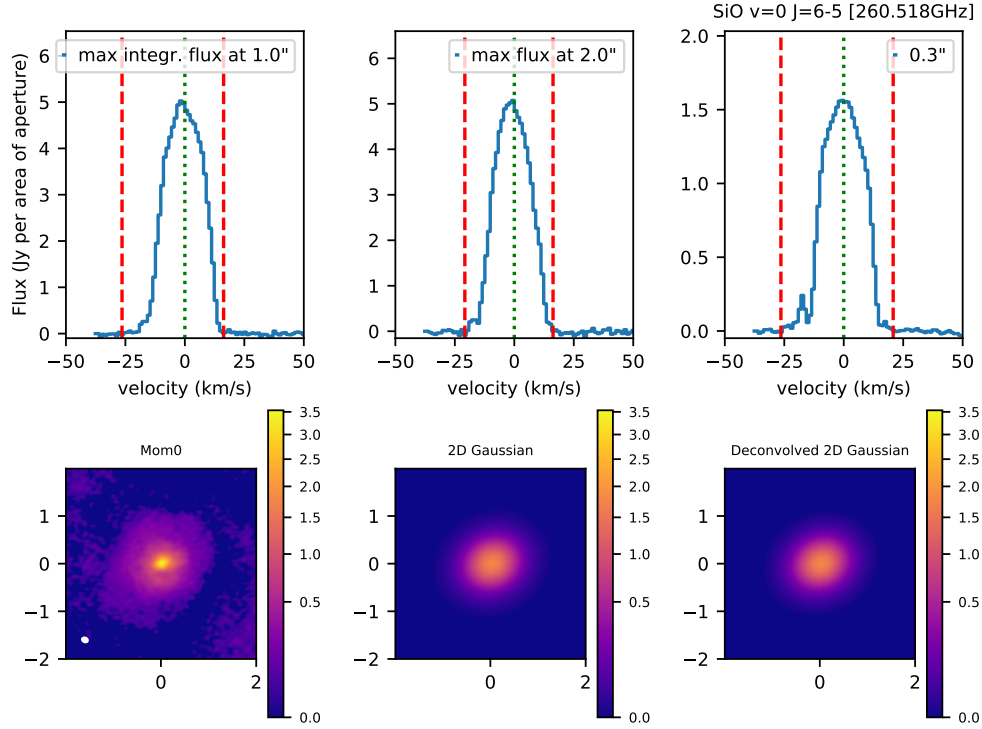
Fig. A.2. Determination of the velocity measure and angular emission zone for the SiO $v = 0$ J=6-5 transition of the medium resolution data of IRC −10529. *Top row:* The maximum integrated flux is attained for an extraction aperture of 1''0 (left panel), the peak flux is maximal for an extraction aperture of 2''0 (middle panel), and for each transition a reference spectrum at 0''3 is plotted (right panel). The velocity (in km s^{-1}) is with respect to the stellar velocity of −16.3 km s^{-1} (see the last column in Table 1). The dotted green vertical line in the spectra indicates the central frequency, and the two dashed red lines indicate the determination of the velocities of the red and blue wings. In the example here, the velocity derived for the SiO line (v(SiO)=26.4 km s^{-1}) is larger than the velocity determined from the low resolution CO $v = 0$ $J = 2 − 1$ line (v(CO)=21.8 km s^{-1}). *Bottom row:* The first image is the moment0 map, the second image the 2D Gaussian fit to the moment0-map, and the last plot the image for the deconvolved 2D Gaussian profile. The colour scales in the moment0 maps are in units of Jy/beam km s^{-1}. The ALMA synthesized beam is shown as a white ellipse in the lower left corner of the moment0 map.
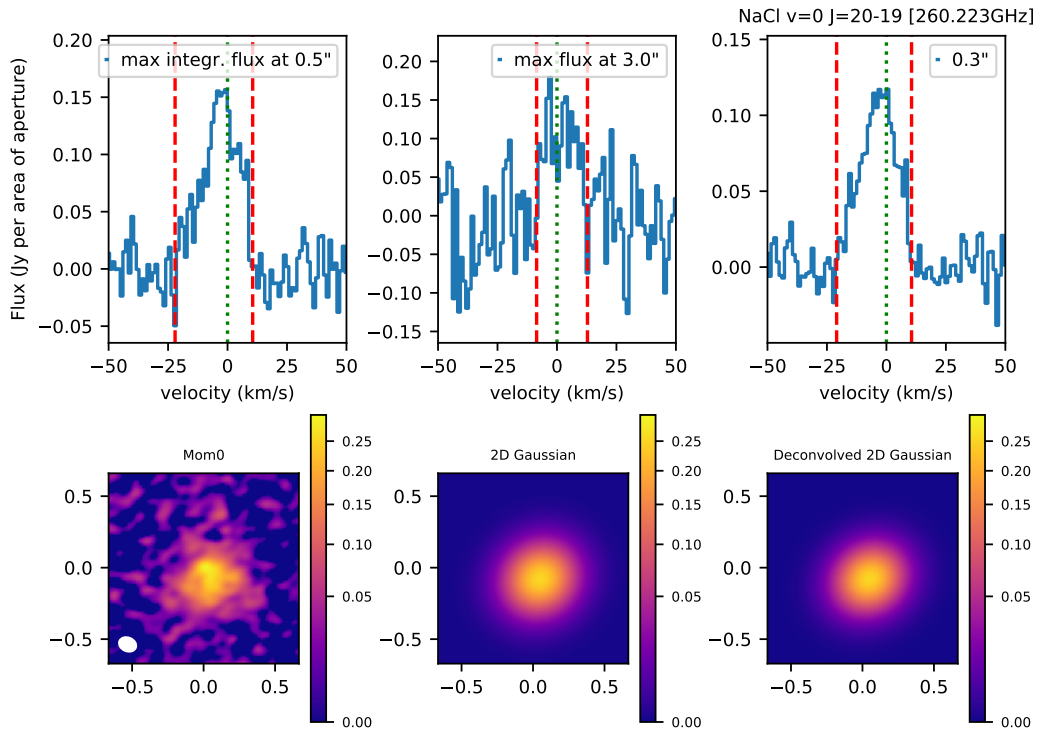
Fig. A.3. Determination of the velocity measure and angular emission zone for the NaCl $v = 0$ J=20-19 transition of the medium resolution data of IRC −10529. The velocity (in km s^{-1}) is with respect to the stellar velocity of −16.3 km s^{-1} (see the last column in Table 1). The colour scales in the moment0 maps are in units of Jy/beam km s^{-1} (see Fig. A.2 caption).
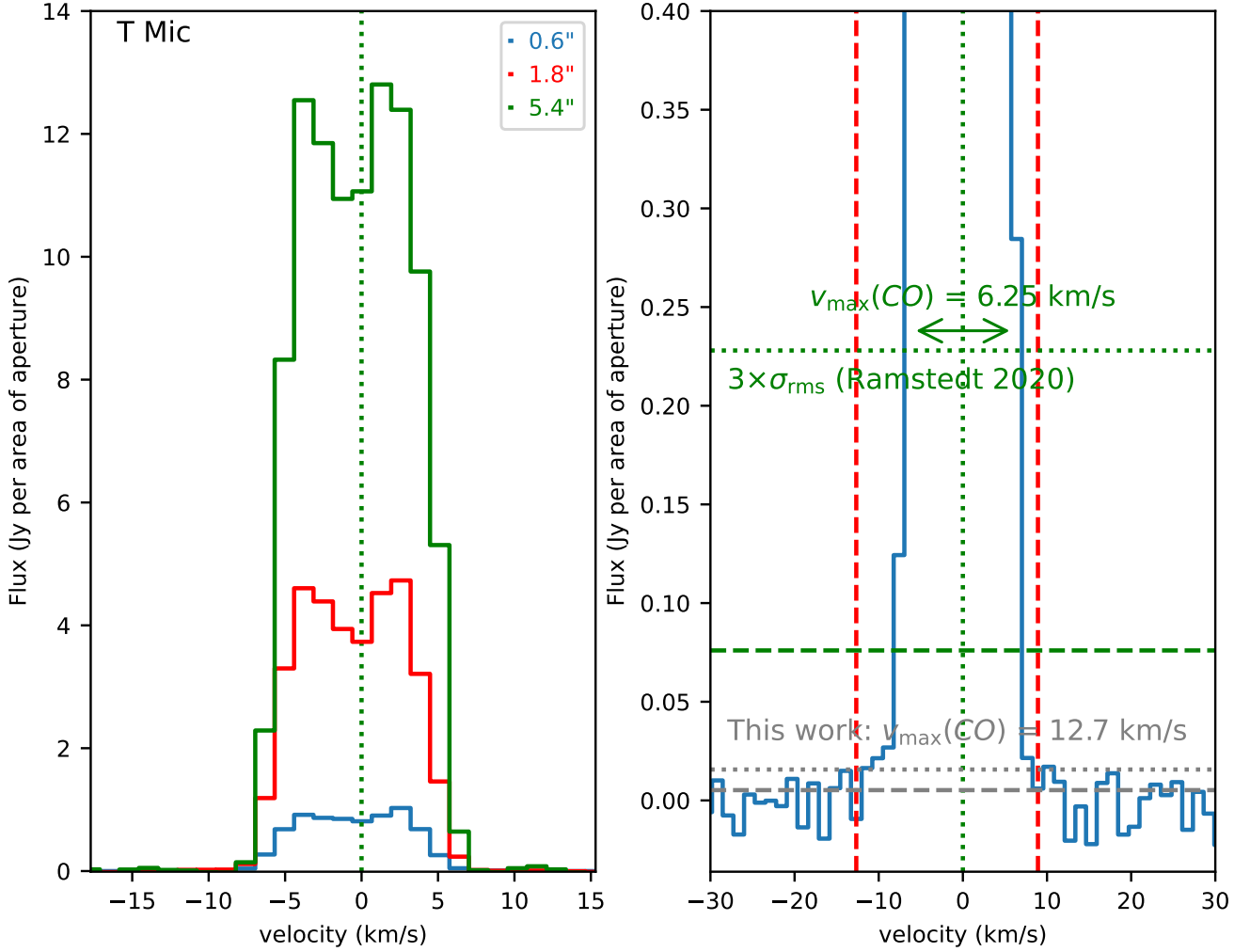
Fig. A.4. The $J = 2-1$ line of CO at 230,538.000 MHz observed in T Mic in the compact configuration. The plots show how (in the example of T Mic) the velocity (v_{max}) was derived from the molecular lines observed in the ATOMIUM survey. *Left:* The CO spectra extracted with apertures of radius 0.6″ (blue), 1.8″ (red), and 5.4″ (green). *Right:* The CO profile extracted with an aperture of radius 2.06″ is plotted on an expanded flux density scale with a full scale amplitude of 0.4 Jy/beam to better discern the red and blue wings. The horizontal dashed grey line at 5 mJy beam^{-1} corresponds to the 1σ peak rms noise (see point #2 in Sect. 5.2); the horizontal dotted grey line at 15 mJy beam^{-1} corresponds to the 3σ peak rms noise; the green dotted vertical line denotes the line center of CO at the v_{LSR} of +25.5 km/sec; and the red dashed vertical lines indicate the blue wing velocity of -12.7 km s^{-1}, and the red wing velocity of 8.9 km s^{-1}. The value of v_{max}(CO) with the largest magnitude – i.e., the blue wing velocity of 12.7 km s^{-1} – is designated as the 'velocity measure' of the CO $J = 2 - 1$ transition in T Mic (see Sect. 5.2). Similarly, the dashed green horizontal line at 76 mJy beam^{-1} corresponds to the $1\sigma_{rms}$ noise in the Band 6 spectrum of CO observed in T Mic by Ramstedt et al. (2020, see Table B.1). The dotted green horizontal line at 228 mJy beam^{-1} corresponds to the $3\sigma_{rms}$ noise and to the point where the full width of the CO $J = 2 - 1$ line profile is equal to 12.5 km s^{-1}, whereby Ramstedt et al. determined v_{max}(CO) = 6.25 km s^{-1}.

Appendix B: Medium angular resolution spectra of IRC −10529

In this section, we provide the additional spectra extracted from the medium resolution data of IRC −10529 for cubes 02–15. The spectra for cubes 00 and 01 are shown in Fig. 7.
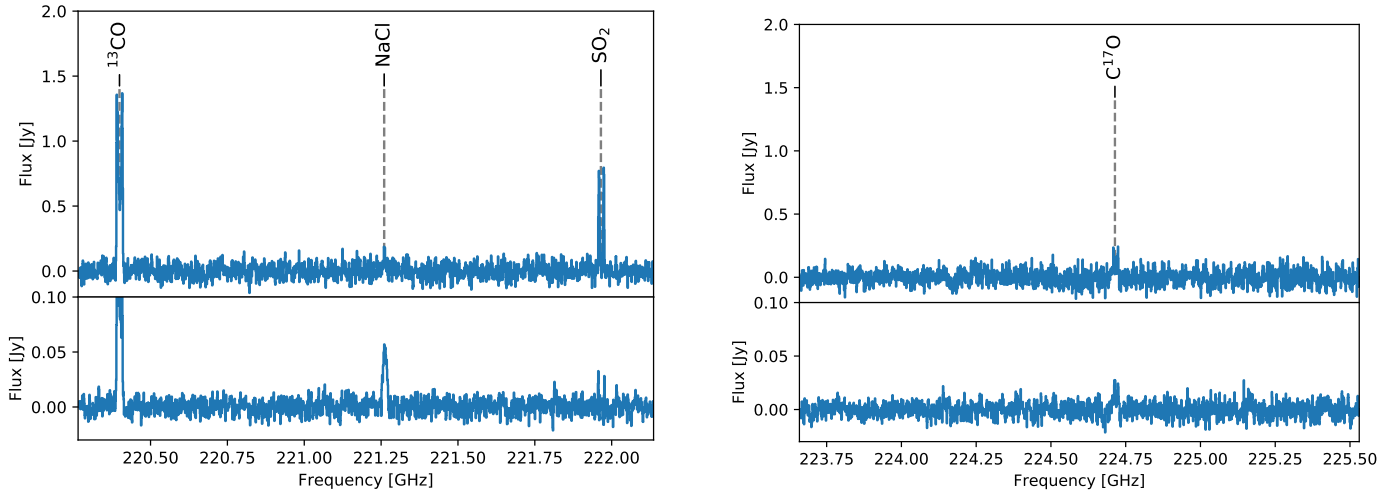
Fig. B.1. ALMA spectra of IRC −10529. Caption; see Fig. 7. Data are displayed for cubes 02 to 03.
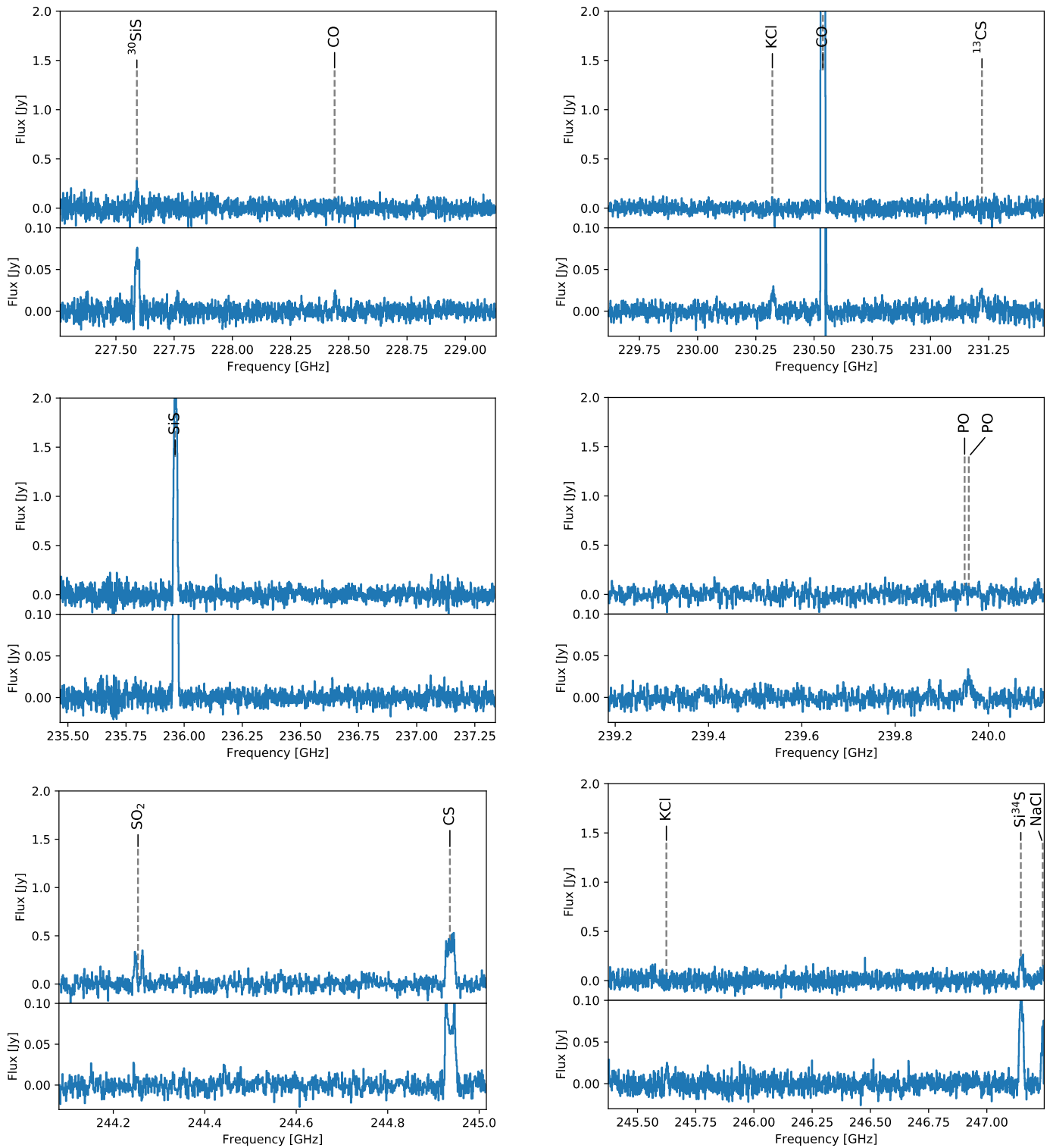
Fig. B.2. ALMA spectra of IRC −10529. Caption; see Fig. 7. Data are displayed for cubes 04 to 09.
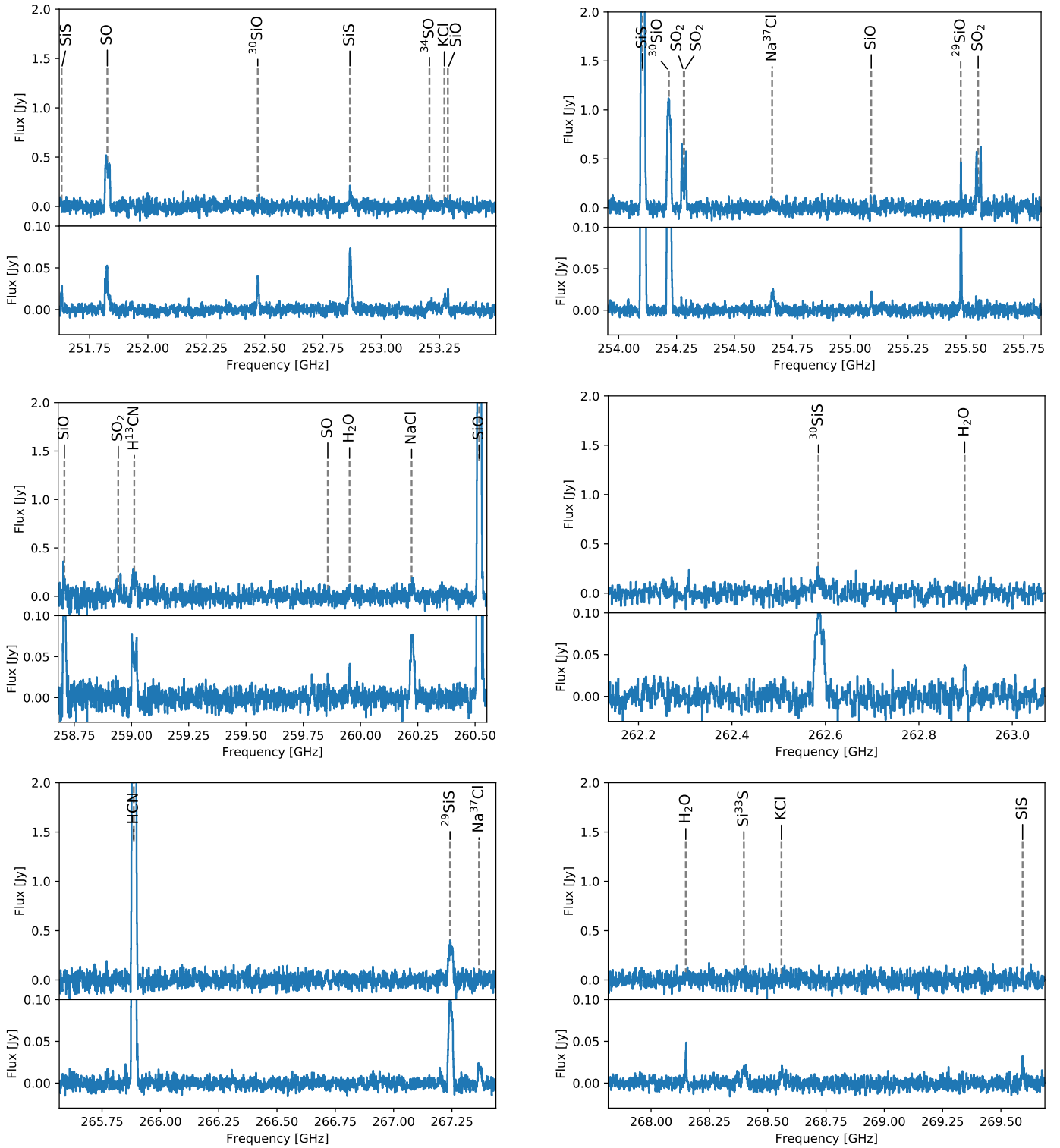
Fig. B.3. ALMA spectra of IRC −10529. Caption; see Fig. 7. Data are displayed for cubes 10 to 15.

Appendix C: Wind kinematics for 15 ATOMIUM sources
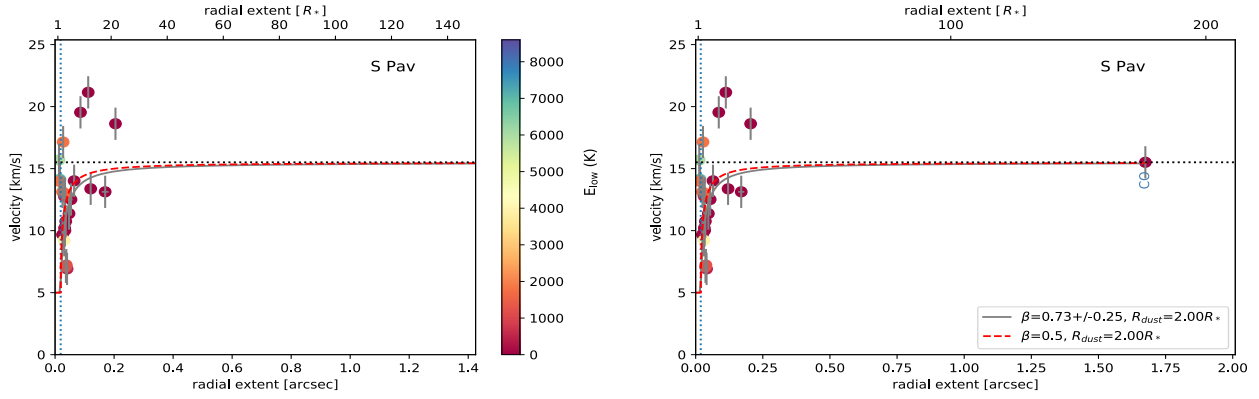
Fig. C.1. Wind kinematics for S Pav. See Fig. 11 caption.
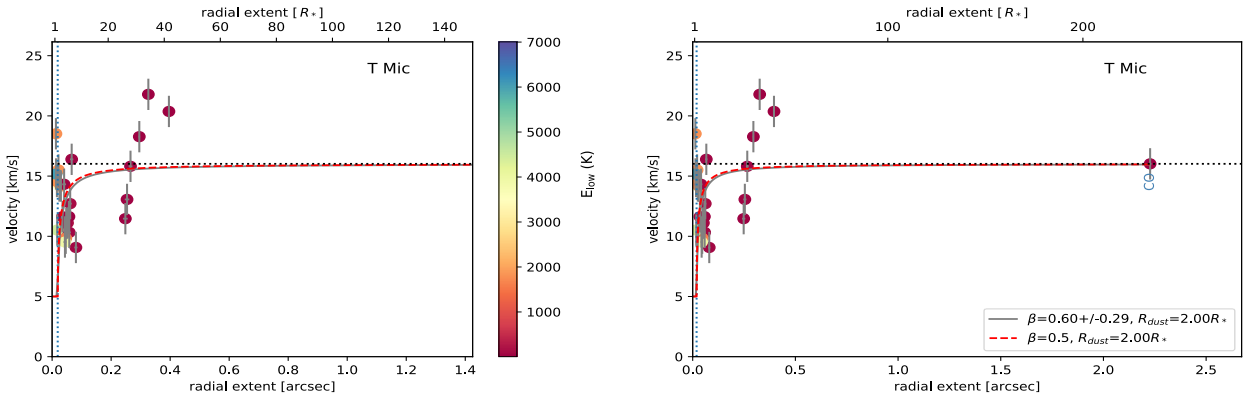
Fig. C.2. Wind kinematics for T Mic. See Fig. 11 caption.
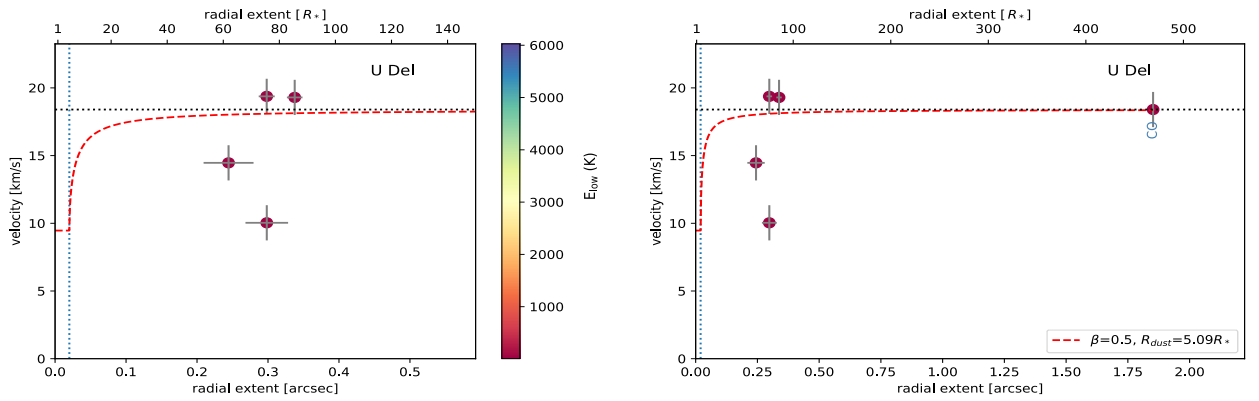
Fig. C.3. Wind kinematics for U Del. See Fig. 11 caption. Not enough data are available for a reliable determination of the β parameter.
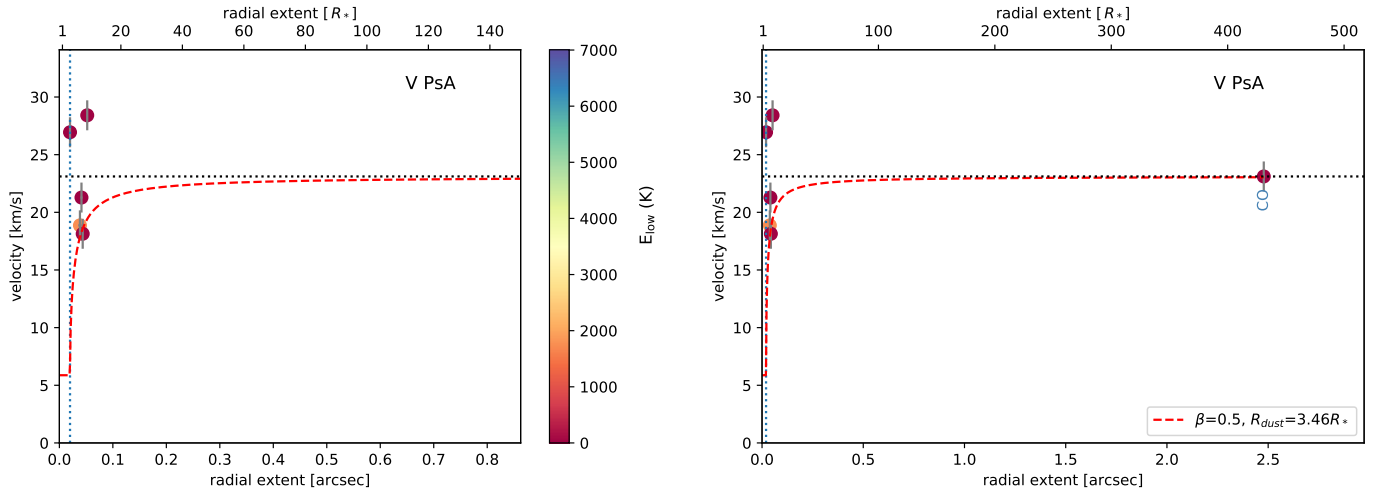
Fig. C.4. Wind kinematics for V PsA. See Fig. 11 caption. Not enough data are available for a reliable determination of the β parameter.
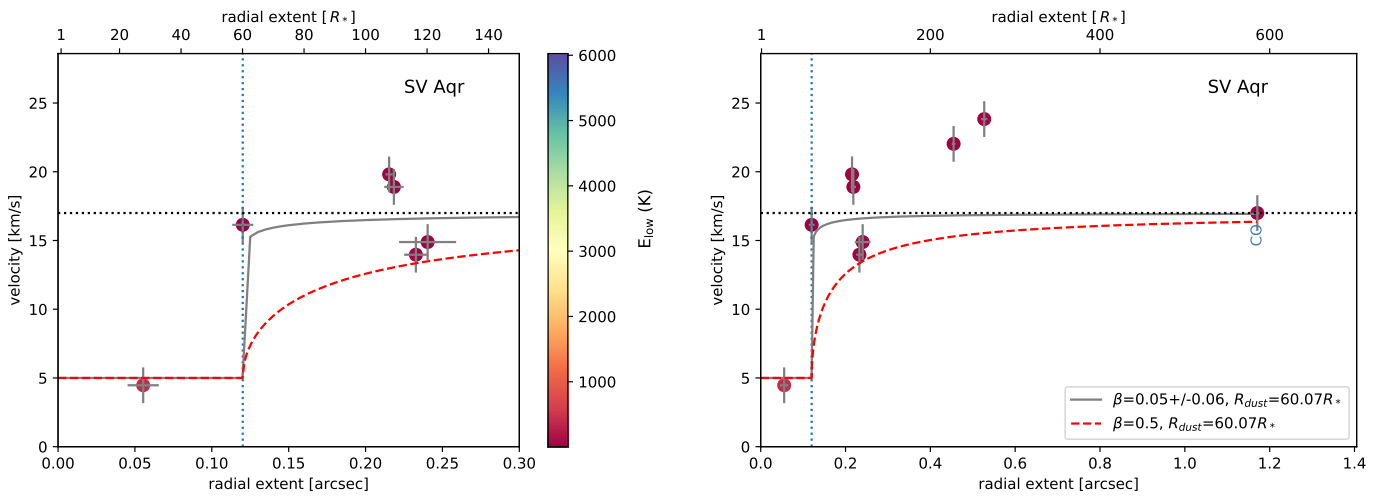
Fig. C.5. Wind kinematics for SV Aqr. See Fig. 11 caption. Not enough data are available for a reliable determination of the β parameter.
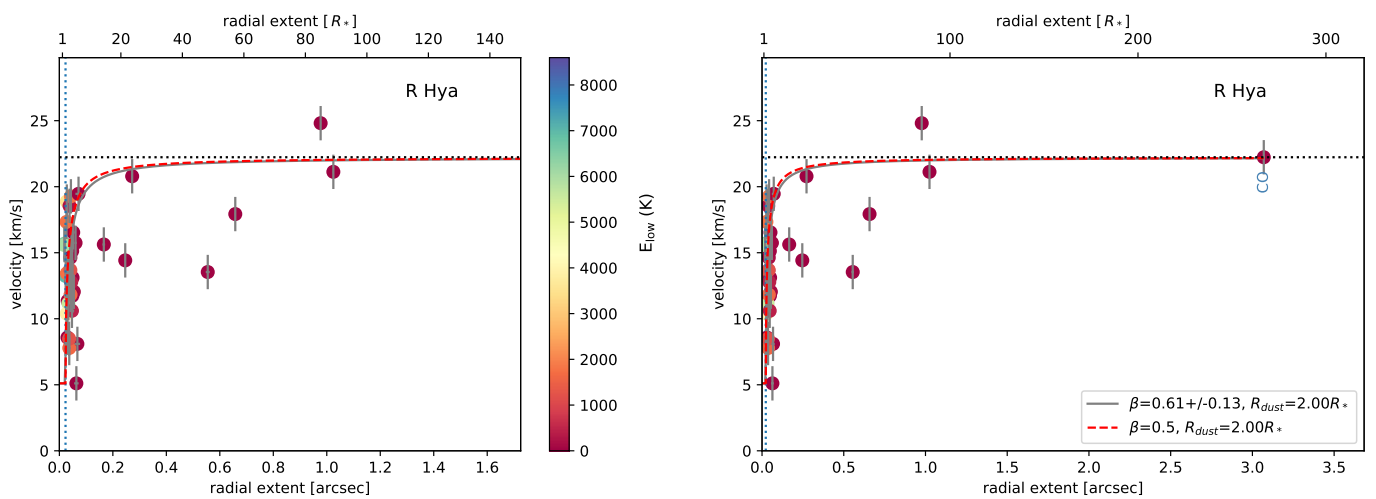
Fig. C.6. Wind kinematics for R Hya. See Fig. 11 caption.
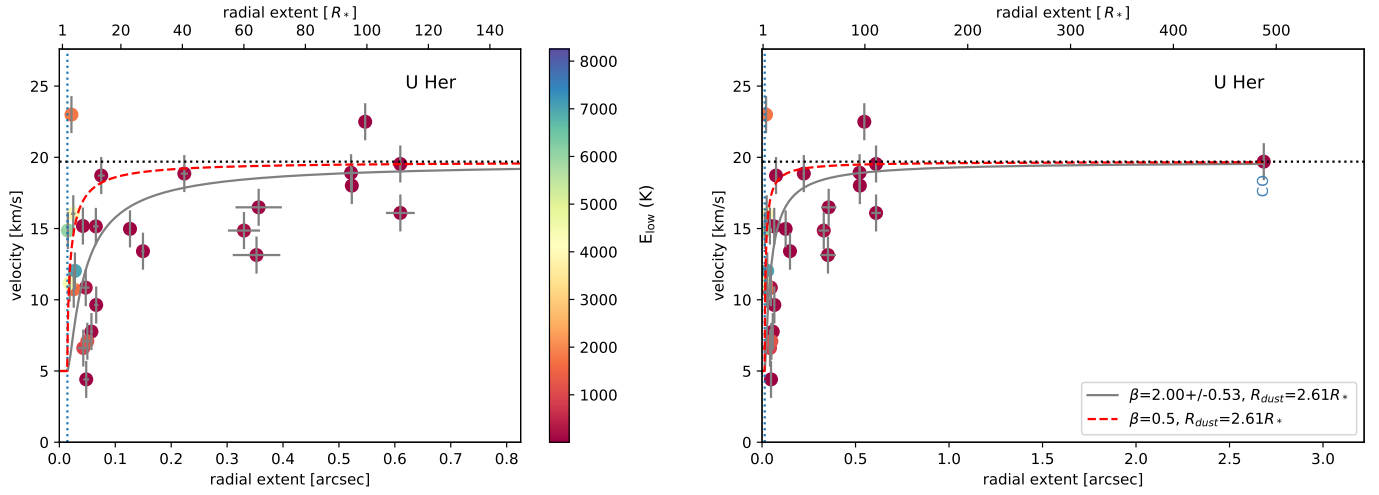
Fig. C.7. Wind kinematics for U Her. See Fig. 11 caption.
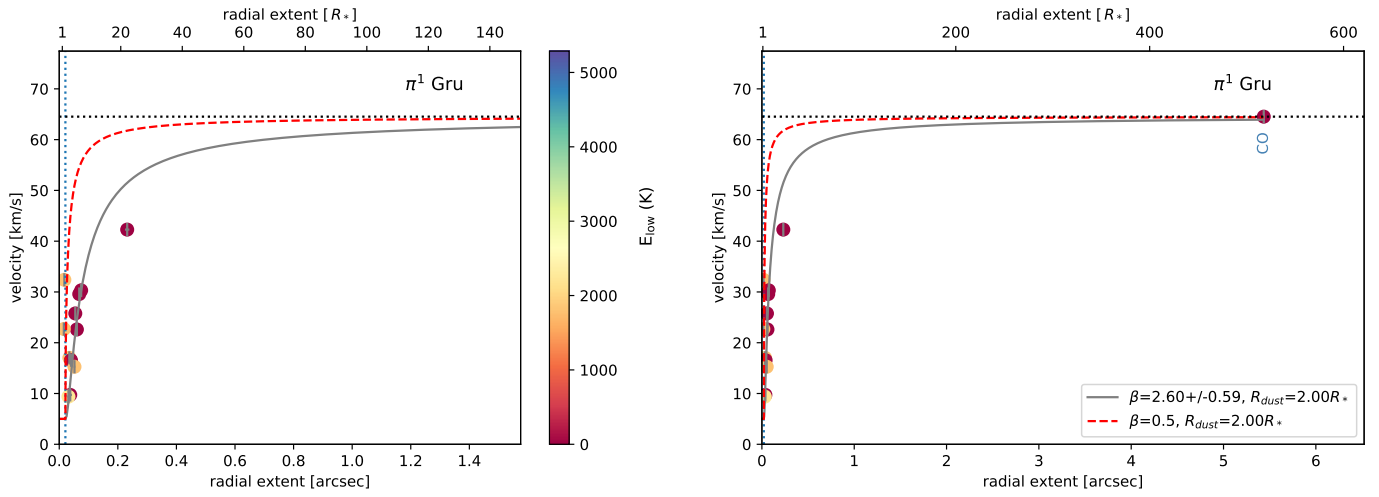
Fig. C.8. Wind kinematics for π^1 Gru. See Fig. 11 caption.
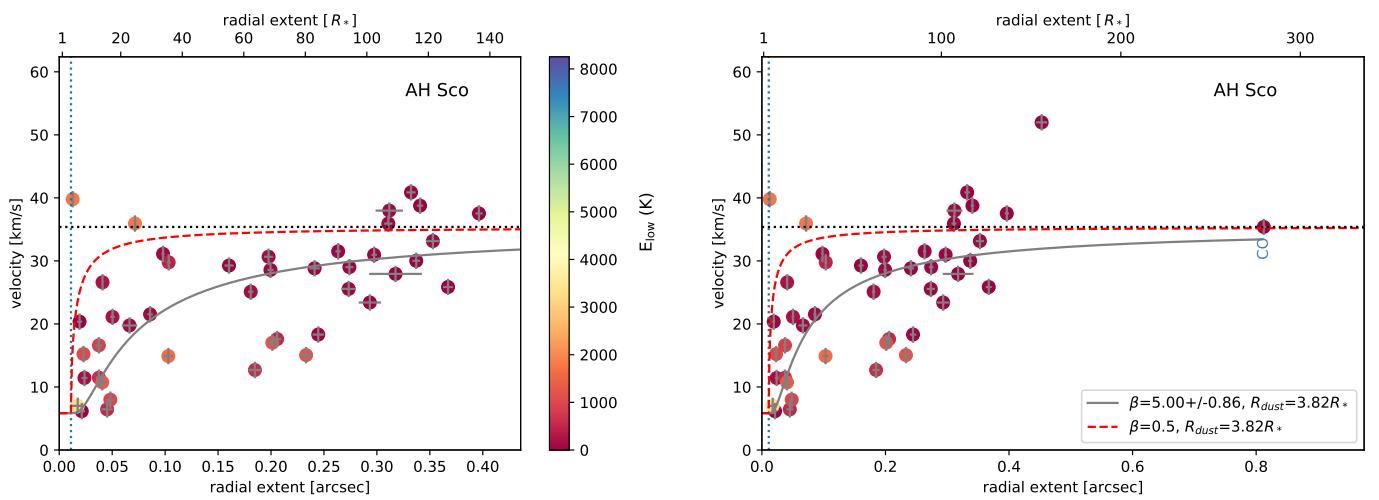
Fig. C.9. Wind kinematics for AH Sco. See Fig. 11 caption. Wind velocity profile constructed only on the basis of the medium and high spatial resolution data, since the low spatial resolution data still need to be acquired.
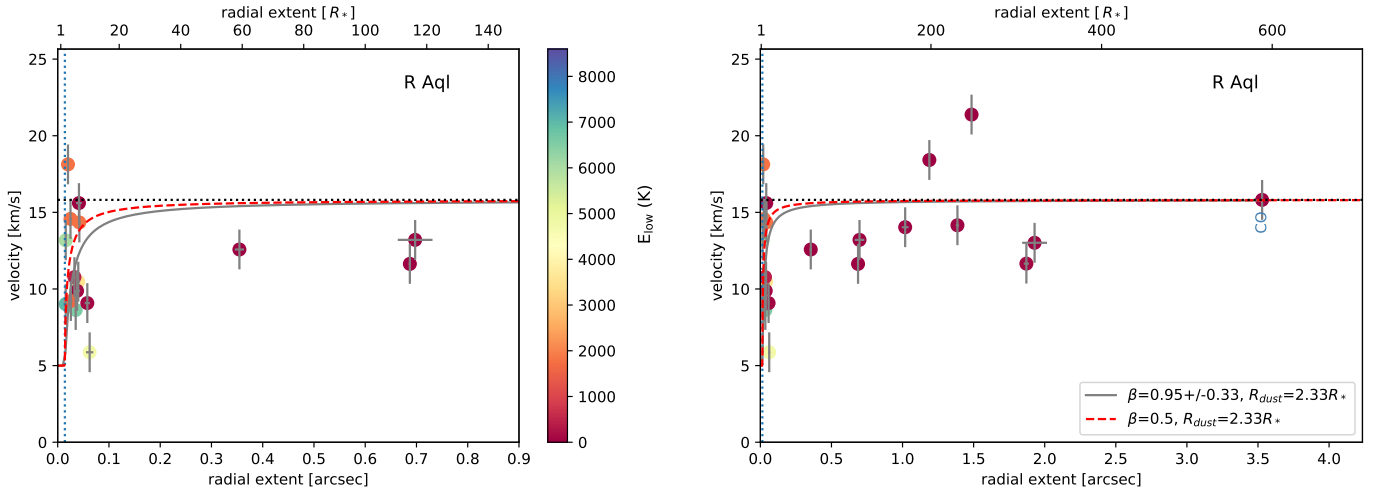
Fig. C.10. Wind kinematics for R Aql. See Fig. 11 caption.
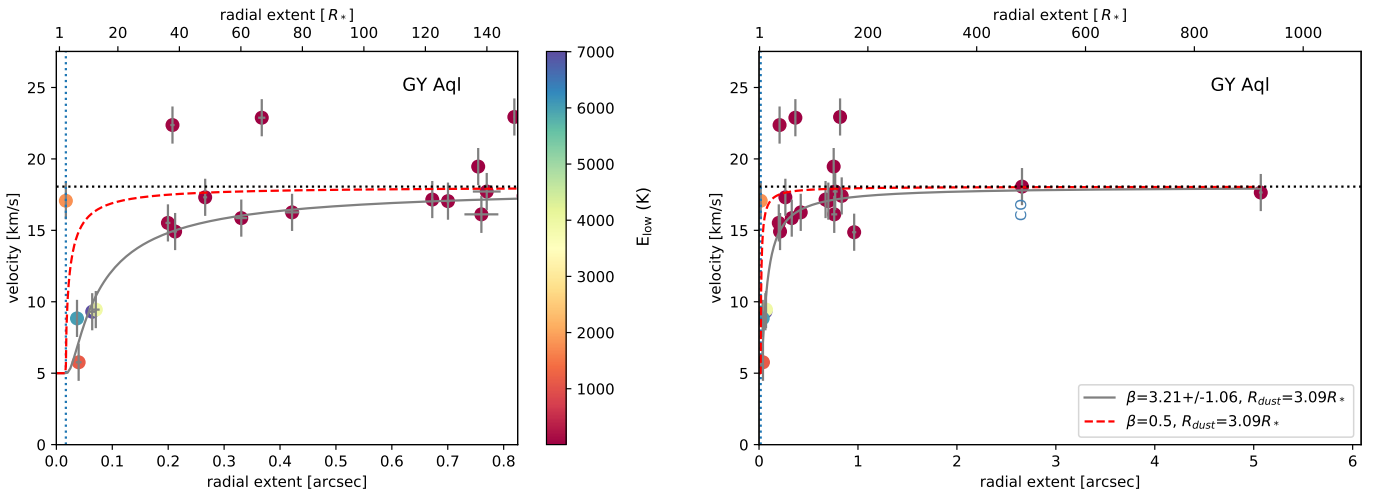
Fig. C.11. Wind kinematics for GY Aql. See Fig. 11 caption.
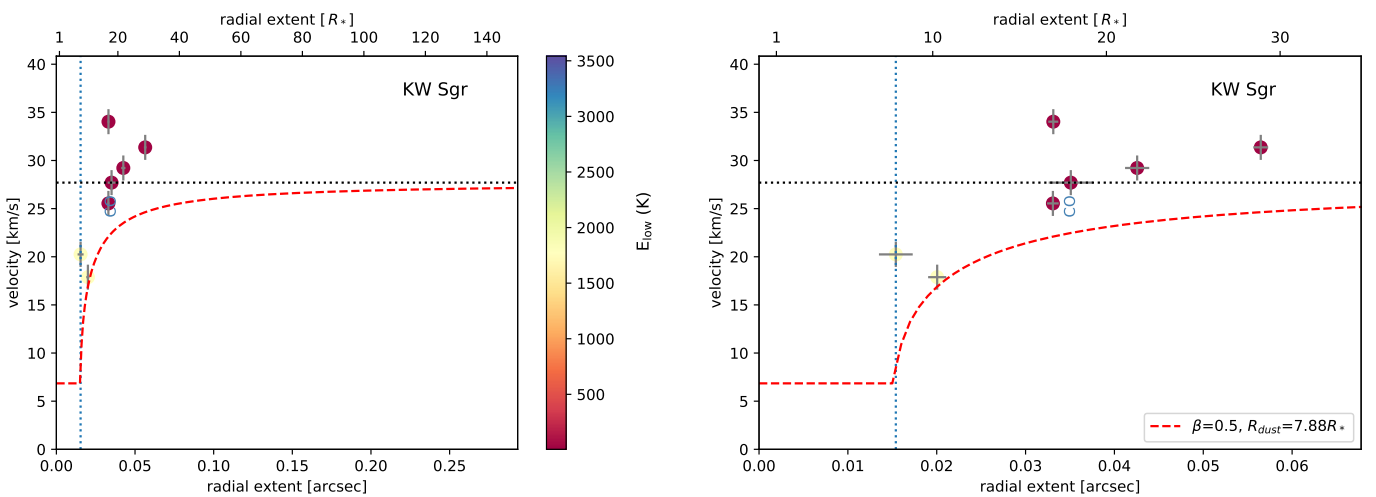
Fig. C.12. Wind kinematics for KW Sgr. See Fig. 11 caption. Wind velocity profile constructed only on the basis of the medium and high spatial resolution data, since the low spatial resolution data still need to be acquired. Not enough data are available for a reliable determination of the β parameter. Since the ^{12}CO $v = 0$ $J = 2 - 1$ remains undetected in the medium-resolution data, the CO extent is deduced from the high-resolution data.
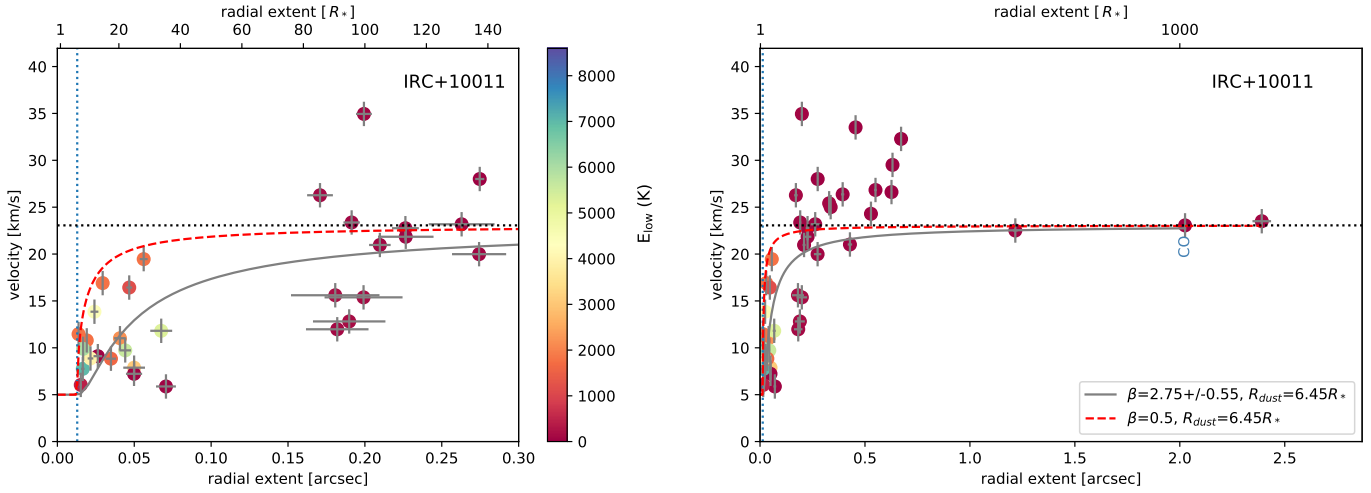
Fig. C.13. Wind kinematics for IRC +10011. See Fig. 11 caption.
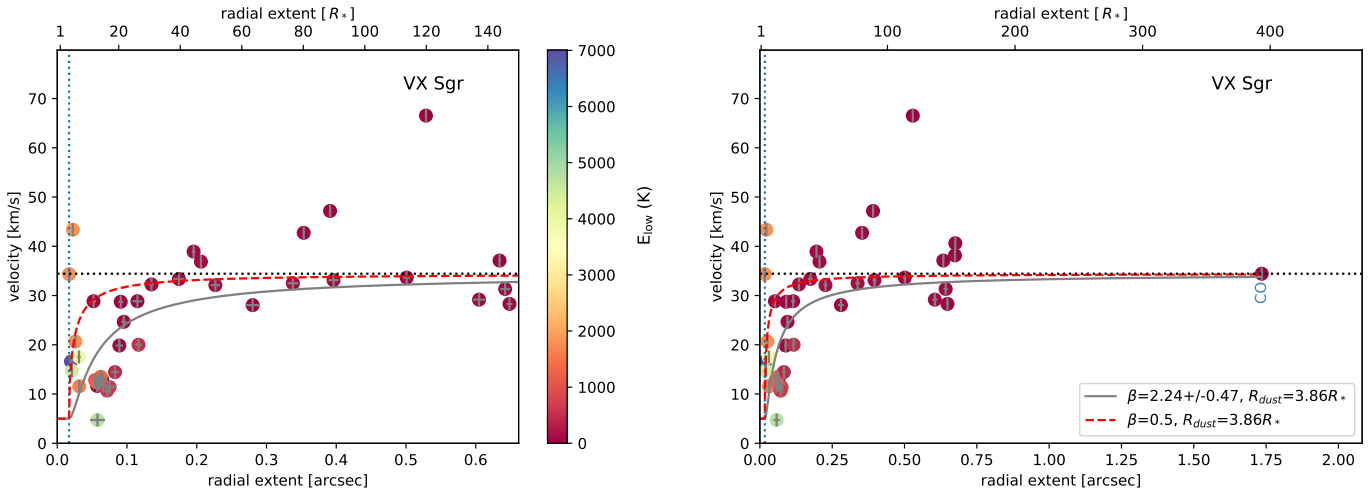
Fig. C.14. Wind kinematics for VX Sgr. See Fig. 11 caption.
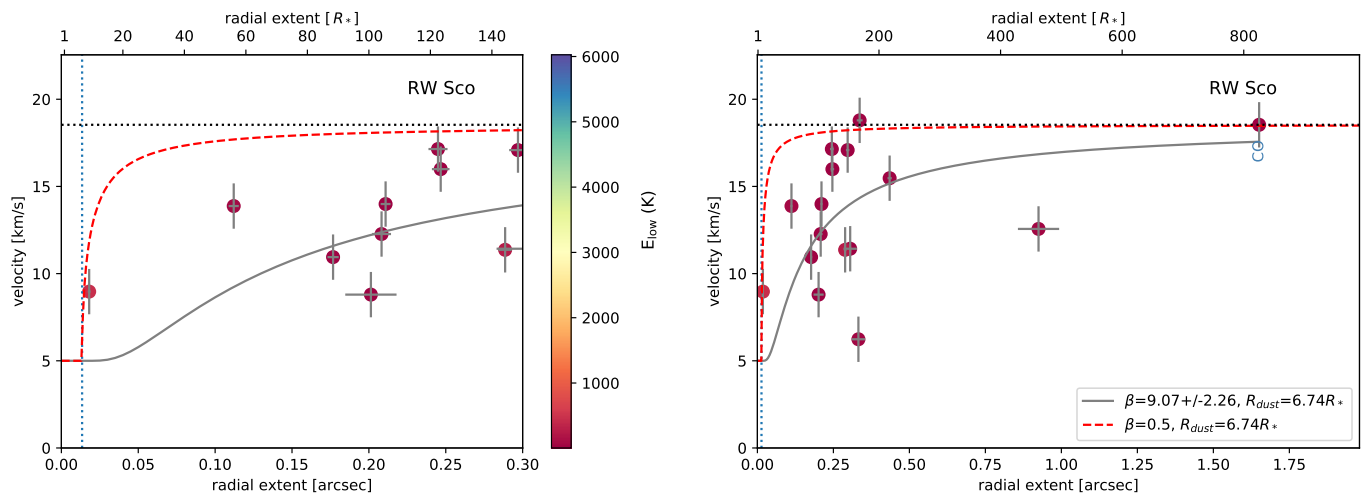
Fig. C.15. Wind kinematics for RW Sco. See Fig. 11 caption.

Appendix D: Determining the terminal wind velocity and the impact of pulsation-induced shocks on the velocity measure

In the main paper, we argue that the ^{12}CO $v = 0$ $J = 2 − 1$ line in the low resolution ATOMIUM data can be used to determine the terminal wind velocity, and its integrity as a diagnostic is not perturbed by pulsation-induced shocks that occur in the innermost few stellar radii. We base our arguments on theoretical simulations of a smooth spherically symmetric wind in which the parameters resemble R Aql (see Table 1). The level populations and corresponding intensities of CO in the simulations were computed on the assumption of a CO abundance of $[CO/H_2] = 2 \times 10^{-4}$ with the (3D) non-LTE radiative transfer code MAGRITTE by De Ceuster et al. (2020a,b) which includes the CMB. The parameters for R Aql resemble the stellar parameters in Table 1 in the main text. The temperature profile is assumed to be similar to that of Danilovich et al. (2017, 2020a): $T(r) = T_\star (R_\star/r)^{0.65}$; and the collisional rates and Einstein A coefficients were taken from the LAMDA database (van der Tak et al. 2020; Yang et al. 2010; Schöier et al. 2005).

In the first set of models, the wind velocity profile follows the analytic expression of Eq. (4) with parameters $v_0 = 1 \, \mathrm{km \, s^{-1}}$, $v_\infty = 12.8 \, \mathrm{km \, s^{-1}}$, and $\beta = 1$, or 5. Depicted in Fig. D.1 are the ^{12}CO $v = 0$ $J = 2 − 1$ velocity measures as a function of the aperture size. It is evident that the CO velocities grow when the aperture size increases from small to large scales. The velocity measure can be larger than the input terminal wind velocity of $12.8 \, \mathrm{km \, s^{-1}}$, owing to the effect of thermal broadening ($v_{\mathrm{therm}} = \sqrt{2kT/m}$) and turbulent broadening ($v_{\mathrm{turb}} = 1.5 \, \mathrm{km \, s^{-1}}$) that is accounted for in the full width at half maximum of the Gaussian broadened profile (i.e., $\mathrm{FWHM} = 2\sqrt{2 \ln 2}\sigma$, where $\sigma = \sqrt{v_{\mathrm{therm}}^2 + v_{\mathrm{turb}}^2}$). An increase in sensitivity of the observations (and hence a lower noise value) yields a more accurate sampling of the weak wings of the line profile where the broadening manifests itself – particularly in the case of optically thick line profiles (De Beck et al. 2012). The blue-wing velocity measure is often smaller than the corresponding red-wing velocity measure, owing to the effect of the blue wing absorption (Morris et al. 1985; Schoenberg 1988).

The combined ATOMIUM data is optimal for establishing whether the increase in CO velocities with aperture size is a general trend. To date, the data for the three separate spatial resolutions and the combined dataset are available for six stars: R Hya, π^1 Gru, R Aql, IRC -10529, IRC $+10011$, and VX Sgr, but only π^1 Gru has been analysed in detail (Homan et al. 2020). Shown in Fig. D.2 is the change in velocities of the ^{12}CO $v = 0$ $J = 2 − 1$ and ^{28}SiO $v = 0$ J=5-4 lines with aperture size when they are extracted from the combined datasets for the 6 sources by following Step 1 and Step 2 in Sect. 5.2. In Fig. D.2 we also compare the velocity profiles with the velocity measure extracted from the low-resolution ATOMIUM data for the ^{12}CO $v = 0$ $J = 2 − 1$ line [see $v_\infty^{\mathrm{com}}(CO)$ in column (3) of Table 3]. For most sources – except for the blue-shifted velocity in IRC $+10011$, and the red-shifted velocity in R Hya – the CO velocity grows with increasing aperture size and reaches a plateau beyond $\sim$100 stellar radii. The velocity measure [$v_\infty^{\mathrm{com}}(CO)$] derived from the ^{12}CO $v = 0$ $J = 2 − 1$ data at low angular resolution is a good tracer for the plateau and the terminal wind velocity, provided the thermal broadening, the turbulent broadening, and the spectral resolution of $\sim$1.3 km s^{-1} are accounted for.

Understanding how pulsation-induced shocks might impact the velocity measure has a strong bearing on the interpreta-

tion of the observationally derived wind kinematics discussed in Sect. 5.4. Analogous to Fig. D.1, we used the non-LTE radiative transfer code MAGRITTE (De Ceuster et al. 2020a,b), but this time rather than using the standard beta-law wind profiles from Eq. (4), the wind velocity profile has been modified to mimic the effect of pulsation-induced shocks within a 1D wind geometry. We used the results of Bladh et al. (2019, see their Fig. 1), which we extrapolated to larger distances from the star by using a fit that follows a beta-velocity profile (see left panel in Fig. D.3). The output image is then run through the ALMA simulator tool for setups resembling the compact, medium, and extended configurations. The simulated output data are then treated in the same way as the ATOMIUM data for the extraction of the velocity measure as a function of the aperture size by following Step 1 and Step 2 in Sect. 5.2 (see the panels labelled 'normal shock' model in Fig. D.4). Two main conclusions can be drawn from comparing the 'no shock' (upper row) and 'normal shock' (middle row) panel of ^{12}CO $v = 0$ $J = 2 − 1$: (1) for the case in which the velocity of the shock amplitude is lower than the terminal wind velocity, it is apparent that the velocity measure extracted from the compact CO $v = 0$ $J = 2 − 1$ data is the same for the 'no shock' and 'normal shock' model, confirming that the compact CO $v = 0$ $J = 2 − 1$ data is a good measure of the terminal wind velocity (if the effect of thermal and turbulent broadening, and the spectral resolution of the ATOMIUM data are accounted for); and (2) the velocity measures derived from the ^{12}CO extended configuration data are slightly higher if shocks are accounted for, with the shocks manifesting themselves in the faint more extended wings.

We also computed the SiO $v = 0$ J=5-4 intensities by following the same procedure as for CO (see right hand panels in Fig. D.4). To account for the depletion of SiO by dust condensation and its potential dissociation, the relative abundance distribution of SiO was assumed to follow a Gaussian of the form (Decin et al. 2010b; Danilovich et al. 2014)

$$[SiO/H_2] = 3 \times 10^{-5} \exp\left(-(r/r_e)^2\right), \tag{D.1}$$

where the e-folding radius r_e (2.3×10^{16} cm) was determined by following González Delgado et al. (2003). In spite of its lower abundance, the detectable extent of the SiO $v = 0$ J=5-4 line observed in the extended configuration is a factor $\sim$2 larger than for CO $v = 0$ $J = 2 − 1$ (0″09 versus 0″04), establishing the radiative nature of SiO (see Sect. 5.4.2). Analogous to CO, the effect of pulsation-induced shocks in the first few stellar radii — where velocities of around $7 − 12 \, \mathrm{km \, s^{-1}}$ are greater than the local sound speed – are observed in the smallest extraction apertures of the extended configuration data. As Fig. D.4 demonstrates, observations with spatial resolution better than 0″150 are a prerequisite for characterizing this complex region in more detail.

The question still remaining is whether and how physical phenomena yielding a velocity amplitude greater than the terminal wind velocity manifest themselves in the velocity measure. We therefore take an extreme example and multiply the shock amplitudes from Bladh et al. (2019) by a factor 3 (see right panel of Fig. D.3), where the outcome of the velocity measures are shown in the bottom panels of Fig. D.4 and are referred to as the 'strong shock' model. Here as well, several interesting conclusions can be drawn: (1) the compact configuration data of the ^{12}CO $v = 0$ $J = 2 − 1$ line are not affected by the presence of shocks in the inner wind, and hence these data are a reliable tracer of the terminal wind velocity given the line broadening and spectral resolution of the data; (2) the extended configuration data of both the ^{12}CO $v = 0$ $J = 2 − 1$ and ^{28}SiO $v = 0$
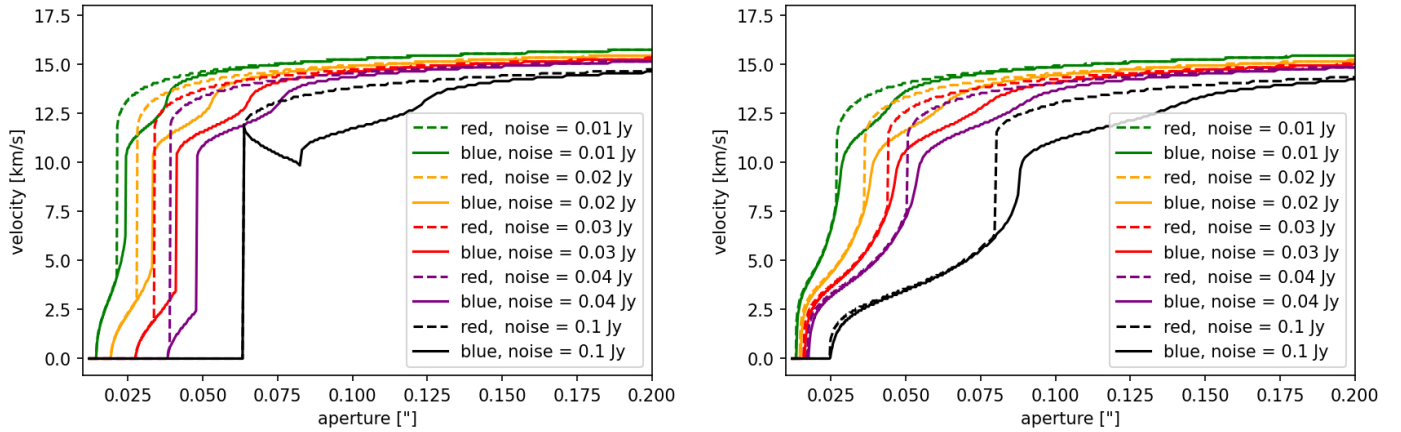
Fig. D.1. Change in the ^{12}**CO** $v = 0$ $J = 2 - 1$ **velocity measure as a function of the aperture size.** The velocity measures are extracted for a range of aperture sizes and noise levels following the same procedure as outlined in Step 2 in Sect. 5.2. The *left panel* is constructed for a velocity profile with $\beta = 1$ and the *right panel* for $\beta = 5$. Velocity measures extracted from the red (blue) wing are indicated with 'red' ('blue') in the legend in the panels.

J=5-4 line bear a signature of the extreme shock velocities in the first few stellar radii of the circumstellar envelope, especially in the case of SiO; and (3) the extreme shock velocities are not traced in both the medium and compact configuration data. With respect to the latter conclusion, it should be noted that if the rms were three times smaller than the present value, the weak extended wings could be better captured, thereby allowing the (shock) signature to be traced in the low and medium resolution data, although the convolution with the (Gaussian) broadening profile will also be tracked to lower intensity levels and hence yield broader profiles.

Our current physical understanding of pulsation-induced shocks, however, does not validate the use of the 'strong shock model', because both models and observations indicate complex, non-monotonic velocity fields with relative macroscopic motions of only some $10\,\mathrm{km\,s^{-1}}$ (Nowotny et al. 2010). Relying then on the simulations for the 'normal shock' model, the question that still needs to be addressed is why the observed SiO velocity measures can be significantly larger than that of CO as shown, for instance, for R Aql in Fig. D.2. Moreover, the same

figure shows a trend in SiO velocity measures that is not captured by any of the shock simulations shown in Fig. D.4 in which the medium and compact configuration data roughly show a constant velocity measure. Although detailed modelling of the ATOMIUM wind kinematic profiles is beyond the scope of this paper, the 1D simulations performed here can guide a thought experiment. A binary companion can impact the radial velocity field in a qualitatively similar way as pulsation-induced shocks in the sense that the radial velocity can have a wave-like character (see Fig. 10). The amplitude of the velocity variations will increase for more massive and closer-in companions, and can attain values well above $20\,\mathrm{km\,s^{-1}}$ where velocity variations of $40-60\,\mathrm{km\,s^{-1}}$ are not an exception (Maes 2020). Guided by the outcome of the 'strong shock' models, we stipulate that the particular behaviour of the wind kinematics profile in various ATOMIUM sources can be explained by binary interaction. The high velocities captured in the SiO measurements can be caused by, for instance, the gravitational well of the companion or the formation of an equatorial density enhancement with potentially a Keplerian velocity field similar to the case of L$_2$ Puppis (Kervella et al. 2016).
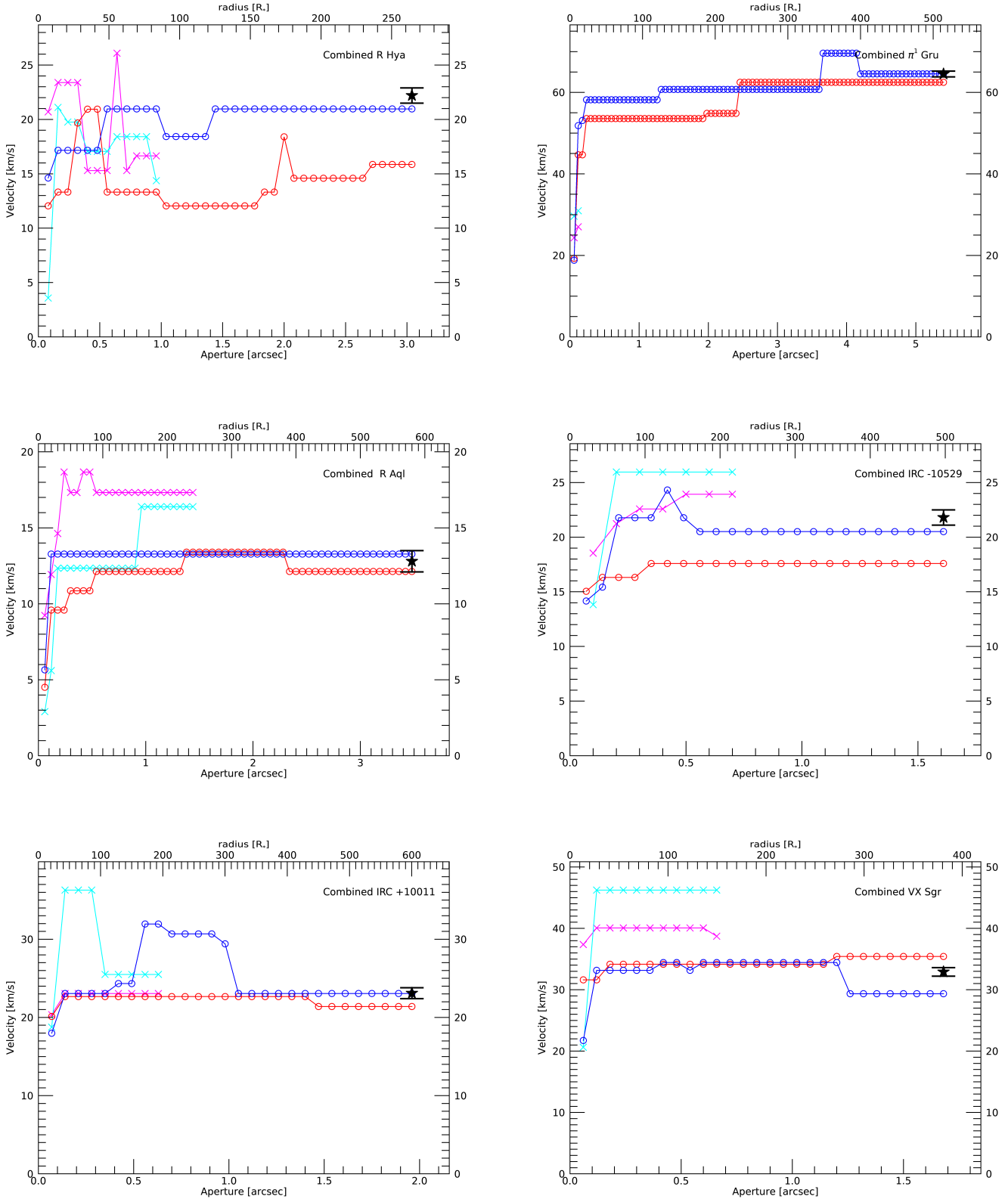
Fig. D.2. ^{12}CO $v = 0$ $J = 2-1$ **and** ^{28}SiO $v = 0$ **J=5-4 wind velocities of R Hya, π^1 Gru, R Aql, IRC −10529, IRC +10011, and VX Sgr.** Plots of the blue and red wing velocity of the ^{12}CO $v = 0$ $J = 2-1$ line (in blue and red, respectively) and the ^{28}SiO $v = 0$ J=5-4 line (in cyan and pink, respectively) derived from the ATOMIUM combined dataset for a range of extraction apertures for R Hya, π^1 Gru, R Aql, IRC −10529, IRC +10011, and VX Sgr, by following Step 1 and Step 2 in Sect. 5.2. The black star (★) denotes the ^{12}CO $v = 0$ $J = 2-1$ velocity extracted from the ATOMIUM low-resolution data, and the error bar denotes the approximate spectral resolution of 1.3 km s^{-1}.
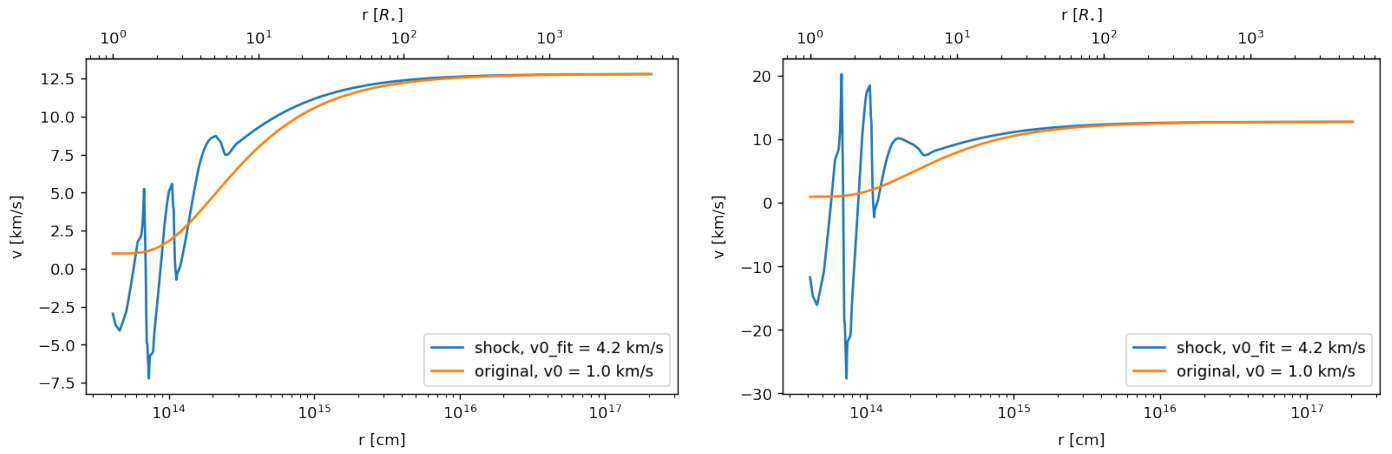
Fig. D.3. Wind velocity profile mimicking pulsation-induced shocks just above the stellar atmosphere. The orange curve shows a beta velocity wind profile for $\beta = 5$ and $v_0 = 1\,\mathrm{km\,s^{-1}}$. The blue curve in the *left panel* is constructed by: (i) using the shock velocity modelled by Bladh et al. (2019, see their Fig. 1) up to $\sim 10\,R_\star$ followed by; (ii) a beta velocity profile that is fitted through the velocity points beyond $\sim 8\,R_\star$, with $\beta = 5$ and the fit parameter v_0 which produces a smooth transition from the pulsation-dominated region towards the freely expanding wind region. In the *right panel*, the blue curve is constructed in a similar way as in the left panel, but this time the shock velocities modelled by Bladh et al. (2019) are multiplied by a factor of 3.
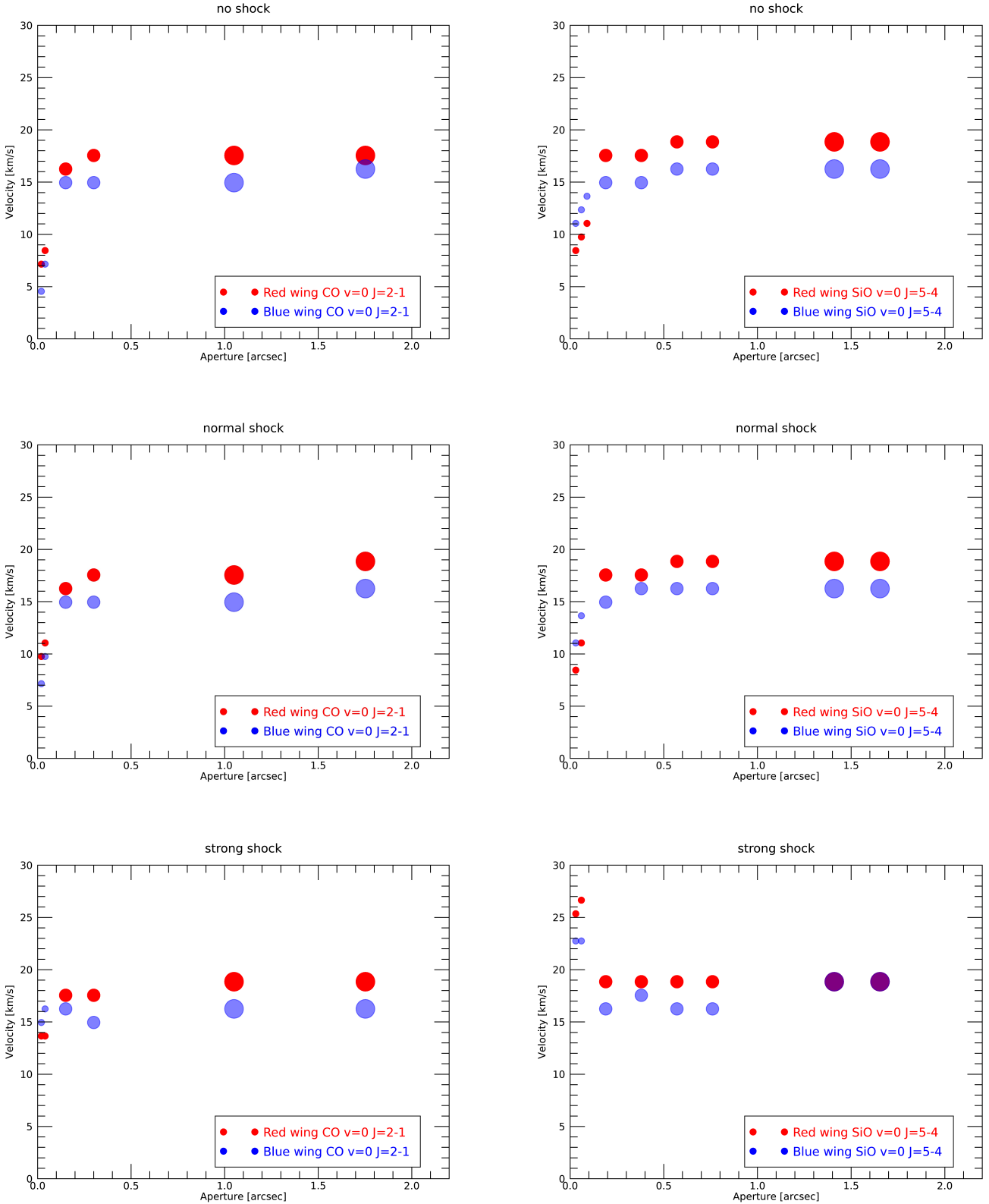
Fig. D.4. Simulated wind velocity measures for ^{12}**CO** $v = 0$ **J=2=1 (left) and** ^{12}**SiO** $v = 0$ **J=5-4 (right).** The upper row depicts the model without shocks, the middle (bottom) row the shocked wind model for the velocity profile shown in the left (right) panel of Fig. D.3. The calculated intensities of ^{12}CO and ^{12}SiO account for the different array configurations and extraction apertures in ATOMIUM (see Sect. 3 for details). The velocity measures for the extended (small dots), medium (medium-sized dots), and compact (large dots) configurations were extracted by following Step 1 and Step 2 in Sect. 5.2. The blue dots representing the blue wing velocities are slightly transparent to allow for visualising the red wing velocities in cases where the red and blue dots coincide.

Appendix E: ATOMIUM image cube properties

Each target's 'ALMA name' is of the form AH_Sco. Each Scheduling Block (SB) is then labelled AH_Sco_a_06_TM1 etc. for the extended configuration, where (a, b, c, d) denote each frequency combination as in Fig. 1. The mid configuration SBs are labelled similarly ending in TM2. The compact configuration data is labelled AH_Sco_e_06_TM1 etc. where (e, f) denote each frequency combination as in Fig. 1. However, for a few targets in compact, inconsistent capitalisation was used for the

target names and thus for the SBs. We made these consistent during data processing; the actual observing SB names are also given in Table E.1. The science spw in each SB tuning are numbered 25, 27, 29, 31 in ascending frequency. In the concatenated visibility data files, the spw become re-numbered in the order of observing time (thus, differing from target to target). For the final cubes that can be retrieved from the ATOMIUM website, we re-numbered these in frequency order 00, 01, · · · , 15. Tables E.2 and E.3 list the properties of each continuum and of each cube image, respectfully.

Table E.1. Observational properties of the ATOMIUM project.

SB	Config	Phase-ref	Phase-ref R.A. (ICRS)	Phase-ref Dec. (ICRS)	Sep. (deg)	PWV (mm)	Date (YYYYMMDD)	ASDM
AH_Sco_a_06_TM1	extended	J1717-3342	17:17:36.02945	−33:42:08.8277	1.91	0.4	20190706	uid___A002_Xde63ab_X9097
AH_Sco_a_06_TM1	extended	J1717-3342	17:17:36.02945	−33:42:08.8277	1.91	0.4	20190706	uid___A002_Xde63ab_X95c6
AH_Sco_b_06_TM1	extended	J1717-3342	17:17:36.02945	−33:42:08.8277	1.91	0.4	20190706	uid___A002_Xde63ab_X9b95
AH_Sco_b_06_TM1	extended	J1717-3342	17:17:36.02945	−33:42:08.8277	1.91	0.8	20190707	uid___A002_Xde8105_Xe0b
AH_Sco_c_06_TM1	extended	J1717-3342	17:17:36.02945	−33:42:08.8277	1.91	2.3	20190710	uid___A002_Xde9c3e_X7537
AH_Sco_c_06_TM1	extended	J1717-3342	17:17:36.02945	−33:42:08.8277	1.91	2.3	20190710	uid___A002_Xde9c3e_X7ad8
AH_Sco_c_06_TM1	extended	J1717-3342	17:17:36.02945	−33:42:08.8277	1.91	2.3	20190710	uid___A002_Xde9c3e_X7f89
AH_Sco_d_06_TM1	extended	J1717-3342	17:17:36.02945	−33:42:08.8277	1.91	1.4	20190708	uid___A002_Xde8105_X761c
AH_Sco_d_06_TM1	extended	J1717-3342	17:17:36.02945	−33:42:08.8277	1.91	1.4	20190708	uid___A002_Xde8105_X7c90
AH_Sco_a_06_TM2	mid	J1717-3342	17:17:36.02945	−33:42:08.8277	1.91	0.7	20190831	uid___A002_Xe0be64_Xb5b
AH_Sco_b_06_TM2	mid	J1717-3342	17:17:36.02945	−33:42:08.8277	1.91	0.7	20190831	uid___A002_Xe0be64_Xa0a
AH_Sco_c_06_TM2	mid	J1717-3342	17:17:36.02945	−33:42:08.8277	1.91	1.8	20190903	uid___A002_Xe0cd4d_X6a65
AH_Sco_d_06_TM2	mid	J1717-3342	17:17:36.02945	−33:42:08.8277	1.91	0.6	20181122	uid___A002_Xd58951_X6e47
GY_Aql_a_06_TM1	extended	J1951-0509	19:51:47.468465	−05:09:43:96196	2.49	0.4	20190624	uid___A002_Xde0eb4_X176b
GY_Aql_b_06_TM1	extended	J1951-0509	19:51:47.468465	−05:09:43:96196	2.49	0.4	20190624	uid___A002_Xde0eb4_X1840
GY_Aql_c_06_TM1	extended	J1951-0509	19:51:47.468465	−05:09:43:96196	2.49	1.4	20190708	uid___A002_Xde8105_X9df1
GY_Aql_d_06_TM1	extended	J1951-0509	19:51:47.468465	−05:09:43:96196	2.49	1.4	20190708	uid___A002_Xde8105_X9f3e
GY_Aql_a_06_TM2	mid	J1951-0509	19:51:47.468465	−05:09:43:96196	2.49	0.5	20181113	uid___A002_Xd51939_X6300
GY_Aql_b_06_TM2	mid	J1951-0509	19:51:47.468465	−05:09:43:96196	2.49	1.7	20181112	uid___A002_Xd51939_X2e4
GY_Aql_b_06_TM2	mid	J1951-0509	19:51:47.468465	−05:09:43:96196	2.49	0.5	20181113	uid___A002_Xd51939_X6277
GY_Aql_c_06_TM2	mid	J1951-0509	19:51:47.468465	−05:09:43:96196	2.49	0.7	20181114	uid___A002_Xd52fc8_X876
GY_Aql_d_06_TM2	mid	J1951-0509	19:51:47.468465	−05:09:43:96196	2.49	0.5	20181113	uid___A002_Xd51939_X638d
GY_Aql_e_06_TM1	compact	J1951-0509	19:51:47.468465	−05:09:43:96196	2.49	1.4	20190303	uid___A002_Xd90607_X3948
GY_Aql_f_06_TM1	compact	J1951-0509	19:51:47.468465	−05:09:43:96196	2.49	1.0	20190113	uid___A002_Xd80784_X62d5
IRC+1001_a_06_TM1	extended	J0103+1526	01:03:26.001741	+15:26:24:66514	2.93	1.2	20190610	uid___A002_Xdd7b18_X33a6
IRC+1001_b_06_TM1	extended	J0103+1526	01:03:26.001741	+15:26:24:66514	2.93	1.2	20190610	uid___A002_Xdd7b18_X35f6
IRC+1001_c_06_TM1	extended	J0103+1526	01:03:26.001741	+15:26:24:66514	2.93	1.2	20190610	uid___A002_Xdd7b18_X373d
IRC+1001_c_06_TM1	extended	J0103+1526	01:03:26.001741	+15:26:24:66514	2.93	0.6	20190623	uid___A002_Xddf4b5_X7ead
IRC+1001_d_06_TM1	extended	J0103+1526	01:03:26.001741	+15:26:24:66514	2.93	1.2	20190610	uid___A002_Xdd7b18_X38ff
IRC+1001_d_06_TM1	extended	J0103+1526	01:03:26.001741	+15:26:24:66514	2.93	0.9	20190619	uid___A002_Xddc5da_X37ef
IRC+1001_a_06_TM2	mid	J0117+1418	01:17:25.203135	+14:18:12:42087	3.17	0.8	20190817	uid___A002_Xe02ab0_X3a67
IRC+1001_b_06_TM2	mid	J0117+1418	01:17:25.203135	+14:18:12:42087	3.17	0.8	20190817	uid___A002_Xe02ab0_X3939
IRC+1001_c_06_TM2	mid	J0117+1418	01:17:25.203135	+14:18:12:42087	3.17	0.8	20190817	uid___A002_Xe02ab0_X3ba1
IRC+1001_d_06_TM2	mid	J0117+1418	01:17:25.203135	+14:18:12:42087	3.17	0.8	20190817	uid___A002_Xe02ab0_X3cb4
IRC+1001_e_06_TM1	compact	J0117+1418	01:17:25.203192	+14:18:12:42000	3.17	1.3	20181225	uid___A002_Xd704f8_X2747c
IRC+1001_f_06_TM1	compact	J0117+1418	01:17:25.203192	+14:18:12:42000	3.17	2.4	20181226	uid___A002_Xd704f8_X2779f
IRC-1052_a_06_TM1	extended	J2018-0509	20:18:57.759947	−05:09:29:37341	2.39	0.4	20190624	uid___A002_Xde0eb4_X1b6b
IRC-1052_b_06_TM1	extended	J2018-0509	20:18:57.759947	−05:09:29:37341	2.39	0.9	20190619	uid___A002_Xddc5da_X36c1
IRC-1052_c_06_TM1	extended	J2018-0509	20:18:57.759947	−05:09:29:37341	2.39	1.3	20190625	uid___A002_Xde0eb4_X5b31
IRC-1052_c_06_TM1	extended	J2018-0509	20:18:57.759947	−05:09:29:37341	2.39	0.5	20190705	uid___A002_Xde63ab_X5a52
IRC-1052_d_06_TM1	extended	J2018-0509	20:18:57.759947	−05:09:29:37341	2.39	1.4	20190708	uid___A002_Xde8105_X9c5d
IRC-1052_a_06_TM2	mid	J2025-0735	20:25:40.660405	−07:35:52:68880	4.00	0.8	20190819	uid___A002_Xe03886_X52af
IRC-1052_b_06_TM2	mid	J2025-0735	20:25:40.660405	−07:35:52:68880	4.00	0.8	20190819	uid___A002_Xe03886_X516b
IRC-1052_c_06_TM2	mid	J2025-0735	20:25:40.660405	−07:35:52:68880	4.00	0.8	20190819	uid___A002_Xe03886_X53a9
IRC-1052_d_06_TM2	mid	J2025-0735	20:25:40.660405	−07:35:52:68880	4.00	2.0	20181103	uid___A002_Xd476cc_Xfbf
IRC-1052_d_06_TM2	mid	J2025-0735	20:25:40.660405	−07:35:52:68880	4.00	0.8	20181110	uid___A002_Xd50463_X48b
IRC-1052_e_06_TM1	compact	J2025-0735	20:25:40.660405	−07:35:52:68880	4.00	2.4	20181223	uid___A002_Xd704f8_X1367b
IRC-1052_f_06_TM1	compact	J2025-0735	20:25:40.660405	−07:35:52:68880	4.00	0.9	20190108	uid___A002_Xd7be9d_X72fd
KW_Sgr_a_06_TM1	extended	J1752-2956	17:52:33.10808	−29:56:44.9151	1.93	0.8	20190707	uid___A002_Xde8105_X18c0
KW_Sgr_b_06_TM1	extended	J1752-2956	17:52:33.10808	−29:56:44.9151	1.93	0.5	20190705	uid___A002_Xde63ab_X45ad
KW_Sgr_c_06_TM1	extended	J1752-2956	17:52:33.10808	−29:56:44.9151	1.93	2.3	20190710	uid___A002_Xde9c3e_X82f2
KW_Sgr_d_06_TM1	extended	J1752-2956	17:52:33.10808	−29:56:44.9151	1.93	0.8	20190707	uid___A002_Xde8105_X1f7b
KW_Sgr_d_06_TM1	extended	J1752-2956	17:52:33.10808	−29:56:44.9151	1.93	0.8	20190707	uid___A002_Xde8105_X241c

Table E.1. continued.

SB	Config	Phase-ref	Phase-ref R.A. (ICRS)	Phase-ref Dec. (ICRS)	Sep. (deg)	PWV (mm)	Date (YYYYMMDD)	ASDM
KW_Sgr_a_06_TM2	mid	J1744-3116	17:44:23.57820	−31:16:36.2947	3.65	0.7	20190827	uid___A002_Xe07f3e_Xfda8
KW_Sgr_a_06_TM2	mid	J1744-3116	17:44:23.57820	−31:16:36.2947	3.65	0.5	20210518	uid___A002_Xec0d12_Xfb6c
KW_Sgr_b_06_TM2	mid	J1744-3116	17:44:23.57820	−31:16:36.2947	3.65	0.7	20190831	uid___A002_Xe0be64_X5f1
KW_Sgr_c_06_TM2	mid	J1744-3116	17:44:23.57820	−31:16:36.2947	3.65	0.7	20190827	uid___A002_Xe07f3e_Xfff2
KW_Sgr_c_06_TM2	mid	J1744-3116	17:44:23.57820	−31:16:36.2947	3.65	2.3	20190921	uid___A002_Xe14043_Xcb1
KW_Sgr_c_06_TM2	mid	J1744-3116	17:44:23.57820	−31:16:36.2947	3.65	2.5	20190922	uid___A002_Xe14043_X13bd
KW_Sgr_d_06_TM2	mid	J1744-3116	17:44:23.57820	−31:16:36.2947	3.65	0.6	20181122	uid___A002_Xd58951_X7342
pi1_Gru_a_06_TM1	extended	J2230-4416	22:30:56.442979	−44:16:29:89110	2.21	0.5	20190623	uid___A002_Xddf4b5_X7acd
pi1_Gru_b_06_TM1	extended	J2230-4416	22:30:56.442979	−44:16:29:89110	2.21	0.5	20190623	uid___A002_Xddf4b5_X7971
pi1_Gru_c_06_TM1	extended	J2230-4416	22:30:56.442979	−44:16:29:89110	2.21	0.4	20190706	uid___A002_Xde63ab_Xb09d
pi1_Gru_d_06_TM1	extended	J2230-4416	22:30:56.442979	−44:16:29:89110	2.21	0.4	20190706	uid___A002_Xde63ab_Xb303
pi1_Gru_a_06_TM2	mid	J2230-4416	22:30:56.442979	−44:16:29:89110	2.21	1.2	20181028	uid___A002_Xd41a7b_Xc68
pi1_Gru_b_06_TM2	mid	J2230-4416	22:30:56.442979	−44:16:29:89110	2.21	1.2	20181028	uid___A002_Xd41a7b_Xb5a
pi1_Gru_c_06_TM2	mid	J2230-4416	22:30:56.442979	−44:16:29:89110	2.21	1.2	20181028	uid___A002_Xd41a7b_Xf86
pi1_Gru_d_06_TM2	mid	J2230-4416	22:30:56.442979	−44:16:29:89110	2.21	1.3	20181031	uid___A002_Xd42ec5_Xaf14
pi1_Gru_d_06_TM2	mid	J2230-4416	22:30:56.442979	−44:16:29:89110	2.21	1.3	20181031	uid___A002_Xd42ec5_Xb5fb
pi1_Gru_e_06_TM1*	compact	J2230-4416	22:30:56.442979	−44:16:29:89110	2.21	1.3	20181225	uid___A002_Xd704f8_X2660c
pi1_Gru_f_06_TM1*	compact	J2230-4416	22:30:56.442979	−44:16:29:89110	2.21	0.6	20190319	uid___A002_Xd99ff3_X1133d
RW_Sco_a_06_TM1	extended	J1717-3342	17:17:36.029447	−33:42:08:82768	0.63	0.5	20190705	uid___A002_Xde63ab_X85f2
RW_Sco_b_06_TM1	extended	J1717-3342	17:17:36.029447	−33:42:08:82768	0.63	0.5	20190705	uid___A002_Xde63ab_X4188
RW_Sco_c_06_TM1	extended	J1717-3342	17:17:36.029447	−33:42:08:82768	0.63	0.5	20190705	uid___A002_Xde63ab_X435f
RW_Sco_d_06_TM1	extended	J1717-3342	17:17:36.029447	−33:42:08:82768	0.63	0.4	20190706	uid___A002_Xde63ab_X8915
RW_Sco_a_06_TM2	mid	J1717-3342	17:17:36.029447	−33:42:08:82768	0.63	0.7	20190830	uid___A002_Xe0be64_X574
RW_Sco_b_06_TM2	mid	J1717-3342	17:17:36.029447	−33:42:08:82768	0.63	0.7	20190830	uid___A002_Xe0be64_X4f7
RW_Sco_c_06_TM2	mid	J1717-3342	17:17:36.029447	−33:42:08:82768	0.63	0.7	20190831	uid___A002_Xe0be64_X652
RW_Sco_d_06_TM2	mid	J1717-3342	17:17:36.029447	−33:42:08:82768	0.63	0.6	20181122	uid___A002_Xd58951_X635f
RW_Sco_e_06_TM1	compact	J1717-3342	17:17:36.029447	−33:42:08:82768	0.63	2.3	20190106	uid___A002_Xd7aa27_X6000
RW_Sco_e_06_TM1	compact	J1717-3342	17:17:36.029447	−33:42:08:82768	0.63	0.9	20190108	uid___A002_Xd7be9d_X63db
RW_Sco_f_06_TM1	compact	J1717-3342	17:17:36.029447	−33:42:08:82768	0.63	0.9	20190108	uid___A002_Xd7be9d_X5e86
R_Aql_a_06_TM1	extended	J1905+0952	19:05:39.898975	+09:52:08:40793	1.65	0.5	20190705	uid___A002_Xde63ab_X4aee
R_Aql_b_06_TM1	extended	J1905+0952	19:05:39.898975	+09:52:08:40793	1.65	0.5	20190705	uid___A002_Xde63ab_X4ced
R_Aql_c_06_TM1	extended	J1905+0952	19:05:39.898975	+09:52:08:40793	1.65	0.4	20190706	uid___A002_Xde63ab_Xa269
R_Aql_d_06_TM1	extended	J1905+0952	19:05:39.898975	+09:52:08:40793	1.65	0.4	20190706	uid___A002_Xde63ab_Xa59d
R_Aql_a_06_TM2	mid	J1907+0127	19:07:11.996165	+01:27:08:96151	6.78	1.3	20181118	uid___A002_Xd557dd_X8b13
R_Aql_a_06_TM2	mid	J1907+0127	19:07:11.996165	+01:27:08:96151	6.78	1.6	20181121	uid___A002_Xd58951_X2aa
R_Aql_b_06_TM2	mid	J1907+0127	19:07:11.996165	+01:27:08:96151	6.78	1.3	20181118	uid___A002_Xd557dd_X8c87
R_Aql_b_06_TM2	mid	J1907+0127	19:07:11.996165	+01:27:08:96151	6.78	1.6	20181121	uid___A002_Xd58951_X1bd
R_Aql_c_06_TM2	mid	J1907+0127	19:07:11.996165	+01:27:08:96151	6.78	1.3	20181118	uid___A002_Xd557dd_X8d4b
R_Aql_c_06_TM2	mid	J1907+0127	19:07:11.996165	+01:27:08:96151	6.78	0.6	20181122	uid___A002_Xd58951_X6b1c
R_Aql_d_06_TM2	mid	J1907+0127	19:07:11.996165	+01:27:08:96151	6.78	1.3	20181118	uid___A002_Xd557dd_X8e44
R_Aql_d_06_TM2	mid	J1907+0127	19:07:11.996165	+01:27:08:96151	6.78	1.9	20181119	uid___A002_Xd57414_X5e6
R_Aql_e_06_TM1	compact	J1907+0127	19:07:11.996165	+01:27:08:96151	6.78	2.4	20181223	uid___A002_Xd704f8_X12e26
R_Aql_f_06_TM1	compact	J1907+0127	19:07:11.996165	+01:27:08:96151	6.78	2.4	20181223	uid___A002_Xd704f8_X134aa
R_Hya_a_06_TM1	extended	J1339-2401	13:39:01.746378	−24:01:14:00628	2.26	1.4	20190711	uid___A002_Xdeb725_X184
R_Hya_b_06_TM1	extended	J1339-2401	13:39:01.746378	−24:01:14:00628	2.26	0.9	20190709	uid___A002_Xde9c3e_X627b
R_Hya_c_06_TM1	extended	J1339-2401	13:39:01.746378	−24:01:14:00628	2.26	1.4	20190711	uid___A002_Xdeb725_X8c1
R_Hya_c_06_TM1	extended	J1339-2401	13:39:01.746378	−24:01:14:00628	2.26	1.7	20190712	uid___A002_Xdeb725_X5595
R_Hya_d_06_TM1	extended	J1339-2401	13:39:01.746378	−24:01:14:00628	2.26	0.9	20190709	uid___A002_Xde9c3e_X66a0
R_Hya_d_06_TM1	extended	J1339-2401	13:39:01.746378	−24:01:14:00628	2.26	2.3	20190710	uid___A002_Xde9c3e_X6e99
R_Hya_d_06_TM1	extended	J1339-2401	13:39:01.746378	−24:01:14:00628	2.26	1.7	20190712	uid___A002_Xdeb725_X943a
R_Hya_a_06_TM2	mid	J1246-2547	12:46:46.802033	−25:47:49:28899	10.08	0.4	20181027	uid___A002_Xd40be0_X86e4
R_Hya_b_06_TM2	mid	J1246-2547	12:46:46.802033	−25:47:49:28899	10.08	0.6	20181025	uid___A002_Xd3e89f_X83c3
R_Hya_b_06_TM2	mid	J1246-2547	12:46:46.802033	−25:47:49:28899	10.08	1.6	20181104	uid___A002_Xd490e7_X7316
R_Hya_c_06_TM2	mid	J1246-2547	12:46:46.802033	−25:47:49:28899	10.08	0.6	20181025	uid___A002_Xd3e89f_X638f
R_Hya_d_06_TM2	mid	J1246-2547	12:46:46.802033	−25:47:49:28899	10.08	0.6	20181025	uid___A002_Xd3e89f_X6861
R_Hya_d_06_TM2	mid	J1246-2547	12:46:46.802033	−25:47:49:28899	10.08	0.6	20181025	uid___A002_Xd3e89f_X74f9
R_Hya_e_06_TM1	compact	J1246-2547	12:46:46.802033	−25:47:49:28899	10.08	1.7	20181227	uid___A002_Xd74c3f_X3c9f
R_Hya_f_06_TM1	compact	J1246-2547	12:46:46.802033	−25:47:49:28899	10.08	2.3	20190106	uid___A002_Xd7aa27_X5bce
SV_Aqr_a_06_TM1	extended	J2323-0617	23:23:39.113750	−06:17:59:23920	4.52	0.9	20190605	uid___A002_Xdd3de2_X3ea4
SV_Aqr_b_06_TM1	extended	J2323-0617	23:23:39.113750	−06:17:59:23920	4.52	1.0	20190612	uid___A002_Xdd7b18_Xa6b1
SV_Aqr_c_06_TM1	extended	J2323-0617	23:23:39.113750	−06:17:59:23920	4.52	1.0	20190612	uid___A002_Xdd7b18_Xaa94
SV_Aqr_d_06_TM1	extended	J2323-0617	23:23:39.113750	−06:17:59:23920	4.52	0.8	20190707	uid___A002_Xde8105_X3afd
SV_Aqr_a_06_TM2	mid	J2323-0617	23:23:39.113750	−06:17:59:23920	4.52	0.8	20190817	uid___A002_Xe02ab0_X3751
SV_Aqr_b_06_TM2	mid	J2323-0617	23:23:39.113750	−06:17:59:23920	4.52	0.8	20190817	uid___A002_Xe02ab0_X361b
SV_Aqr_c_06_TM2	mid	J2323-0617	23:23:39.113750	−06:17:59:23920	4.52	0.8	20190817	uid___A002_Xe02ab0_X386c
SV_Aqr_d_06_TM2	mid	J2345-1555	23:45:12.462316	−15:55:07:83452	7.47	0.8	20181021	uid___A002_Xd395f6_Xa686
SV_Aqr_e_06_TM1	compact	J2345-1555	23:45:12.462316	−15:55:07:83452	7.47	1.7	20181227	uid___A002_Xd74c3f_X8693

Table E.1. continued.

SB	Config	Phase-ref	Phase-ref R.A. (ICRS)	Phase-ref Dec. (ICRS)	Sep. (deg)	PWV (mm)	Date (YYYYMMDD)	ASDM
SV_Aqr_e_06_TM1	compact	J2345-1555	23:45:12.462316	−15:55:07:83452	7.47	3.6	20190118	uid___A002_Xd845af_Xe8b1
SV_Aqr_f_06_TM1	compact	J2345-1555	23:45:12.462316	−15:55:07:83452	7.47	1.1	20190312	uid___A002_Xd9668b_X856d
S_Pav_a_06_TM1	extended	J1946-5812	19:46:29.827711	−58:12:52:41679	1.50	0.5	20190705	uid___A002_Xde63ab_X4f83
S_Pav_b_06_TM1	extended	J1946-5812	19:46:29.827711	−58:12:52:41679	1.50	0.5	20190705	uid___A002_Xde63ab_X52fd
S_Pav_c_06_TM1	extended	J1946-5812	19:46:29.827711	−58:12:52:41679	1.50	0.8	20190707	uid___A002_Xde8105_X299d
S_Pav_d_06_TM1	extended	J1946-5812	19:46:29.827711	−58:12:52:41679	1.50	0.8	20190707	uid___A002_Xde8105_X2db8
S_Pav_a_06_TM2	mid	J1829-5813	18:29:12.402359	−58:13:55:16190	11.16	2.1	20181105	uid___A002_Xd490e7_Xaf43
S_Pav_a_06_TM2	mid	J1829-5813	18:29:12.402359	−58:13:55:16190	11.16	1.4	20181115	uid___A002_Xd5371c_X37eb
S_Pav_b_06_TM2	mid	J1829-5813	18:29:12.402359	−58:13:55:16190	11.16	2.1	20181105	uid___A002_Xd490e7_Xad8e
S_Pav_b_06_TM2	mid	J1829-5813	18:29:12.402359	−58:13:55:16190	11.16	1.5	20181120	uid___A002_Xd57a13_X590f
S_Pav_c_06_TM2	mid	J1829-5813	18:29:12.402359	−58:13:55:16190	11.16	1.4	20181115	uid___A002_Xd5371c_X3c8c
S_Pav_d_06_TM2	mid	J1829-5813	18:29:12.402359	−58:13:55:16190	11.16	1.4	20181029	uid___A002_Xd42ec5_Xe10
S_Pav_d_06_TM2	mid	J1829-5813	18:29:12.402359	−58:13:55:16190	11.16	1.3	20181031	uid___A002_Xd44a99_X76d
S_Pav_e_06_TM1	compact	J1829-5813	18:29:12.402359	−58:13:55:16190	11.16	2.3	20190106	uid___A002_Xd7aa27_X79c7
S_Pav_e_06_TM1	compact	J1945-5520	19:45:24.228664	−55:20:48:83907	4.07	1.4	20190303	uid___A002_Xd90607_X441a
S_Pav_f_06_TM1	compact	J1829-5813	18:29:12.402359	−58:13:55:16190	11.16	2.4	20181223	uid___A002_Xd704f8_X13873
S_Pav_f_06_TM1	compact	J2056-4714	20:56:16.359815	−47:14:47:62776	14.97	1.8	20190122	uid___A002_Xd88143_X5349
T_Mic_a_06_TM1	extended	J2025-2845	20:25:53.612837	−28:45:48:69762	0.67	0.8	20190707	uid___A002_Xde8105_X314c
T_Mic_b_06_TM1	extended	J2025-2845	20:25:53.612837	−28:45:48:69762	0.67	0.8	20190707	uid___A002_Xde8105_X33c2
T_Mic_c_06_TM1	extended	J2025-2845	20:25:53.612837	−28:45:48:69762	0.67	0.8	20190707	uid___A002_Xde8105_X3691
T_Mic_d_06_TM1	extended	J2025-2845	20:25:53.612837	−28:45:48:69762	0.67	0.8	20190707	uid___A002_Xde8105_X385b
T_Mic_a_06_TM2	mid	J2056-3208	20:56:25.070236	−32:08:47:80088	7.28	1.3	20181101	uid___A002_Xd44a99_Xcb6
T_Mic_a_06_TM2	mid	J2056-3208	20:56:25.070236	−32:08:47:80088	7.28	0.5	20181113	uid___A002_Xd51939_X61ca
T_Mic_b_06_TM2	mid	J2056-3208	20:56:25.070236	−32:08:47:80088	7.28	1.3	20181031	uid___A002_Xd44a99_Xb3d
T_Mic_b_06_TM2	mid	J2056-3208	20:56:25.070236	−32:08:47:80088	7.28	1.4	20181115	uid___A002_Xd5371c_X39dd
T_Mic_c_06_TM2	mid	J2056-3208	20:56:25.070236	−32:08:47:80088	7.28	1.3	20181101	uid___A002_Xd44a99_Xf42
T_Mic_c_06_TM2	mid	J2056-3208	20:56:25.070236	−32:08:47:80088	7.28	1.9	20181119	uid___A002_Xd57414_X3ef
T_Mic_d_06_TM2	mid	J2056-3208	20:56:25.070236	−32:08:47:80088	7.28	1.3	20181101	uid___A002_Xd44a99_X1606
T_Mic_d_06_TM2	mid	J2056-3208	20:56:25.070236	−32:08:47:80088	7.28	1.1	20181102	uid___A002_Xd44a99_X104f1
T_Mic_e_06_TM1*	compact	J2056-3208	20:56:25.070236	−32:08:47:80088	7.28	1.3	20181225	uid___A002_Xd704f8_X2739a
T_Mic_e_06_TM1*	compact	J2056-3208	20:56:25.070236	−32:08:47:80088	7.28	2.3	20190106	uid___A002_Xd7aa27_X7f54
T_Mic_f_06_TM1*	compact	J2024-3253	20:24:35.577000	−32:53:35:91200	4.69	1.8	20190305	uid___A002_Xd90607_X11b5d
U_Del_a_06_TM1	extended	J2051+1743	20:51:35.582938	+17:43:36:90030	1.50	0.5	20190705	uid___A002_Xde63ab_X55b7
U_Del_b_06_TM1	extended	J2051+1743	20:51:35.582938	+17:43:36:90030	1.50	0.9	20190627	uid___A002_Xde2e20_Xaaa
U_Del_c_06_TM1	extended	J2051+1743	20:51:35.582938	+17:43:36:90030	1.50	0.4	20190706	uid___A002_Xde63ab_Xa8f6
U_Del_d_06_TM1	extended	J2051+1743	20:51:35.582938	+17:43:36:90030	1.50	0.4	20190706	uid___A002_Xde63ab_Xad2f
U_Del_a_06_TM2	mid	J2051+1743	20:51:35.582938	+17:43:36:90030	1.50	1.6	20181104	uid___A002_Xd490e7_Xa294
U_Del_b_06_TM2	mid	J2051+1743	20:51:35.582938	+17:43:36:90030	1.50	1.1	20181102	uid___A002_Xd44a99_X1086a
U_Del_b_06_TM2	mid	J2051+1743	20:51:35.582938	+17:43:36:90030	1.50	0.8	20181110	uid___A002_Xd4f832_X2524
U_Del_c_06_TM2	mid	J2051+1743	20:51:35.582938	+17:43:36:90030	1.50	1.3	20181031	uid___A002_Xd44a99_X8ee
U_Del_d_06_TM2	mid	J2051+1743	20:51:35.582938	+17:43:36:90030	1.50	1.4	20181030	uid___A002_Xd42ec5_Xffd
U_Del_d_06_TM2	mid	J2051+1743	20:51:35.582938	+17:43:36:90030	1.50	1.4	20181030	uid___A002_Xd42ec5_Xad56
U_Del_e_06_TM1	compact	J2051+1743	20:51:35.582938	+17:43:36:90030	1.50	1.7	20190303	uid___A002_Xd90607_X447c
U_Del_e_06_TM1	compact	J2051+1743	20:51:35.582938	+17:43:36:90030	1.50	0.4	20190326	uid___A002_Xda1250_X5785
U_Del_f_06_TM1	compact	J2051+1743	20:51:35.582938	+17:43:36:90030	1.50	3.2	20190115	uid___A002_Xd81670_Xfee1
U_Del_f_06_TM1	compact	J2051+1743	20:51:35.582938	+17:43:36:90030	1.50	1.4	20190303	uid___A002_Xd90607_X417e
U_Her_a_06_TM1	extended	J1619+2247	16:19:14.824597	+22:47:47:85095	4.19	0.4	20190624	uid___A002_Xde0eb4_Xb77
U_Her_b_06_TM1	extended	J1619+2247	16:19:14.824597	+22:47:47:85095	4.19	1.2	20190622	uid___A002_Xddf4b5_X1219
U_Her_c_06_TM1	extended	J1619+2247	16:19:14.824597	+22:47:47:85095	4.19	0.4	20190624	uid___A002_Xde0eb4_X9a1
U_Her_c_06_TM1	extended	J1619+2247	16:19:14.824597	+22:47:47:85095	4.19	0.6	20190704	uid___A002_Xde63ab_X3d7d
U_Her_d_06_TM1	extended	J1619+2247	16:19:14.824597	+22:47:47:85095	4.19	0.4	20190706	uid___A002_Xde63ab_X8c82
U_Her_a_06_TM2	mid	J1619+2247	16:19:14.824597	+22:47:47:85095	4.19	0.6	20181122	uid___A002_Xd58951_X64f9
U_Her_b_06_TM2	mid	J1619+2247	16:19:14.824597	+22:47:47:85095	4.19	0.6	20181122	uid___A002_Xd58951_X66a6
U_Her_c_06_TM2	mid	J1619+2247	16:19:14.824597	+22:47:47:85095	4.19	0.6	20181122	uid___A002_Xd58951_X684d
U_Her_d_06_TM2	mid	J1619+2247	16:19:14.824597	+22:47:47:85095	4.19	0.5	20181014	uid___A002_Xd341ff_X7fb0
U_Her_d_06_TM2	mid	J1619+2247	16:19:14.824597	+22:47:47:85095	4.19	1.2	20190824	uid___A002_Xe07f3e_X1119
U_Her_e_06_TM1	compact	J1619+2247	16:19:14.824597	+22:47:47:85095	4.19	2.3	20190106	uid___A002_Xd7aa27_X5dfc
U_Her_e_06_TM1	compact	J1619+2247	16:19:14.824597	+22:47:47:85095	4.19	0.9	20190108	uid___A002_Xd7be9d_X5e35
U_Her_f_06_TM1	compact	J1606+1814	16:06:16.027796	+18:14:59:81991	4.67	2.3	20190106	uid___A002_Xd7aa27_X6818
U_Her_f_06_TM1	compact	J1606+1814	16:06:16.027796	+18:14:59:81991	4.67	1.4	20190303	uid___A002_Xd90607_X2701
VX_Sgr_a_06_TM1	extended	J1755-2232	17:55:26.284539	−22:32:10:61556	2.94	0.9	20190709	uid___A002_Xde9c3e_X2897
VX_Sgr_b_06_TM1	extended	J1755-2232	17:55:26.284539	−22:32:10:61556	2.94	0.5	20190705	uid___A002_Xde63ab_X5869
VX_Sgr_c_06_TM1	extended	J1755-2232	17:55:26.284539	−22:32:10:61556	2.94	0.9	20190709	uid___A002_Xde9c3e_X2cd8
VX_Sgr_d_06_TM1	extended	J1755-2232	17:55:26.284539	−22:32:10:61556	2.94	0.9	20190709	uid___A002_Xde9c3e_X3204
VX_Sgr_a_06_TM2	mid	J1755-2232	17:55:26.284539	−22:32:10:61556	2.94	0.8	20190825	uid___A002_Xe07f3e_X37fd
VX_Sgr_b_06_TM2	mid	J1755-2232	17:55:26.284539	−22:32:10:61556	2.94	0.4	20190820	uid___A002_Xe03886_Xaf4e
VX_Sgr_c_06_TM2	mid	J1755-2232	17:55:26.284539	−22:32:10:61556	2.94	0.8	20190825	uid___A002_Xe07f3e_X35aa

Table E.1. continued.

SB	Config	Phase-ref	Phase-ref R.A. (ICRS)	Phase-ref Dec. (ICRS)	Sep. (deg)	PWV (mm)	Date (YYYYMMDD)	ASDM
VX_Sgr_d_06_TM2	mid	J1832-2039	18:32:11.046488	−20:39:48:20328	5.82	0.6	20181122	uid___A002_Xd58951_X61a1
VX_Sgr_e_06_TM1*	compact	J1832-2039	18:32:11.046488	−20:39:48:20328	5.82	0.9	20190108	uid___A002_Xd7be9d_X5fb9
VX_Sgr_f_06_TM1*	compact	J1832-2039	18:32:11.046488	−20:39:48:20328	5.82	1.4	20190303	uid___A002_Xd90607_X2921
V_PsA_a_06_TM1	extended	J2258-2758	22:58:05.962884	−27:58:21:25677	1.75	0.4	20190624	uid___A002_Xde0eb4_X190d
V_PsA_b_06_TM1	extended	J2258-2758	22:58:05.962884	−27:58:21:25677	1.75	0.5	20190623	uid___A002_Xddf4b5_X7c50
V_PsA_c_06_TM1	extended	J2258-2758	22:58:05.962884	−27:58:21:25677	1.75	0.4	20190706	uid___A002_Xde63ab_Xb469
V_PsA_d_06_TM1	extended	J2248-3235	22:48:38.685742	−32:35:52:18816	3.31	0.8	20190707	uid___A002_Xde8105_X4234
V_PsA_a_06_TM2	mid	J2258-2758	22:58:05.962884	−27:58:21:25677	1.75	0.6	20181026	uid___A002_Xd3e89f_Xb473
V_PsA_b_06_TM2	mid	J2258-2758	22:58:05.962884	−27:58:21:25677	1.75	0.6	20181025	uid___A002_Xd3e89f_X1af0
V_PsA_c_06_TM2	mid	J2258-2758	22:58:05.962884	−27:58:21:25677	1.75	1.4	20181030	uid___A002_Xd42ec5_X258a
V_PsA_d_06_TM2	mid	J2258-2758	22:58:05.962884	−27:58:21:25677	1.75	0.4	20181027	uid___A002_Xd40be0_X2f01
V_PsA_e_06_TM1	compact	J2258-2758	22:58:05.962884	−27:58:21:25677	1.75	1.7	20181227	uid___A002_Xd74c3f_X873c
V_PsA_e_06_TM1	compact	J2248-3235	22:48:38.685742	−32:35:52:18816	3.31	0.8	20190320	uid___A002_Xd99ff3_X1927f
V_PsA_f_06_TM1	compact	J2248-3235	22:48:38.685742	−32:35:52:18816	3.31	0.8	20190320	uid___A002_Xd99ff3_X19307
W_Aql_a_06_TM1	extended	J1912-0804	19:12:07.128819	−08:04:21:90218	1.31	0.4	20190624	uid___A002_Xde0eb4_X12a4
W_Aql_b_06_TM1	extended	J1912-0804	19:12:07.128819	−08:04:21:90218	1.31	0.4	20190624	uid___A002_Xde0eb4_X152c
W_Aql_c_06_TM1	extended	J1912-0804	19:12:07.128819	−08:04:21:90218	1.31	1.4	20190708	uid___A002_Xde8105_X8695
W_Aql_d_06_TM1	extended	J1912-0804	19:12:07.128819	−08:04:21:90218	1.31	1.4	20190708	uid___A002_Xde8105_X9638
W_Aql_a_06_TM2	mid	J1907+0127	19:07:11.996165	+01:27:08:96151	8.74	0.9	20181116	uid___A002_Xd54982_X9ce
W_Aql_a_06_TM2	mid	J1907+0127	19:07:11.996165	+01:27:08:96151	8.74	1.4	20181117	uid___A002_Xd557dd_X4e9
W_Aql_b_06_TM2	mid	J1951-0509	19:51:47.468465	−05:09:43:96196	9.24	0.9	20181116	uid___A002_Xd54982_X945
W_Aql_b_06_TM2	mid	J1907+0127	19:07:11.996165	+01:27:08:96151	8.74	1.4	20181117	uid___A002_Xd557dd_X351
W_Aql_c_06_TM2	mid	J1951-0509	19:51:47.468465	−05:09:43:96196	9.24	1.4	20181117	uid___A002_Xd557dd_X70b
W_Aql_c_06_TM2	mid	J1951-0509	19:51:47.468465	−05:09:43:96196	9.24	1.3	20181118	uid___A002_Xd557dd_X8f04
W_Aql_d_06_TM2	mid	J1951-0509	19:51:47.468465	−05:09:43:96196	9.24	1.3	20181118	uid___A002_Xd557dd_X9057
W_Aql_d_06_TM2	mid	J1951-0509	19:51:47.468465	−05:09:43:96196	9.24	1.5	20181120	uid___A002_Xd57a13_X586a
W_Aql_e_06_TM1	compact	J1907+0127	19:07:11.996165	+01:27:08:96151	8.74	2.4	20181223	uid___A002_Xd704f8_X1328c
W_Aql_f_06_TM1	compact	J1951-0509	19:51:47.468465	−05:09:43:96196	9.24	0.9	20190108	uid___A002_Xd7be9d_X61a3

Notes. 'SB' refers to the Scheduling Block, 'Config' to the array configuration, 'Phase-ref' to the phase reference source, 'R.A.' and 'Dec.' to the right ascension and declination, 'Sep.' is the angular separation between the target and the phase-reference source, 'PWV' is the precipitable water vapour at the Date of the observations, and 'ASDM' is the ALMA archival name. The PWV values are for the start of each night and vary (usually by only 10% or less) during observations. In Col. 8, 'Date' refers to the end date of the observation.* Owing to initial inconsistent capitalisation, SG marked * were originally named as follows: pi1_gru_a_06_TM1, pi1_gru_b_06_TM1, vx_sgr_a_06_TM1, vx_sgr_b_06_TM1, T_mic_a_06_TM1, T_mic_b_06_TM1. The SG were subsequently renamed as indicated below in our data products.

Table E.2. Continuum image properties.

Star	Config.	b_{maj}	b_{min}	b_{pa}	Imsize	MRS	Cont.	σ_{rms}^{cont}	Peak RA	Peak Dec.	σ_{RA}^{cont}	σ_{Dec}^{cont}	Peak^{cont}	σ_{Peak}^{cont}	Mid Freq.
		(arcsec)		(deg)	(arcsec)		(GHz)	(mJy)	(ICRS)	(ICRS)	(mas)		(mJy/bm)		(GHz)
AH_Sco	extended	0.023	0.023	70	1.0	0.5	18.61	0.011	17:11:17.01591	−32:19:30.7643	0.1	0.1	7.48	0.04	241.78
AH_Sco	mid	0.159	0.100	−79	4.0	1.7	17.08	0.014	17:11:17.01635	−32:19:30.7669	1.2	2.6	6.48	0.13	241.78
GY_Aql	extended	0.025	0.022	−56	1.0	0.4	23.81	0.023	19:50:06.31478	−07:36:52.1890	0.1	0.1	9.00	0.04	241.75
GY_Aql	mid	0.324	0.247	−70	24.0	4.0	18.03	0.026	19:50:06.31432	−07:36:52.2006	0.7	1.0	8.53	0.06	241.75
GY_Aql	compact	1.220	0.897	64	24.0	9.5	8.69	0.040	19:50:06.31672	−07:36:52.3182	7.0	9.5	9.45	0.16	238.44
IRC+10011	extended	0.027	0.019	31	1.0	0.4	23.55	0.020	01:06:25.98833	+12:35:52.8487	0.1	0.1	11.19	0.09	241.77
IRC+10011	mid	0.112	0.100	38	6.0	1.6	18.49	0.033	01:06:25.98838	+12:35:52.8565	0.6	0.6	11.70	0.14	241.77
IRC+10011	compact	0.722	0.686	−59	24.0	7.4	8.53	0.051	01:06:25.98542	+12:35:52.8578	2.2	2.2	12.44	0.09	238.43
IRC-10529	extended	0.026	0.023	−55	1.0	0.4	23.63	0.028	20:10:27.87133	−06:16:13.7402	0.1	0.2	7.31	0.09	241.79
IRC-10529	mid	0.146	0.113	−63	4.0	2.0	15.33	0.027	20:10:27.87259	−06:16:13.7475	0.8	1.2	7.26	0.11	241.76
IRC-10529	compact	0.788	0.627	76	24.0	8.9	6.97	0.052	20:10:27.86978	−06:16:13.7251	4.4	6.3	6.25	0.10	238.48
KW_Sgr	extended	0.022	0.020	−66	0.8	0.5	24.31	0.008	17:52:00.72819	−28:01:20.5715	0.1	0.1	2.90	0.01	241.77
KW_Sgr	mid	0.157	0.098	−75	4.0	2.0	22.42	0.019	17:52:00.72839	−28:01:20.5846	0.4	1.0	2.63	0.03	241.74
pi1_Gru	extended	0.019	0.019	60	0.6	0.4	24.21	0.015	22:22:44.26959	−45:56:53.0065	0.2	0.2	17.79	0.04	241.79
pi1_Gru	mid	0.248	0.235	30	8.0	3.9	20.49	0.034	22:22:44.26654	−45:56:52.9986	0.2	0.2	32.33	0.08	241.79
pi1_Gru	compact	0.866	0.774	−86	24.0	9.3	10.36	0.036	22:22:44.26861	−45:56:52.9890	0.4	0.4	31.29	0.04	238.45
RW_Sco	extended	0.024	0.020	−70	1.0	0.4	24.53	0.020	17:14:51.68672	−33:25:54.5437	0.2	0.2	5.84	0.10	241.83
RW_Sco	mid	0.147	0.120	−86	4.0	1.9	6.75	0.040	17:14:51.68671	−33:25:54.5440	0.4	0.6	5.26	0.04	242.02
RW_Sco	compact	0.928	0.701	86	24.0	9.0	10.30	0.034	17:14:51.68927	−33:25:54.5042	2.5	4.2	3.37	0.03	238.52
R_Aql	extended	0.024	0.022	−13	1.0	0.4	22.63	0.008	19:06:22.25672	+08:13:46.6778	0.1	0.1	17.02	0.03	241.74
R_Aql	mid	0.306	0.238	−54	8.0	3.8	20.31	0.030	19:06:22.25564	+08:13:46.7063	0.8	1.0	18.04	0.13	241.74
R_Aql	compact	0.764	0.648	83	24.0	7.7	10.25	0.042	19:06:22.26051	+08:13:46.6697	1.5	2.1	15.91	0.09	238.43
R_Hya	extended	0.034	0.025	67	1.0	0.6	23.55	0.057	13:29:42.70211	−23:16:52.5146	0.3	0.4	41.86	0.27	241.78
R_Hya	mid	0.256	0.223	70	8.0	3.5	19.02	0.028	13:29:42.70465	−23:16:52.5318	0.2	0.2	54.44	0.10	241.82
R_Hya	compact	0.830	0.600	79	24.0	8.7	10.09	0.051	13:29:42.70448	−23:16:52.5536	0.2	0.2	65.55	0.06	238.47
SV_Aqr	extended	0.022	0.021	43	1.0	0.4	28.96	0.009	23:22:45.40025	−10:49:00.1874	0.2	0.2	1.43	0.02	241.78
SV_Aqr	mid	0.124	0.104	−75	8.0	1.6	27.55	0.023	23:22:45.39878	−10:49:00.1789	0.6	0.7	2.17	0.03	241.77
SV_Aqr	compact	0.886	0.747	74	24.0	9.8	10.92	0.038	23:22:45.39676	−10:49:00.2442	7.9	9.3	1.35	0.03	238.46
S_Pav	extended	0.025	0.020	−13	1.0	0.4	22.35	0.010	19:55:14.00546	−59:11:45.1943	0.1	0.1	21.75	0.04	241.79
S_Pav	mid	0.304	0.234	56	8.0	3.3	20.20	0.022	19:55:14.00227	−59:11:45.1462	0.2	0.2	31.04	0.04	241.89
S_Pav	compact	1.026	0.983	−56	24.0	8.7	10.22	0.051	19:55:13.99589	−59:11:45.0735	1.7	1.8	27.24	0.11	238.48
T_Mic	extended	0.024	0.021	−73	1.0	0.4	24.94	0.013	20:27:55.17974	−28:15:39.5529	0.1	0.1	23.00	0.07	241.75
T_Mic	mid	0.268	0.225	−89	8.0	4.0	19.36	0.025	20:27:55.17968	−28:15:39.5631	0.1	0.1	30.14	0.03	241.75
T_Mic	compact	1.047	0.730	−79	24.0	9.3	10.99	0.059	20:27:55.18152	−28:15:39.4732	0.8	1.6	26.39	0.08	238.45
U_Del	extended	0.030	0.021	−25	1.0	0.4	25.44	0.010	20:45:28.25002	+18:05:23.9761	0.0	0.0	6.49	0.02	241.78
U_Del	mid	0.316	0.235	−33	8.0	3.3	14.84	0.028	20:45:28.24967	+18:05:23.9930	1.4	1.2	7.25	0.06	241.68
U_Del	compact	1.165	1.013	33	24.0	9.0	11.00	0.048	20:45:28.25138	+18:05:23.9726	4.6	4.0	7.36	0.06	238.44
U_Her	extended	0.024	0.018	8	0.6	0.4	23.33	0.013	16:25:47.45136	+18:53:32.6663	0.1	0.1	11.60	0.08	241.79
U_Her	mid	0.267	0.195	−33	8.0	2.2	16.83	0.048	16:25:47.45134	+18:53:32.7012	2.3	1.9	14.77	0.18	241.79
U_Her	compact	0.997	0.843	26	24.0	9.7	9.75	0.054	16:25:47.45145	+18:53:32.6428	1.2	1.0	17.29	0.05	238.48
VX_Sgr	extended	0.028	0.020	89	0.6	0.4	18.16	0.019	18:08:04.04604	−22:13:26.6209	0.1	0.1	14.58	0.08	241.77
VX_Sgr	mid	0.162	0.095	−75	4.0	1.5	16.11	0.030	18:08:04.04466	−22:13:26.6121	0.2	0.4	16.34	0.08	241.77
VX_Sgr	compact	1.127	0.809	79	36.0	10.0	8.05	0.039	18:08:04.04934	−22:13:26.6426	1.6	2.8	15.96	0.08	238.46
V_PsA	extended	0.023	0.021	−77	1.0	0.4	24.78	0.009	22:55:19.72280	−29:36:45.0384	0.1	0.1	8.93	0.03	241.78
V_PsA	mid	0.283	0.229	85	8.0	4.0	20.99	0.020	22:55:19.72003	−29:36:45.0569	0.2	0.4	9.35	0.03	241.67
V_PsA	compact	0.995	0.753	87	24.0	9.0	11.28	0.030	22:55:19.72043	−29:36:45.0559	1.4	2.4	8.67	0.04	238.45
W_Aql	extended	0.024	0.021	−47	1.0	0.4	24.22	0.005	19:15:23.37809	−07:02:50.3306	0.1	0.1	6.53	0.04	241.80
W_Aql	mid	0.351	0.223	−68	8.0	3.9	18.75	0.030	19:15:23.37954	−07:02:50.3165	2.4	4.0	5.63	0.12	241.69
W_Aql	compact	0.920	0.667	76	24.0	8.9	6.61	0.056	19:15:23.38051	−07:02:50.3096	5.6	8.7	7.62	0.14	238.49

Notes. These are taken from the image after the optimum number of rounds of self-calibration. Config. is the array combination, determining b_{maj}, b_{min} and b_{PA}, the major and minor axis and the position angle of the synthesized beam, respectively. Imsize is the image size and MRS is the maximum recoverable angular scale. Cont. is the total line-free bandwidth, spread over all tunings. The continuum σ_{rms}^{cont} noise is measured in a region of ∼10% the total image area clear of the emission, in the images without primary beam correction. Peak RA and Peak Dec. are the position of a 2D Gaussian component fitted to the peak, fitting uncertainties σ_{RA}^{cont}, σ_{Dec}^{cont}. Peak^{cont} and σ_{Peak}^{cont} are the peak flux density and stochastic uncertainty, and Mid Freq is the approximate mid point of the line-free coverage.

Table E.3. Image cube properties.

Star	Configuration	Cube No.	Low (GHz)	High (GHz)	b_{maj} (arcsec)	b_{min} (arcsec)	b_{PA} (deg)	Imsize (arcsec)	σ_{rms} (mJy)
AH_Sco	extended	00	213.865	215.738	0.024	0.022	0	2.0	0.4
AH_Sco	extended	01	216.065	217.938	0.025	0.023	5	2.0	0.6
AH_Sco	extended	02	220.265	222.138	0.027	0.023	86	2.0	0.6
AH_Sco	extended	03	223.660	225.533	0.026	0.024	82	2.0	0.5
AH_Sco	extended	04	227.263	229.136	0.022	0.021	−12	2.0	0.5
AH_Sco	extended	05	229.618	231.491	0.022	0.020	−21	2.0	0.4
AH_Sco	extended	06	235.468	237.341	0.025	0.021	−84	2.0	0.5
AH_Sco	extended	07	239.187	240.122	0.026	0.023	74	2.0	0.8
AH_Sco	extended	08	244.082	245.018	0.046	0.034	57	2.0	4.8
AH_Sco	extended	09	245.375	247.248	0.036	0.025	55	2.0	1.0
AH_Sco	extended	10	251.621	253.494	0.044	0.026	39	2.0	1.2
AH_Sco	extended	11	253.954	255.827	0.048	0.028	37	2.0	1.5
AH_Sco	extended	12	258.682	260.555	0.043	0.034	49	2.0	4.1
AH_Sco	extended	13	262.137	263.073	0.045	0.036	59	2.0	6.2
AH_Sco	extended	14	265.569	267.442	0.049	0.027	40	2.0	1.8
AH_Sco	extended	15	267.819	269.692	0.040	0.023	38	2.0	1.0
AH_Sco	mid	00	213.865	215.738	0.193	0.109	−75	12.0	1.1
AH_Sco	mid	01	216.065	217.938	0.188	0.104	−79	12.0	1.2
AH_Sco	mid	02	220.265	222.138	0.178	0.104	−75	12.0	1.3
AH_Sco	mid	03	223.659	225.532	0.157	0.102	−82	12.0	1.0
AH_Sco	mid	04	227.263	229.136	0.179	0.099	−79	12.0	1.1
AH_Sco	mid	05	229.618	231.491	0.178	0.100	−78	12.0	1.1
AH_Sco	mid	06	235.468	237.341	0.148	0.097	−82	12.0	1.2
AH_Sco	mid	07	239.187	240.123	0.160	0.094	−80	12.0	1.3
AH_Sco	mid	08	244.082	245.018	0.129	0.091	−87	12.0	1.7
AH_Sco	mid	09	245.375	247.248	0.129	0.091	−87	12.0	1.5
AH_Sco	mid	10	251.621	253.494	0.322	0.250	71	12.0	1.3
AH_Sco	mid	11	253.954	255.827	0.321	0.248	71	12.0	1.3
AH_Sco	mid	12	258.682	260.556	0.120	0.086	−88	12.0	1.7
AH_Sco	mid	13	262.137	263.073	0.118	0.085	−87	12.0	2.0
AH_Sco	mid	14	265.569	267.442	0.305	0.239	72	12.0	1.5
AH_Sco	mid	15	267.819	269.692	0.304	0.235	71	12.0	1.6
GY_Aql	extended	00	213.838	215.711	0.028	0.025	21	2.0	1.8
GY_Aql	extended	01	216.038	217.910	0.028	0.025	13	2.0	2.0
GY_Aql	extended	02	220.237	222.110	0.027	0.026	0	2.0	2.1
GY_Aql	extended	03	223.631	225.504	0.026	0.025	−28	2.0	1.7
GY_Aql	extended	04	227.234	229.107	0.026	0.024	6	2.0	1.9
GY_Aql	extended	05	229.589	231.462	0.026	0.024	−3	2.0	1.8
GY_Aql	extended	06	235.438	237.311	0.025	0.024	−33	2.0	1.8
GY_Aql	extended	07	239.157	240.092	0.025	0.024	−29	2.0	2.1
GY_Aql	extended	08	244.051	244.987	0.034	0.026	84	2.0	3.1
GY_Aql	extended	09	245.344	247.217	0.033	0.025	86	2.0	2.2
GY_Aql	extended	10	251.588	253.461	0.033	0.021	−66	2.0	2.9
GY_Aql	extended	11	253.921	255.794	0.033	0.021	−68	2.0	3.0
GY_Aql	extended	12	258.650	260.522	0.032	0.024	83	2.0	2.9
GY_Aql	extended	13	262.104	263.039	0.032	0.024	82	2.0	3.5
GY_Aql	extended	14	265.535	267.408	0.032	0.022	−78	2.0	3.4
GY_Aql	extended	15	267.785	269.657	0.031	0.022	−77	2.0	3.5
GY_Aql	mid	00	213.838	215.711	0.382	0.319	−74	24.0	2.0
GY_Aql	mid	01	216.037	217.911	0.375	0.318	−76	24.0	2.1
GY_Aql	mid	02	220.237	222.110	0.364	0.295	−73	24.0	2.0
GY_Aql	mid	03	223.631	225.504	0.358	0.290	−76	24.0	1.7
GY_Aql	mid	04	227.235	229.108	0.357	0.304	−79	24.0	2.2
GY_Aql	mid	05	229.589	231.462	0.358	0.298	−78	24.0	2.1
GY_Aql	mid	06	235.438	237.311	0.340	0.272	−76	24.0	1.9
GY_Aql	mid	07	239.157	240.092	0.340	0.275	−74	24.0	2.1
GY_Aql	mid	08	244.051	244.987	0.397	0.278	−75	24.0	2.7

Table E.3. continued.

Star	Configuration	Cube No.	Low (GHz)	High (GHz)	b_{maj} (arcsec)	b_{min} (arcsec)	b_{PA} (deg)	Imsize (arcsec)	σ_{rms} (mJy)
GY_Aql	mid	09	245.350	247.223	0.395	0.273	−76	24.0	2.3
GY_Aql	mid	10	251.583	253.456	0.351	0.273	−71	24.0	4.0
GY_Aql	mid	11	253.947	255.820	0.349	0.271	−71	24.0	4.1
GY_Aql	mid	12	258.624	260.497	0.377	0.260	−75	24.0	2.6
GY_Aql	mid	13	262.104	263.039	0.371	0.262	−75	24.0	3.0
GY_Aql	mid	14	265.533	267.406	0.334	0.257	−70	24.0	4.6
GY_Aql	mid	15	267.783	269.657	0.333	0.257	−73	24.0	4.9
GY_Aql	compact	00	213.838	215.711	1.343	1.045	64	24.0	2.6
GY_Aql	compact	01	216.038	217.910	1.360	1.047	66	24.0	3.1
GY_Aql	compact	04	227.234	229.107	1.286	1.013	69	24.0	2.7
GY_Aql	compact	05	229.589	231.462	1.265	0.986	67	24.0	2.8
GY_Aql	compact	08	244.051	244.987	1.294	0.929	65	24.0	2.5
GY_Aql	compact	09	245.350	247.223	1.278	0.925	66	24.0	2.3
GY_Aql	compact	12	258.623	260.496	1.223	0.885	66	24.0	2.4
GY_Aql	compact	13	262.104	263.039	1.207	0.876	66	24.0	3.0
IRC+10011	extended	00	213.855	215.728	0.033	0.024	42	5.0	2.3
IRC+10011	extended	01	216.055	217.928	0.032	0.024	42	5.0	2.6
IRC+10011	extended	02	220.255	222.128	0.030	0.024	30	5.0	2.8
IRC+10011	extended	03	223.650	225.523	0.030	0.024	30	5.0	2.4
IRC+10011	extended	04	227.252	229.125	0.035	0.021	37	5.0	2.6
IRC+10011	extended	05	229.607	231.480	0.031	0.022	40	5.0	2.4
IRC+10011	extended	06	235.457	237.330	0.032	0.022	32	5.0	2.6
IRC+10011	extended	07	239.176	240.111	0.028	0.023	30	5.0	3.2
IRC+10011	extended	08	244.071	245.006	0.029	0.022	23	5.0	2.0
IRC+10011	extended	09	245.364	247.237	0.026	0.020	25	5.0	1.6
IRC+10011	extended	10	251.609	253.482	0.026	0.020	24	5.0	1.6
IRC+10011	extended	11	253.942	255.815	0.025	0.020	24	5.0	1.7
IRC+10011	extended	12	258.670	260.543	0.026	0.019	24	5.0	1.7
IRC+10011	extended	13	262.125	263.060	0.026	0.020	22	5.0	2.1
IRC+10011	extended	14	265.556	267.429	0.026	0.019	25	5.0	2.0
IRC+10011	extended	15	267.806	269.679	0.024	0.019	26	5.0	1.9
IRC+10011	mid	00	213.855	215.728	0.139	0.127	37	18.0	2.0
IRC+10011	mid	01	216.055	217.928	0.138	0.126	38	18.0	2.1
IRC+10011	mid	02	220.255	222.128	0.138	0.123	46	18.0	2.4
IRC+10011	mid	03	223.650	225.523	0.136	0.121	43	18.0	2.0
IRC+10011	mid	04	227.252	229.125	0.131	0.121	37	18.0	2.1
IRC+10011	mid	05	229.607	231.480	0.130	0.121	38	18.0	2.1
IRC+10011	mid	06	235.457	237.330	0.129	0.116	37	18.0	2.2
IRC+10011	mid	07	239.176	240.111	0.128	0.117	37	18.0	2.4
IRC+10011	mid	08	244.071	245.006	0.122	0.115	6	18.0	2.5
IRC+10011	mid	09	245.364	247.237	0.119	0.114	10	18.0	2.2
IRC+10011	mid	10	251.609	253.482	0.124	0.116	−34	18.0	4.6
IRC+10011	mid	11	253.942	255.815	0.120	0.113	1	18.0	4.6
IRC+10011	mid	12	258.670	260.543	0.113	0.108	−1	18.0	2.4
IRC+10011	mid	13	262.125	263.060	0.113	0.109	−6	18.0	2.8
IRC+10011	mid	14	265.556	267.429	0.115	0.106	6	18.0	5.3
IRC+10011	mid	15	267.806	269.679	0.116	0.107	0	18.0	5.3
IRC+10011	compact	00	213.855	215.728	0.852	0.801	0	24.0	3.0
IRC+10011	compact	01	216.055	217.928	0.843	0.792	8	24.0	3.1
IRC+10011	compact	04	227.253	229.126	0.820	0.755	0	24.0	3.3
IRC+10011	compact	05	229.607	231.481	0.801	0.750	1	24.0	3.3
IRC+10011	compact	08	244.071	245.006	0.785	0.680	−67	24.0	3.5
IRC+10011	compact	09	245.370	247.243	0.783	0.674	−68	24.0	3.3
IRC+10011	compact	12	258.644	260.518	0.748	0.649	−62	24.0	3.5
IRC+10011	compact	13	262.125	263.061	0.738	0.640	−68	24.0	4.0
IRC−10529	extended	00	213.875	215.748	0.033	0.028	−57	2.0	1.8
IRC−10529	extended	01	216.075	217.948	0.039	0.028	66	2.0	3.3

Table E.3. continued.

Star	Configuration	Cube No.	Low (GHz)	High (GHz)	b_{maj} (arcsec)	b_{min} (arcsec)	b_{PA} (deg)	Imsize (arcsec)	σ_{rms} (mJy)
IRC-10529	extended	02	220.276	222.148	0.033	0.030	−82	2.0	2.9
IRC-10529	extended	03	223.671	225.544	0.030	0.024	−55	2.0	2.1
IRC-10529	extended	04	227.273	229.145	0.029	0.027	−62	2.0	2.0
IRC-10529	extended	05	229.629	231.502	0.030	0.024	−53	2.0	1.8
IRC-10529	extended	06	235.479	237.352	0.030	0.027	−76	2.0	2.7
IRC-10529	extended	07	239.198	240.134	0.037	0.029	−85	2.0	7.1
IRC-10529	extended	08	244.094	245.029	0.032	0.024	47	2.0	4.0
IRC-10529	extended	09	245.387	247.260	0.024	0.023	−60	2.0	1.9
IRC-10529	extended	10	251.634	253.507	0.029	0.026	82	2.0	2.8
IRC-10529	extended	11	253.967	255.839	0.032	0.027	−61	2.0	3.0
IRC-10529	extended	12	258.693	260.566	0.023	0.022	−49	2.0	2.2
IRC-10529	extended	13	262.150	263.085	0.028	0.021	48	2.0	3.5
IRC-10529	extended	14	265.581	267.454	0.034	0.025	67	2.0	3.9
IRC-10529	extended	15	267.831	269.704	0.031	0.023	62	2.0	3.7
IRC-10529	mid	00	213.875	215.748	0.152	0.112	−65	12.0	2.0
IRC-10529	mid	01	216.075	217.948	0.143	0.112	−69	12.0	2.2
IRC-10529	mid	02	220.275	222.148	0.137	0.112	−68	12.0	2.5
IRC-10529	mid	03	223.670	225.543	0.135	0.111	−75	12.0	2.1
IRC-10529	mid	04	227.273	229.146	0.135	0.109	−68	12.0	2.1
IRC-10529	mid	05	229.629	231.502	0.134	0.108	−66	12.0	2.1
IRC-10529	mid	06	235.479	237.352	0.126	0.106	−66	12.0	2.2
IRC-10529	mid	07	239.198	240.134	0.125	0.106	−67	12.0	2.3
IRC-10529	mid	08	244.093	245.029	0.130	0.105	−65	12.0	2.6
IRC-10529	mid	09	245.387	247.260	0.131	0.101	−65	12.0	2.3
IRC-10529	mid	10	251.633	253.506	0.329	0.244	−66	12.0	4.5
IRC-10529	mid	11	253.966	255.839	0.329	0.244	−66	12.0	4.3
IRC-10529	mid	12	258.694	260.567	0.123	0.096	−67	12.0	2.5
IRC-10529	mid	13	262.149	263.085	0.122	0.098	−64	12.0	3.0
IRC-10529	mid	14	265.581	267.454	0.323	0.259	−68	12.0	5.5
IRC-10529	mid	15	267.831	269.704	0.310	0.235	−67	12.0	5.2
IRC-10529	compact	00	213.875	215.748	0.846	0.680	78	24.0	2.6
IRC-10529	compact	01	216.075	217.948	0.934	0.694	74	24.0	3.0
IRC-10529	compact	04	227.273	229.146	0.819	0.646	79	24.0	2.7
IRC-10529	compact	05	229.629	231.502	0.801	0.642	76	24.0	2.7
IRC-10529	compact	08	244.093	245.029	0.969	0.793	69	24.0	4.3
IRC-10529	compact	09	245.387	247.260	0.953	0.826	64	24.0	4.0
IRC-10529	compact	12	258.694	260.567	0.925	0.751	80	24.0	4.1
IRC-10529	compact	13	262.149	263.085	0.914	0.746	78	24.0	4.6
KW_Sgr	extended	00	213.859	215.732	0.027	0.023	−70	1.6	0.6
KW_Sgr	extended	01	216.059	217.932	0.027	0.023	−72	1.6	0.7
KW_Sgr	extended	02	220.259	222.132	0.024	0.024	32	1.6	0.7
KW_Sgr	extended	03	223.654	225.527	0.024	0.023	−81	1.6	0.6
KW_Sgr	extended	04	227.257	229.130	0.025	0.023	−72	1.6	0.6
KW_Sgr	extended	05	229.612	231.485	0.025	0.022	−69	1.6	0.7
KW_Sgr	extended	06	235.462	237.335	0.022	0.022	−74	1.6	0.6
KW_Sgr	extended	07	239.181	240.116	0.022	0.021	−67	1.6	0.7
KW_Sgr	extended	08	244.076	245.011	0.041	0.025	83	1.6	1.2
KW_Sgr	extended	09	245.369	247.242	0.041	0.025	82	1.6	1.1
KW_Sgr	extended	10	251.614	253.487	0.021	0.021	47	1.6	0.7
KW_Sgr	extended	11	253.947	255.820	0.021	0.020	−53	1.6	0.6
KW_Sgr	extended	12	258.675	260.548	0.039	0.024	82	1.6	1.2
KW_Sgr	extended	13	262.130	263.066	0.038	0.023	82	1.6	1.4
KW_Sgr	extended	14	265.561	267.434	0.020	0.019	−47	1.6	0.8
KW_Sgr	extended	15	267.811	269.684	0.020	0.019	−51	1.6	0.7
KW_Sgr	mid	00	213.859	215.732	0.247	0.112	−75	12.0	1.8
KW_Sgr	mid	01	216.059	217.932	0.220	0.114	−76	12.0	2.1
KW_Sgr	mid	02	220.259	222.132	0.137	0.102	−87	12.0	1.8
KW_Sgr	mid	03	223.653	225.526	0.124	0.104	−81	12.0	1.5

Table E.3. continued.

Star	Configuration	Cube No.	Low (GHz)	High (GHz)	b_{maj} (arcsec)	b_{min} (arcsec)	b_{PA} (deg)	Imsize (arcsec)	σ_{rms} (mJy)
KW_Sgr	mid	04	227.257	229.130	0.214	0.102	−73	12.0	2.1
KW_Sgr	mid	05	229.612	231.485	0.210	0.103	−75	12.0	1.9
KW_Sgr	mid	06	235.462	237.335	0.119	0.100	−71	12.0	1.8
KW_Sgr	mid	07	239.181	240.116	0.130	0.098	−89	12.0	2.1
KW_Sgr	mid	08	244.075	245.011	0.204	0.116	−70	12.0	2.2
KW_Sgr	mid	09	245.375	247.248	0.202	0.110	−73	12.0	1.8
KW_Sgr	mid	10	251.614	253.487	0.348	0.269	73	12.0	1.8
KW_Sgr	mid	11	253.947	255.820	0.323	0.247	−86	12.0	1.6
KW_Sgr	mid	12	258.649	260.522	0.174	0.107	−74	12.0	1.8
KW_Sgr	mid	13	262.130	263.066	0.193	0.105	−74	12.0	2.6
KW_Sgr	mid	14	265.561	267.434	0.532	0.262	71	12.0	2.3
KW_Sgr	mid	15	267.811	269.684	0.406	0.238	87	12.0	2.1
pi1_Gru	extended	00	213.871	215.744	0.026	0.023	0	1.2	0.9
pi1_Gru	extended	01	216.071	217.944	0.024	0.021	5	1.2	1.0
pi1_Gru	extended	02	220.272	222.145	0.025	0.021	−13	1.2	1.1
pi1_Gru	extended	03	223.667	225.540	0.024	0.021	−9	1.2	1.0
pi1_Gru	extended	04	227.269	229.142	0.023	0.020	6	1.2	1.0
pi1_Gru	extended	05	229.625	231.498	0.023	0.020	2	1.2	1.0
pi1_Gru	extended	06	235.475	237.348	0.023	0.020	−9	1.2	1.0
pi1_Gru	extended	07	239.194	240.130	0.023	0.020	−3	1.2	1.2
pi1_Gru	extended	08	244.089	245.025	0.025	0.019	60	1.2	1.4
pi1_Gru	extended	09	245.383	247.256	0.025	0.019	59	1.2	1.1
pi1_Gru	extended	10	251.629	253.502	0.027	0.018	68	1.2	1.2
pi1_Gru	extended	11	253.962	255.835	0.028	0.020	68	1.2	1.2
pi1_Gru	extended	12	258.689	260.562	0.025	0.019	59	1.2	1.2
pi1_Gru	extended	13	262.145	263.081	0.024	0.018	58	1.2	1.5
pi1_Gru	extended	14	265.577	267.450	0.025	0.018	69	1.2	1.4
pi1_Gru	extended	15	267.827	269.700	0.025	0.018	68	1.2	1.4
pi1_Gru	mid	00	213.871	215.744	0.353	0.308	31	24.0	3.1
pi1_Gru	mid	01	216.071	217.945	0.341	0.308	26	24.0	3.5
pi1_Gru	mid	02	220.272	222.145	0.338	0.310	23	24.0	3.5
pi1_Gru	mid	03	223.666	225.539	0.334	0.306	23	24.0	3.1
pi1_Gru	mid	04	227.270	229.143	0.328	0.294	27	24.0	3.4
pi1_Gru	mid	05	229.625	231.498	0.327	0.293	32	24.0	3.3
pi1_Gru	mid	06	235.475	237.348	0.320	0.289	28	24.0	3.3
pi1_Gru	mid	07	239.194	240.130	0.321	0.291	26	24.0	3.6
pi1_Gru	mid	08	244.089	245.025	0.318	0.275	36	24.0	3.5
pi1_Gru	mid	09	245.383	247.256	0.315	0.272	36	24.0	3.3
pi1_Gru	mid	10	251.628	253.501	0.285	0.262	34	24.0	2.2
pi1_Gru	mid	11	253.961	255.834	0.284	0.259	34	24.0	2.3
pi1_Gru	mid	12	258.690	260.563	0.298	0.256	33	24.0	3.4
pi1_Gru	mid	13	262.145	263.081	0.293	0.256	34	24.0	4.0
pi1_Gru	mid	14	265.576	267.450	0.271	0.251	37	24.0	2.7
pi1_Gru	mid	15	267.827	269.700	0.269	0.249	37	24.0	2.7
pi1_Gru	compact	00	213.871	215.744	0.844	0.828	88	36.0	2.6
pi1_Gru	compact	01	216.071	217.945	0.842	0.827	76	36.0	2.9
pi1_Gru	compact	04	227.270	229.143	0.815	0.792	−56	36.0	2.9
pi1_Gru	compact	05	229.625	231.498	0.807	0.768	−80	36.0	2.9
pi1_Gru	compact	08	244.089	245.025	1.334	1.020	−85	36.0	2.5
pi1_Gru	compact	09	245.383	247.256	1.321	1.012	−82	36.0	2.2
pi1_Gru	compact	12	258.689	260.562	1.258	0.982	−80	36.0	2.6
pi1_Gru	compact	13	262.145	263.081	1.247	0.956	−83	36.0	2.9
RW_Sco	extended	00	213.915	215.788	0.034	0.026	−71	2.0	1.9
RW_Sco	extended	01	216.114	217.987	0.030	0.028	−88	2.0	3.2
RW_Sco	extended	02	220.315	222.188	0.028	0.024	−67	2.0	2.0
RW_Sco	extended	03	223.711	225.584	0.028	0.024	−63	2.0	1.5

Table E.3. continued.

Star	Configuration	Cube No.	Low (GHz)	High (GHz)	b_{maj} (arcsec)	b_{min} (arcsec)	b_{PA} (deg)	Imsize (arcsec)	σ_{rms} (mJy)
RW_Sco	extended	04	227.313	229.186	0.030	0.024	−79	2.0	2.0
RW_Sco	extended	05	229.670	231.543	0.031	0.023	−73	2.0	1.8
RW_Sco	extended	06	235.522	237.395	0.026	0.024	−68	2.0	1.9
RW_Sco	extended	07	239.241	240.177	0.028	0.024	20	2.0	2.8
RW_Sco	extended	08	244.138	245.073	0.029	0.024	0	2.0	4.4
RW_Sco	extended	09	245.431	247.304	0.026	0.020	−58	2.0	1.7
RW_Sco	extended	10	251.680	253.553	0.026	0.021	−69	2.0	1.7
RW_Sco	extended	11	254.013	255.886	0.026	0.020	−68	2.0	1.8
RW_Sco	extended	12	258.739	260.612	0.024	0.020	−55	2.0	1.9
RW_Sco	extended	13	262.197	263.132	0.025	0.019	−44	2.0	3.6
RW_Sco	extended	14	265.629	267.502	0.024	0.020	−68	2.0	2.1
RW_Sco	extended	15	267.879	269.753	0.025	0.019	−67	2.0	2.0
RW_Sco	mid	00	213.914	215.787	0.159	0.120	−72	12.0	4.1
RW_Sco	mid	01	216.114	217.987	0.144	0.113	87	12.0	3.9
RW_Sco	mid	02	220.315	222.188	0.146	0.110	−85	12.0	4.3
RW_Sco	mid	03	223.710	225.584	0.137	0.112	−87	12.0	3.5
RW_Sco	mid	04	227.313	229.187	0.133	0.108	−87	12.0	3.8
RW_Sco	mid	05	229.670	231.543	0.134	0.109	−85	12.0	3.6
RW_Sco	mid	06	235.522	237.395	0.129	0.108	−84	12.0	3.8
RW_Sco	mid	07	239.241	240.177	0.139	0.109	−82	12.0	4.3
RW_Sco	mid	08	244.137	245.073	0.131	0.107	84	12.0	4.6
RW_Sco	mid	09	245.431	247.304	0.127	0.103	−86	12.0	3.8
RW_Sco	mid	10	251.680	253.553	0.314	0.277	34	12.0	4.1
RW_Sco	mid	11	254.013	255.886	0.333	0.302	19	12.0	4.4
RW_Sco	mid	12	258.740	260.613	0.116	0.091	89	12.0	4.8
RW_Sco	mid	13	262.197	263.132	0.158	0.090	−85	12.0	7.3
RW_Sco	mid	14	265.629	267.502	0.287	0.260	−18	12.0	6.0
RW_Sco	mid	15	267.879	269.753	0.338	0.277	−88	12.0	5.8
RW_Sco	compact	00	213.915	215.788	1.099	0.797	87	24.0	2.3
RW_Sco	compact	01	216.114	217.987	1.398	0.902	−77	24.0	3.5
RW_Sco	compact	04	227.313	229.186	1.059	0.739	88	24.0	2.4
RW_Sco	compact	05	229.670	231.543	1.033	0.730	88	24.0	2.3
RW_Sco	compact	08	244.138	245.073	0.899	0.806	73	24.0	2.9
RW_Sco	compact	09	245.431	247.304	0.900	0.789	73	24.0	2.4
RW_Sco	compact	12	258.739	260.612	0.875	0.745	72	24.0	2.7
RW_Sco	compact	13	262.197	263.132	0.876	0.745	64	24.0	3.1
R_Aql	extended	00	213.828	215.701	0.029	0.023	36	2.0	0.7
R_Aql	extended	01	216.028	217.901	0.029	0.022	36	2.0	0.7
R_Aql	extended	02	220.227	222.100	0.027	0.022	18	2.0	0.8
R_Aql	extended	03	223.621	225.494	0.026	0.021	21	2.0	0.7
R_Aql	extended	04	227.224	229.097	0.028	0.021	34	2.0	0.7
R_Aql	extended	05	229.579	231.452	0.027	0.021	33	2.0	0.7
R_Aql	extended	06	235.428	237.301	0.025	0.020	20	2.0	0.7
R_Aql	extended	07	239.146	240.082	0.024	0.020	19	2.0	0.8
R_Aql	extended	08	244.040	244.976	0.027	0.020	−30	2.0	0.9
R_Aql	extended	09	245.340	247.213	0.027	0.020	−31	2.0	0.7
R_Aql	extended	10	251.577	253.450	0.029	0.020	−43	2.0	0.7
R_Aql	extended	11	253.910	255.783	0.029	0.020	−44	2.0	0.7
R_Aql	extended	12	258.612	260.485	0.025	0.019	−30	2.0	0.8
R_Aql	extended	13	262.093	263.028	0.025	0.019	−30	2.0	0.9
R_Aql	extended	14	265.523	267.396	0.028	0.019	−43	2.0	0.8
R_Aql	extended	15	267.773	269.646	0.028	0.019	−42	2.0	0.8
R_Aql	mid	00	213.828	215.701	0.418	0.307	−54	24.0	2.6
R_Aql	mid	01	216.028	217.901	0.419	0.303	−53	24.0	2.9
R_Aql	mid	02	220.227	222.100	0.409	0.301	−54	24.0	2.9
R_Aql	mid	03	223.621	225.494	0.411	0.297	−53	24.0	2.7
R_Aql	mid	04	227.225	229.098	0.398	0.290	−55	24.0	2.8

Table E.3. continued.

Star	Configuration	Cube No.	Low (GHz)	High (GHz)	b_{maj} (arcsec)	b_{min} (arcsec)	b_{PA} (deg)	Imsize (arcsec)	σ_{rms} (mJy)
R_Aql	mid	05	229.579	231.452	0.390	0.286	−55	24.0	2.7
R_Aql	mid	06	235.428	237.301	0.387	0.322	−60	24.0	2.9
R_Aql	mid	07	239.146	240.082	0.386	0.321	−61	24.0	3.4
R_Aql	mid	08	244.040	244.976	0.324	0.295	−68	24.0	2.5
R_Aql	mid	09	245.339	247.212	0.324	0.288	−65	24.0	2.3
R_Aql	mid	10	251.572	253.445	0.363	0.281	−54	24.0	2.8
R_Aql	mid	11	253.936	255.809	0.364	0.279	−55	24.0	2.7
R_Aql	mid	12	258.613	260.486	0.304	0.280	−70	24.0	2.5
R_Aql	mid	13	262.093	263.028	0.304	0.278	−70	24.0	2.9
R_Aql	mid	14	265.522	267.395	0.356	0.277	−55	24.0	3.4
R_Aql	mid	15	267.772	269.645	0.343	0.270	−55	24.0	3.3
R_Aql	compact	00	213.828	215.701	0.945	0.778	73	28.0	2.8
R_Aql	compact	01	216.028	217.901	0.947	0.773	72	28.0	2.8
R_Aql	compact	04	227.225	229.098	0.909	0.732	72	28.0	2.9
R_Aql	compact	05	229.579	231.452	0.895	0.736	73	28.0	3.0
R_Aql	compact	08	244.040	244.976	0.793	0.699	−76	28.0	3.2
R_Aql	compact	09	245.339	247.212	0.788	0.691	−74	28.0	3.0
R_Aql	compact	12	258.612	260.485	0.763	0.663	−76	28.0	3.1
R_Aql	compact	13	262.093	263.028	0.769	0.661	−79	28.0	3.5
R_Hya	extended	00	213.870	215.743	0.046	0.030	70	2.0	0.8
R_Hya	extended	01	216.070	217.943	0.047	0.029	68	2.0	0.9
R_Hya	extended	02	220.270	222.143	0.041	0.030	45	2.0	1.2
R_Hya	extended	03	223.664	225.537	0.040	0.030	44	2.0	1.0
R_Hya	extended	04	227.268	229.141	0.046	0.028	68	2.0	0.8
R_Hya	extended	05	229.623	231.497	0.046	0.029	68	2.0	0.8
R_Hya	extended	06	235.474	237.347	0.038	0.028	44	2.0	1.1
R_Hya	extended	07	239.193	240.128	0.037	0.028	44	2.0	1.2
R_Hya	extended	08	244.088	245.023	0.050	0.028	75	2.0	0.8
R_Hya	extended	09	245.381	247.254	0.050	0.029	74	2.0	0.7
R_Hya	extended	10	251.626	253.499	0.039	0.031	46	2.0	0.8
R_Hya	extended	11	253.959	255.833	0.039	0.030	49	2.0	0.8
R_Hya	extended	12	258.688	260.562	0.048	0.028	72	2.0	0.8
R_Hya	extended	13	262.143	263.079	0.047	0.027	73	2.0	0.9
R_Hya	extended	14	265.575	267.448	0.038	0.029	48	2.0	0.9
R_Hya	extended	15	267.825	269.698	0.038	0.029	48	2.0	0.9
R_Hya	mid	00	213.870	215.743	0.307	0.274	−85	24.0	1.7
R_Hya	mid	01	216.070	217.943	0.306	0.273	−80	24.0	1.8
R_Hya	mid	02	220.270	222.143	0.369	0.292	76	24.0	1.8
R_Hya	mid	03	223.665	225.538	0.367	0.288	79	24.0	1.5
R_Hya	mid	04	227.268	229.141	0.294	0.258	−84	24.0	1.8
R_Hya	mid	05	229.623	231.496	0.290	0.256	−84	24.0	1.7
R_Hya	mid	06	235.474	237.347	0.356	0.279	83	24.0	1.6
R_Hya	mid	07	239.193	240.128	0.352	0.274	81	24.0	1.9
R_Hya	mid	08	244.088	245.023	0.298	0.259	55	24.0	2.0
R_Hya	mid	09	245.381	247.254	0.277	0.260	50	24.0	1.7
R_Hya	mid	10	251.627	253.500	0.283	0.238	62	24.0	1.2
R_Hya	mid	11	253.960	255.833	0.285	0.236	55	24.0	1.3
R_Hya	mid	12	258.688	260.561	0.277	0.241	59	24.0	1.9
R_Hya	mid	13	262.143	263.079	0.281	0.243	52	24.0	2.2
R_Hya	mid	14	265.575	267.448	0.273	0.227	62	24.0	1.5
R_Hya	mid	15	267.825	269.698	0.264	0.224	63	24.0	1.5
R_Hya	compact	00	213.870	215.743	0.976	0.682	78	28.0	2.4
R_Hya	compact	01	216.070	217.943	0.983	0.675	77	28.0	2.6
R_Hya	compact	04	227.267	229.140	0.957	0.649	78	28.0	2.5
R_Hya	compact	05	229.624	231.496	0.947	0.634	78	28.0	2.5
R_Hya	compact	08	244.088	245.023	0.847	0.727	−83	28.0	3.8
R_Hya	compact	09	245.381	247.254	0.887	0.738	81	28.0	3.2

Table E.3. continued.

Star	Configuration	Cube No.	Low (GHz)	High (GHz)	b_{maj} (arcsec)	b_{min} (arcsec)	b_{PA} (deg)	Imsize (arcsec)	σ_{rms} (mJy)
R_Hya	compact	12	258.687	260.560	0.836	0.717	74	28.0	3.9
R_Hya	compact	13	262.143	263.079	0.804	0.702	−84	28.0	4.3
SV_Aqr	extended	00	213.856	215.729	0.029	0.023	48	2.0	0.8
SV_Aqr	extended	01	216.056	217.929	0.030	0.022	48	2.0	0.9
SV_Aqr	extended	02	220.256	222.129	0.023	0.022	33	2.0	1.1
SV_Aqr	extended	03	223.651	225.524	0.023	0.021	35	2.0	0.9
SV_Aqr	extended	04	227.253	229.126	0.030	0.021	48	2.0	0.9
SV_Aqr	extended	05	229.609	231.481	0.028	0.022	48	2.0	0.8
SV_Aqr	extended	06	235.458	237.331	0.021	0.020	28	2.0	1.0
SV_Aqr	extended	07	239.177	240.112	0.021	0.020	26	2.0	1.2
SV_Aqr	extended	08	244.072	245.007	0.021	0.020	−83	2.0	1.2
SV_Aqr	extended	09	245.365	247.238	0.021	0.020	−27	2.0	1.0
SV_Aqr	extended	10	251.611	253.484	0.022	0.021	88	2.0	0.9
SV_Aqr	extended	11	253.944	255.816	0.022	0.021	89	2.0	0.9
SV_Aqr	extended	12	258.671	260.544	0.020	0.019	−13	2.0	1.1
SV_Aqr	extended	13	262.126	263.062	0.020	0.019	−19	2.0	1.4
SV_Aqr	extended	14	265.557	267.430	0.021	0.019	−59	2.0	1.1
SV_Aqr	extended	15	267.807	269.680	0.021	0.019	−57	2.0	1.1
SV_Aqr	mid	00	213.856	215.729	0.143	0.101	−77	24.0	1.9
SV_Aqr	mid	01	216.056	217.929	0.183	0.097	−61	24.0	3.0
SV_Aqr	mid	02	220.256	222.129	0.136	0.100	88	24.0	3.0
SV_Aqr	mid	03	223.651	225.524	0.138	0.099	−58	24.0	2.8
SV_Aqr	mid	04	227.253	229.126	0.117	0.094	73	24.0	3.1
SV_Aqr	mid	05	229.608	231.481	0.129	0.095	84	24.0	2.3
SV_Aqr	mid	06	235.458	237.331	0.124	0.086	−83	24.0	2.8
SV_Aqr	mid	07	239.177	240.112	0.234	0.136	−72	24.0	5.7
SV_Aqr	mid	08	244.072	245.007	0.190	0.134	88	24.0	5.2
SV_Aqr	mid	09	245.365	247.238	0.117	0.090	−77	24.0	2.0
SV_Aqr	mid	10	251.609	253.483	0.277	0.258	−88	24.0	2.2
SV_Aqr	mid	11	253.943	255.816	0.279	0.255	−77	24.0	2.2
SV_Aqr	mid	12	258.671	260.544	0.108	0.093	−56	24.0	2.3
SV_Aqr	mid	13	262.126	263.062	0.105	0.079	−32	24.0	5.7
SV_Aqr	mid	14	265.557	267.431	0.309	0.253	−63	24.0	2.7
SV_Aqr	mid	15	267.807	269.680	0.257	0.235	−89	24.0	2.7
SV_Aqr	compact	00	213.856	215.729	0.903	0.762	75	24.0	2.6
SV_Aqr	compact	01	216.056	217.929	0.910	0.759	77	24.0	2.6
SV_Aqr	compact	04	227.254	229.127	0.871	0.731	78	24.0	2.6
SV_Aqr	compact	05	229.608	231.482	0.848	0.717	78	24.0	2.6
SV_Aqr	compact	08	244.072	245.007	1.120	0.945	71	24.0	3.2
SV_Aqr	compact	09	245.365	247.238	1.114	0.936	70	24.0	3.0
SV_Aqr	compact	12	258.671	260.544	1.064	0.895	73	24.0	3.1
SV_Aqr	compact	13	262.126	263.062	1.049	0.888	70	24.0	3.7
S_Pav	extended	00	213.876	215.749	0.030	0.023	−17	2.0	0.7
S_Pav	extended	01	216.077	217.950	0.028	0.021	−20	2.0	0.8
S_Pav	extended	02	220.277	222.150	0.027	0.021	−3	2.0	0.8
S_Pav	extended	03	223.672	225.545	0.027	0.020	0	2.0	0.7
S_Pav	extended	04	227.274	229.147	0.027	0.020	−21	2.0	0.8
S_Pav	extended	05	229.630	231.503	0.027	0.020	−23	2.0	0.7
S_Pav	extended	06	235.481	237.354	0.025	0.019	−2	2.0	0.8
S_Pav	extended	07	239.200	240.135	0.025	0.019	−3	2.0	0.9
S_Pav	extended	08	244.095	245.031	0.026	0.020	−21	2.0	1.0
S_Pav	extended	09	245.388	247.261	0.026	0.020	−20	2.0	0.9
S_Pav	extended	10	251.635	253.508	0.025	0.020	11	2.0	1.0
S_Pav	extended	11	253.968	255.841	0.024	0.019	6	2.0	1.0
S_Pav	extended	12	258.696	260.569	0.024	0.019	−19	2.0	1.0
S_Pav	extended	13	262.151	263.087	0.024	0.018	−20	2.0	1.2

Table E.3. continued.

Star	Configuration	Cube No.	Low (GHz)	High (GHz)	b_{maj} (arcsec)	b_{min} (arcsec)	b_{PA} (deg)	Imsize (arcsec)	σ_{rms} (mJy)
S_Pav	extended	14	265.583	267.456	0.023	0.019	4	2.0	1.2
S_Pav	extended	15	267.833	269.706	0.023	0.018	4	2.0	1.1
S_Pav	mid	00	213.876	215.749	0.417	0.287	57	24.0	2.0
S_Pav	mid	01	216.076	217.950	0.416	0.282	57	24.0	2.0
S_Pav	mid	02	220.277	222.150	0.425	0.294	64	24.0	2.7
S_Pav	mid	03	223.671	225.544	0.421	0.286	64	24.0	2.4
S_Pav	mid	04	227.275	229.148	0.394	0.270	57	24.0	2.1
S_Pav	mid	05	229.630	231.503	0.398	0.280	62	24.0	2.1
S_Pav	mid	06	235.481	237.354	0.402	0.273	65	24.0	2.6
S_Pav	mid	07	239.200	240.135	0.405	0.281	67	24.0	2.7
S_Pav	mid	08	244.095	245.031	0.395	0.243	64	24.0	2.7
S_Pav	mid	09	245.388	247.262	0.399	0.239	64	24.0	2.5
S_Pav	mid	10	251.634	253.507	0.328	0.243	37	24.0	1.8
S_Pav	mid	11	253.967	255.840	0.322	0.241	36	24.0	1.9
S_Pav	mid	12	258.696	260.569	0.374	0.227	64	24.0	2.6
S_Pav	mid	13	262.151	263.087	0.374	0.226	64	24.0	3.0
S_Pav	mid	14	265.583	267.456	0.312	0.233	36	24.0	2.2
S_Pav	mid	15	267.833	269.706	0.308	0.228	37	24.0	2.2
S_Pav	compact	00	213.876	215.749	1.169	1.107	−68	24.0	2.9
S_Pav	compact	01	216.076	217.950	1.155	1.100	−89	24.0	3.2
S_Pav	compact	04	227.275	229.148	1.100	1.051	86	24.0	2.9
S_Pav	compact	05	229.630	231.503	1.061	1.043	−88	24.0	3.0
S_Pav	compact	08	244.095	245.031	1.049	0.959	−53	24.0	4.1
S_Pav	compact	09	245.388	247.262	1.107	0.983	−48	24.0	3.3
S_Pav	compact	12	258.696	260.569	0.984	0.910	−40	24.0	3.7
S_Pav	compact	13	262.151	263.087	0.914	0.872	29	24.0	4.1
T_Mic	extended	00	213.844	215.717	0.024	0.023	−58	2.0	1.1
T_Mic	extended	01	216.044	217.917	0.024	0.023	−64	2.0	1.2
T_Mic	extended	02	220.243	222.116	0.025	0.023	−77	2.0	1.3
T_Mic	extended	03	223.638	225.511	0.024	0.023	86	2.0	1.1
T_Mic	extended	04	227.241	229.114	0.023	0.022	−73	2.0	1.2
T_Mic	extended	05	229.596	231.468	0.023	0.022	−56	2.0	1.2
T_Mic	extended	06	235.445	237.318	0.023	0.022	87	2.0	1.2
T_Mic	extended	07	239.163	240.099	0.023	0.022	76	2.0	1.4
T_Mic	extended	08	244.058	244.994	0.026	0.022	−86	2.0	1.4
T_Mic	extended	09	245.351	247.224	0.026	0.022	−85	2.0	1.2
T_Mic	extended	10	251.596	253.469	0.028	0.021	−82	2.0	1.2
T_Mic	extended	11	253.929	255.802	0.028	0.021	−81	2.0	1.2
T_Mic	extended	12	258.657	260.530	0.024	0.020	−89	2.0	1.3
T_Mic	extended	13	262.112	263.047	0.024	0.021	−87	2.0	1.5
T_Mic	extended	14	265.543	267.415	0.027	0.020	−83	2.0	1.4
T_Mic	extended	15	267.792	269.665	0.027	0.020	−83	2.0	1.4
T_Mic	mid	00	213.844	215.717	0.332	0.294	76	24.0	1.9
T_Mic	mid	01	216.044	217.917	0.329	0.291	73	24.0	2.0
T_Mic	mid	02	220.243	222.116	0.340	0.288	78	24.0	2.3
T_Mic	mid	03	223.637	225.510	0.335	0.283	81	24.0	1.9
T_Mic	mid	04	227.241	229.114	0.315	0.279	71	24.0	2.0
T_Mic	mid	05	229.596	231.469	0.334	0.277	81	24.0	2.1
T_Mic	mid	06	235.445	237.318	0.319	0.269	83	24.0	2.0
T_Mic	mid	07	239.163	240.099	0.345	0.268	86	24.0	2.3
T_Mic	mid	08	244.058	244.994	0.298	0.259	71	24.0	2.6
T_Mic	mid	09	245.357	247.230	0.294	0.254	72	24.0	2.3
T_Mic	mid	10	251.591	253.464	0.304	0.240	87	24.0	2.3
T_Mic	mid	11	253.954	255.827	0.301	0.241	85	24.0	2.2
T_Mic	mid	12	258.631	260.505	0.279	0.241	72	24.0	2.5
T_Mic	mid	13	262.112	263.047	0.298	0.241	78	24.0	2.9
T_Mic	mid	14	265.541	267.414	0.287	0.229	88	24.0	2.7

Table E.3. continued.

Star	Configuration	Cube No.	Low (GHz)	High (GHz)	b_{maj} (arcsec)	b_{min} (arcsec)	b_{PA} (deg)	Imsize (arcsec)	σ_{rms} (mJy)
T_Mic	mid	15	267.791	269.664	0.320	0.226	−88	24.0	2.7
T_Mic	compact	00	213.844	215.717	1.095	0.715	−80	24.0	3.6
T_Mic	compact	01	216.044	217.917	1.113	0.711	−79	24.0	4.0
T_Mic	compact	04	227.241	229.114	1.075	0.692	−78	24.0	4.1
T_Mic	compact	05	229.595	231.469	1.041	0.662	−79	24.0	4.2
T_Mic	compact	08	244.058	244.994	1.169	0.949	−82	24.0	3.7
T_Mic	compact	09	245.351	247.224	1.157	0.943	−81	24.0	3.4
T_Mic	compact	12	258.657	260.530	1.111	0.892	−80	24.0	3.5
T_Mic	compact	13	262.112	263.047	1.103	0.887	−77	24.0	4.2
U_Del	extended	00	213.867	215.740	0.034	0.023	10	2.0	0.8
U_Del	extended	01	216.067	217.940	0.030	0.021	4	2.0	1.2
U_Del	extended	02	220.267	222.140	0.041	0.025	−14	2.0	2.0
U_Del	extended	03	223.662	225.535	0.040	0.023	−12	2.0	1.5
U_Del	extended	04	227.264	229.137	0.028	0.020	4	2.0	0.9
U_Del	extended	05	229.620	231.493	0.028	0.020	2	2.0	0.8
U_Del	extended	06	235.470	237.343	0.039	0.025	−9	2.0	1.6
U_Del	extended	07	239.189	240.124	0.044	0.025	0	2.0	4.9
U_Del	extended	08	244.084	245.020	0.033	0.023	−23	2.0	1.7
U_Del	extended	09	245.377	247.250	0.032	0.019	−32	2.0	0.8
U_Del	extended	10	251.624	253.497	0.039	0.019	−45	2.0	1.0
U_Del	extended	11	253.957	255.829	0.039	0.020	−44	2.0	1.0
U_Del	extended	12	258.684	260.556	0.030	0.019	−31	2.0	0.9
U_Del	extended	13	262.139	263.075	0.031	0.020	−26	2.0	1.8
U_Del	extended	14	265.571	267.444	0.037	0.020	−45	2.0	1.3
U_Del	extended	15	267.821	269.694	0.037	0.019	−44	2.0	1.2
U_Del	mid	00	213.867	215.740	0.418	0.388	−56	24.0	2.8
U_Del	mid	01	216.067	217.940	0.463	0.417	−52	24.0	3.6
U_Del	mid	02	220.267	222.140	0.477	0.275	−45	24.0	2.2
U_Del	mid	03	223.661	225.534	0.466	0.270	−46	24.0	1.9
U_Del	mid	04	227.265	229.138	0.377	0.352	−13	24.0	2.9
U_Del	mid	05	229.620	231.493	0.664	0.440	31	24.0	4.0
U_Del	mid	06	235.470	237.343	0.446	0.259	−46	24.0	2.2
U_Del	mid	07	239.189	240.124	0.460	0.268	−51	24.0	2.5
U_Del	mid	08	244.084	245.020	0.360	0.284	−17	24.0	3.5
U_Del	mid	09	245.377	247.250	0.362	0.284	−10	24.0	3.1
U_Del	mid	10	251.623	253.496	0.340	0.258	−25	24.0	2.2
U_Del	mid	11	253.956	255.829	0.332	0.252	−25	24.0	2.2
U_Del	mid	12	258.684	260.557	0.339	0.269	−21	24.0	3.3
U_Del	mid	13	262.139	263.075	0.335	0.268	−14	24.0	3.8
U_Del	mid	14	265.571	267.444	0.334	0.265	−32	24.0	2.7
U_Del	mid	15	267.821	269.694	0.315	0.262	−29	24.0	2.6
U_Del	compact	00	213.867	215.740	1.327	1.170	54	24.0	2.2
U_Del	compact	01	216.067	217.940	1.351	1.160	54	24.0	2.3
U_Del	compact	04	227.264	229.137	1.283	1.141	58	24.0	2.3
U_Del	compact	05	229.620	231.493	1.253	1.118	48	24.0	2.1
U_Del	compact	08	244.084	245.020	1.357	1.137	34	24.0	4.3
U_Del	compact	09	245.377	247.250	1.355	1.137	35	24.0	3.6
U_Del	compact	12	258.684	260.557	1.300	1.062	40	24.0	4.0
U_Del	compact	13	262.139	263.075	1.252	0.940	39	24.0	4.6
U_Her	extended	00	213.872	215.745	0.033	0.023	−12	2.0	1.1
U_Her	extended	01	216.073	217.946	0.032	0.023	−11	2.0	1.2
U_Her	extended	02	220.273	222.146	0.032	0.022	14	2.0	1.7
U_Her	extended	03	223.668	225.541	0.031	0.022	15	2.0	1.5
U_Her	extended	04	227.270	229.143	0.030	0.022	−9	2.0	1.1
U_Her	extended	05	229.626	231.499	0.031	0.021	−11	2.0	1.1
U_Her	extended	06	235.476	237.349	0.030	0.020	16	2.0	1.6

Table E.3. continued.

Star	Configuration	Cube No.	Low (GHz)	High (GHz)	b_{maj} (arcsec)	b_{min} (arcsec)	b_{PA} (deg)	Imsize (arcsec)	σ_{rms} (mJy)
U_Her	extended	07	239.195	240.131	0.031	0.021	15	2.0	2.0
U_Her	extended	08	244.091	245.026	0.029	0.022	16	2.0	1.2
U_Her	extended	09	245.384	247.257	0.029	0.020	21	2.0	0.9
U_Her	extended	10	251.630	253.503	0.027	0.020	13	2.0	1.2
U_Her	extended	11	253.963	255.836	0.027	0.020	13	2.0	1.3
U_Her	extended	12	258.691	260.564	0.027	0.019	19	2.0	1.0
U_Her	extended	13	262.146	263.082	0.028	0.020	20	2.0	1.2
U_Her	extended	14	265.578	267.451	0.026	0.019	13	2.0	1.4
U_Her	extended	15	267.828	269.701	0.026	0.019	11	2.0	1.5
U_Her	mid	00	213.873	215.745	0.444	0.334	−13	18.0	3.5
U_Her	mid	01	216.073	217.946	0.444	0.329	−12	18.0	3.7
U_Her	mid	02	220.273	222.146	0.450	0.337	−40	18.0	4.2
U_Her	mid	03	223.668	225.541	0.446	0.331	−41	18.0	3.6
U_Her	mid	04	227.270	229.143	0.421	0.314	−14	18.0	3.8
U_Her	mid	05	229.626	231.499	0.402	0.300	−24	18.0	3.6
U_Her	mid	06	235.476	237.349	0.403	0.301	−33	18.0	4.1
U_Her	mid	07	239.195	240.131	0.403	0.297	−31	18.0	4.4
U_Her	mid	08	244.091	245.026	0.415	0.293	−39	18.0	3.7
U_Her	mid	09	245.384	247.257	0.412	0.286	−38	18.0	3.2
U_Her	mid	10	251.630	253.503	0.171	0.146	−23	18.0	3.5
U_Her	mid	11	253.963	255.836	0.170	0.141	−22	18.0	3.6
U_Her	mid	12	258.691	260.563	0.395	0.273	−37	18.0	3.6
U_Her	mid	13	262.146	263.082	0.384	0.276	−38	18.0	4.4
U_Her	mid	14	265.578	267.451	0.161	0.137	−14	18.0	4.8
U_Her	mid	15	267.828	269.701	0.160	0.136	−14	18.0	4.1
U_Her	compact	00	213.873	215.746	1.045	0.885	23	24.0	2.5
U_Her	compact	01	216.073	217.945	1.031	0.908	26	24.0	2.3
U_Her	compact	04	227.270	229.143	0.992	0.875	27	24.0	2.4
U_Her	compact	05	229.626	231.499	0.978	0.837	23	24.0	2.5
U_Her	compact	08	244.091	245.026	1.247	1.004	25	24.0	5.5
U_Her	compact	09	245.384	247.257	1.164	0.912	25	24.0	4.4
U_Her	compact	12	258.690	260.563	1.164	0.889	22	24.0	4.7
U_Her	compact	13	262.146	263.082	1.271	0.935	32	24.0	6.8
VX_Sgr	extended	00	213.858	215.731	0.033	0.027	69	1.2	1.3
VX_Sgr	extended	01	216.058	217.931	0.033	0.026	66	1.2	1.4
VX_Sgr	extended	02	220.258	222.131	0.031	0.022	−84	1.2	1.3
VX_Sgr	extended	03	223.653	225.526	0.030	0.022	−83	1.2	1.0
VX_Sgr	extended	04	227.256	229.129	0.032	0.025	65	1.2	1.4
VX_Sgr	extended	05	229.611	231.484	0.031	0.025	68	1.2	1.3
VX_Sgr	extended	06	235.461	237.334	0.029	0.021	−83	1.2	1.1
VX_Sgr	extended	07	239.180	240.115	0.028	0.020	−82	1.2	1.3
VX_Sgr	extended	08	244.074	245.010	0.033	0.024	78	1.2	1.7
VX_Sgr	extended	09	245.368	247.241	0.032	0.023	81	1.2	1.4
VX_Sgr	extended	10	251.613	253.486	0.035	0.023	−89	1.2	1.4
VX_Sgr	extended	11	253.946	255.819	0.037	0.024	−88	1.2	1.3
VX_Sgr	extended	12	258.674	260.547	0.030	0.022	79	1.2	1.4
VX_Sgr	extended	13	262.129	263.065	0.030	0.022	80	1.2	1.8
VX_Sgr	extended	14	265.560	267.433	0.034	0.022	89	1.2	1.6
VX_Sgr	extended	15	267.810	269.683	0.033	0.021	89	1.2	1.6
VX_Sgr	mid	00	213.858	215.731	0.234	0.130	−70	24.0	2.4
VX_Sgr	mid	01	216.058	217.931	0.217	0.128	−73	24.0	2.9
VX_Sgr	mid	02	220.258	222.131	0.210	0.113	−75	24.0	2.6
VX_Sgr	mid	03	223.652	225.525	0.195	0.113	−76	24.0	2.1
VX_Sgr	mid	04	227.256	229.129	0.211	0.118	−74	24.0	2.5
VX_Sgr	mid	05	229.611	231.484	0.211	0.119	−73	24.0	2.5
VX_Sgr	mid	06	235.461	237.334	0.183	0.108	−75	24.0	2.3
VX_Sgr	mid	07	239.180	240.115	0.181	0.106	−75	24.0	2.6

Table E.3. continued.

Star	Configuration	Cube No.	Low (GHz)	High (GHz)	b_{maj} (arcsec)	b_{min} (arcsec)	b_{PA} (deg)	Imsize (arcsec)	σ_{rms} (mJy)
VX_Sgr	mid	08	244.074	245.010	0.184	0.109	−74	24.0	2.7
VX_Sgr	mid	09	245.368	247.241	0.183	0.110	−74	24.0	2.4
VX_Sgr	mid	10	251.613	253.486	0.319	0.266	87	24.0	2.6
VX_Sgr	mid	11	253.946	255.819	0.321	0.262	89	24.0	2.7
VX_Sgr	mid	12	258.674	260.548	0.172	0.104	−75	24.0	2.7
VX_Sgr	mid	13	262.129	263.065	0.170	0.103	−75	24.0	3.1
VX_Sgr	mid	14	265.560	267.433	0.315	0.251	−88	24.0	3.1
VX_Sgr	mid	15	267.810	269.683	0.316	0.249	−88	24.0	3.2
VX_Sgr	compact	00	213.858	215.731	1.251	0.932	82	36.0	2.3
VX_Sgr	compact	01	216.058	217.931	1.263	0.919	83	36.0	2.3
VX_Sgr	compact	04	227.255	229.128	1.195	0.906	85	36.0	2.4
VX_Sgr	compact	05	229.611	231.484	1.169	0.887	84	36.0	2.3
VX_Sgr	compact	08	244.074	245.010	1.308	0.938	77	36.0	2.8
VX_Sgr	compact	09	245.368	247.241	1.283	0.929	76	36.0	2.4
VX_Sgr	compact	12	258.673	260.546	1.238	0.898	75	36.0	2.6
VX_Sgr	compact	13	262.129	263.065	1.212	0.896	77	36.0	3.2
V_PsA	extended	00	213.870	215.743	0.025	0.022	−35	2.0	0.8
V_PsA	extended	01	216.070	217.943	0.025	0.022	−33	2.0	0.8
V_PsA	extended	02	220.270	222.143	0.023	0.021	23	2.0	0.9
V_PsA	extended	03	223.666	225.539	0.023	0.021	28	2.0	0.8
V_PsA	extended	04	227.268	229.140	0.023	0.021	−31	2.0	0.8
V_PsA	extended	05	229.624	231.496	0.024	0.020	−34	2.0	0.8
V_PsA	extended	06	235.474	237.347	0.021	0.020	18	2.0	0.8
V_PsA	extended	07	239.193	240.128	0.021	0.020	18	2.0	1.0
V_PsA	extended	08	244.088	245.023	0.028	0.020	86	2.0	1.1
V_PsA	extended	09	245.381	247.254	0.028	0.020	88	2.0	0.9
V_PsA	extended	10	251.628	253.501	0.029	0.021	−87	2.0	1.0
V_PsA	extended	11	253.960	255.833	0.029	0.021	−86	2.0	1.1
V_PsA	extended	12	258.688	260.561	0.027	0.019	88	2.0	0.9
V_PsA	extended	13	262.143	263.079	0.026	0.019	89	2.0	1.2
V_PsA	extended	14	265.575	267.448	0.027	0.020	−82	2.0	1.3
V_PsA	extended	15	267.825	269.698	0.027	0.020	−83	2.0	1.2
V_PsA	mid	00	213.870	215.743	0.422	0.315	78	24.0	2.0
V_PsA	mid	01	216.070	217.943	0.419	0.318	74	24.0	2.3
V_PsA	mid	02	220.270	222.143	0.433	0.291	76	24.0	2.1
V_PsA	mid	03	223.665	225.538	0.408	0.290	77	24.0	1.8
V_PsA	mid	04	227.268	229.141	0.400	0.297	74	24.0	2.0
V_PsA	mid	05	229.623	231.497	0.384	0.298	77	24.0	2.0
V_PsA	mid	06	235.474	237.347	0.396	0.277	75	24.0	1.9
V_PsA	mid	07	239.193	240.128	0.402	0.287	79	24.0	2.3
V_PsA	mid	08	244.088	245.023	0.333	0.270	72	24.0	2.5
V_PsA	mid	09	245.381	247.254	0.326	0.262	73	24.0	2.2
V_PsA	mid	10	251.626	253.500	0.295	0.246	67	24.0	1.8
V_PsA	mid	11	253.960	255.833	0.292	0.248	69	24.0	1.8
V_PsA	mid	12	258.688	260.562	0.311	0.246	70	24.0	2.4
V_PsA	mid	13	262.143	263.079	0.342	0.254	81	24.0	2.8
V_PsA	mid	14	265.575	267.448	0.286	0.238	67	24.0	2.1
V_PsA	mid	15	267.825	269.698	0.283	0.233	66	24.0	2.1
V_PsA	compact	00	213.870	215.743	1.083	0.864	87	24.0	2.7
V_PsA	compact	01	216.070	217.943	1.080	0.866	−89	24.0	2.7
V_PsA	compact	04	227.268	229.141	1.046	0.832	88	24.0	2.8
V_PsA	compact	05	229.623	231.497	1.032	0.820	85	24.0	2.9
V_PsA	compact	08	244.088	245.023	1.095	0.781	89	24.0	2.6
V_PsA	compact	09	245.381	247.254	1.085	0.773	88	24.0	2.2
V_PsA	compact	12	258.688	260.561	1.033	0.735	88	24.0	2.6
V_PsA	compact	13	262.143	263.079	1.024	0.724	87	24.0	2.9

Table E.3. continued.

Star	Configuration	Cube No.	Low (GHz)	High (GHz)	b_{maj} (arcsec)	b_{min} (arcsec)	b_{PA} (deg)	Imsize (arcsec)	σ_{rms} (mJy)
W_Aql	extended	00	213.880	215.753	0.025	0.023	−21	2.0	0.4
W_Aql	extended	01	216.080	217.953	0.025	0.023	−17	2.0	0.4
W_Aql	extended	02	220.281	222.154	0.025	0.023	−31	2.0	0.5
W_Aql	extended	03	223.676	225.549	0.025	0.023	−18	2.0	0.4
W_Aql	extended	04	227.278	229.151	0.023	0.022	−9	2.0	0.4
W_Aql	extended	05	229.634	231.507	0.024	0.022	−19	2.0	0.4
W_Aql	extended	06	235.485	237.358	0.023	0.022	−14	2.0	0.4
W_Aql	extended	07	239.204	240.139	0.023	0.022	−21	2.0	0.5
W_Aql	extended	08	244.099	245.035	0.031	0.022	49	2.0	0.7
W_Aql	extended	09	245.393	247.266	0.024	0.021	−75	2.0	0.5
W_Aql	extended	10	251.640	253.513	0.026	0.021	−70	2.0	0.6
W_Aql	extended	11	253.972	255.845	0.026	0.021	−74	2.0	0.6
W_Aql	extended	12	258.699	260.572	0.023	0.020	−71	2.0	0.6
W_Aql	extended	13	262.156	263.091	0.024	0.021	−80	2.0	0.8
W_Aql	extended	14	265.587	267.460	0.026	0.020	−74	2.0	0.7
W_Aql	extended	15	267.837	269.710	0.025	0.020	−75	2.0	0.7
W_Aql	mid	00	213.880	215.753	0.502	0.306	−72	24.0	2.3
W_Aql	mid	01	216.080	217.953	0.496	0.329	−77	24.0	2.4
W_Aql	mid	02	220.280	222.154	0.460	0.284	−69	24.0	2.2
W_Aql	mid	03	223.675	225.548	0.453	0.280	−69	24.0	1.9
W_Aql	mid	04	227.278	229.151	0.478	0.292	−74	24.0	2.3
W_Aql	mid	05	229.634	231.507	0.474	0.292	−74	24.0	2.3
W_Aql	mid	06	235.485	237.358	0.433	0.266	−69	24.0	2.2
W_Aql	mid	07	239.204	240.139	0.425	0.274	−70	24.0	2.3
W_Aql	mid	08	244.099	245.035	0.415	0.287	−84	24.0	2.6
W_Aql	mid	09	245.393	247.266	0.397	0.259	−73	24.0	2.3
W_Aql	mid	10	251.639	253.512	0.356	0.274	−79	24.0	2.3
W_Aql	mid	11	253.972	255.845	0.395	0.277	−77	24.0	2.8
W_Aql	mid	12	258.700	260.573	0.375	0.250	−74	24.0	2.5
W_Aql	mid	13	262.156	263.091	0.374	0.250	−74	24.0	2.9
W_Aql	mid	14	265.587	267.460	0.390	0.284	−81	24.0	3.5
W_Aql	mid	15	267.837	269.710	0.372	0.272	−86	24.0	3.9
W_Aql	compact	00	213.880	215.753	1.015	0.727	77	24.0	2.7
W_Aql	compact	01	216.080	217.953	0.969	0.711	−89	24.0	2.8
W_Aql	compact	04	227.278	229.151	0.890	0.695	70	24.0	3.1
W_Aql	compact	05	229.634	231.507	0.830	0.678	78	24.0	3.0
W_Aql	compact	08	244.099	245.035	1.176	0.785	73	24.0	3.3
W_Aql	compact	09	245.393	247.266	1.177	0.792	73	24.0	2.8
W_Aql	compact	12	258.699	260.572	1.123	0.766	74	24.0	3.1
W_Aql	compact	13	262.156	263.091	1.111	0.881	82	24.0	4.2

Notes. Low and High are the minimum and maximum observed frequencies in the cube. The parameters b_{maj}, b_{min} and b_{PA} are the major and minor axis and the position angle of the synthesized beam, respectively. The noise σ_{rms} is measured from a selection of emission-free channels in the cube without the primary beam correction. U Del compact configuration cubes 08, 09, 12 and 13, and KW Sgr mid configuration cubes 00, 01, 04 and 05 have not yet been fully observed.